MULTISCALE FLOW INTERACTIONS IN THE COMPLEX

TERRAIN OF NORTHWESTERN UTAH

by

Matthew E. Jeglum

A dissertation submitted to the faculty of
The University of Utah
in partial fulfillment of the requirements for the degree of

Doctor of Philosophy

Department of Atmospheric Sciences

The University of Utah

December 2016

The University of Utah Graduate School

STATEMENT OF DISSERTATION APPROVAL

The dissertation of   **Matthew E. Jeglum**

has been approved by the following supervisory committee members:

Sebastian Wilhelm Hoch	, Chair	**6/15/2016** Date Approved
William James Steenburgh	, Member	**6/15/2016** Date Approved
John D. Horel	, Member	**6/15/2016** Date Approved
Eric R. Pardyjak	, Member	**6/15/2016** Date Approved
Robert M. Banta	, Member	**6/15/2016** Date Approved

and by   **Kevin Perry**   , Chair/Dean of

the Department/College/School of   **Atmospheric Sciences**

and by David B. Kieda, Dean of The Graduate School.

ABSTRACT

Winds in complex terrain are forced by a range of mechanisms operating on multiple scales including synoptic scale winds, thermally direct circulations, and dynamic interactions of flow with terrain. Flows forced on various scales interact in complex ways that are modulated by the structure of the atmospheric boundary layer. Here we analyze surface and boundary layer flows observed at Dugway Proving Ground (DPG) during the Mountain Terrain Atmospheric Modeling and Observations (MATER-HORN) field program to diagnose and understand the multiscale forcing mechanisms and their interactions.

A 17-year climatology at 26 surface automated weather stations found that the surface wind at DPG is bimodal at times when thermally driven winds would produce a single direction. The two modes, which corresponded to northerly and southerly winds, are referred to as the "Northerly Regime" and the "Southerly Regime". The Southerly Regime is relatively common in January and August and uncommon in May while the Northerly Regime is most common in May. The existence of the regimes and their seasonal distribution are likely attributable to variability in synoptic and mesoscale phenomena such as the Great Basin Confluence Zone, development of thermal low pressure over the Intermountain West in summer, and regional thermal contrasts. Knowledge of these flow systems can be used to assess and fix model deficiencies.

One specific flow was found to cause a high number of large nocturnal temperature fluctuations on the slope of a mountain at DPG named Granite Mountain. Large temperature fluctuations (LTFs), defined as a drop of at least $3\,^{\circ}\mathrm{C}$ in 30 min followed

by a temperature rise, were identified at over 100 automatic weather stations at DPG. LTFs are most common in areas 50-100 m above the basin floor during the nocturnal period, including on the east slope of Granite Mountain. The cause of these fluctuations was found to be an orographic wake that formed when a nocturnal, stably stratified southwesterly flow impinges on Granite Mountain and is blocked at low levels. This blocked flow causes warm air to descend the lee of the mountain. This warm flow, in conjunction with a strong cold-air pool at the foot of Granite Mountain, creates a strong horizontal temperature gradient that, when displaced, produces large temperature fluctuations at the surface. The displacement of this temperature gradient is likely due to variations in the incident flow and the development of vertical-axis eddies on the southern end of Granite Mountain.

This increased understanding of flows on multiple scales, their interactions, and their likely forcing mechanisms will be used to inform numerical model improvement efforts as part of the MATERHORN Program.

CONTENTS

Appendices

ACKNOWLEDGMENTS

CHAPTER 1

INTRODUCTION

1.1 Motivation

The impact of surface winds on human communities is not limited to high-impact events such as severe convection or tropical cyclones. Day-to-day variations of near-surface winds impact human communities through their influence on air quality (Jerrett et al. 2005; Coen et al. 2012; Whiteman et al. 2014), wind energy generation (Wilczak et al. 2014), wildfire suppression and prediction (Butler et al. 2006), agriculture (Li et al. 2015) and emergency response and military operations (Liu et al. 2008). Accurate forecasts of these winds relies heavily on the output of numerical weather prediction models (Doyle et al. 2013). Unfortunately, numerical model simulations of wind, particularly in complex terrain, tend to be poor (Rife et al. 2004; Hart et al. 2005; Berg and Zhong 2005; Seaman et al. 2011; Jiménez and Dudhia 2013).

This research was conducted as part of the Mountain Terrain Atmospheric Modeling and Observations (MATERHORN) program, which was designed with an overarching goal of improving weather prediction in complex terrain through (1) increasing our knowledge of flow processes there, and (2) improving numerical model performance (Fernando et al. 2015). The near-surface wind and temperature fields are modulated by dynamic and thermodynamic processes occurring within the atmospheric boundary layer (ABL). This research will utilize observations and numerical simulations to examine near-surface flows in an area of complex terrain in northwestern Utah, with the objective of understanding the interaction of flows on multiple

scales, both within and above the ABL. This improved understanding of flows and ABL processes will enable targeted model improvements when deficiencies in the simulations are identified.

The following sections provide an overview of the MATERHORN program and of the processes, both within and above the ABL, that drive near-surface winds and modulate the interactions betwen different scales of forcing.

1.2 The MATERHORN Field Campaign

To accomplish the MATERHORN objectives described above, two intensive field campaigns were conducted using advanced observational tools to measure phenomena occurring on spatial scales from the mesoscale to the Kolmogorov scale.

Dugway Proving Ground (DPG) in Northwest Utah was the location of the MATER-HORN field experiments as it offered complex terrain, a large preexisting instrument network, and accessibility for instrument installation and aircraft operation. DPG and the surrounding airshed consist of wide, flat valleys separated by steep-sided mountain ranges that in some cases exceed 3000 m in elevation. The climate is semi-arid, with the valley bottoms receiving as little as 150 mm of precipitation per year.

The first field campaign, the MATERHORN Fall Experiment, occurred from 25 September-31 October 2012. The second, the MATERHORN Spring Experiment, occurred from 1-31 May 2012. October and May were chosen primarily due to the favorable mix of synoptic scale ridges and troughs during those months. Instruments that were running continuously during both one-month periods include over 120 automatic weather stations (AWSs), 8 atmospheric flux towers, multiple sodars, and extensive surface energy balance measurements. During each month-long campaign ten 24-h intensive observation periods IOPs were conducted where additional sensors were operated. IOPs were conducted in conditions that were weakly, moderately, and strongly forced on the synoptic scale, although weakly forced events were most common. All IOPs were precipitation-free. Instruments operated only during IOPs

include all lidars, a Twin Otter aircraft, an infrared camera, tethered balloons, radiosoundings, and other instruments.

MATERHORN instrumentation was deployed to measure three distinct areas at DPG (lower left inset of Fig. 1.1): Playa, Granite Mountain, and east basin. The playa is a nearly flat, seasonally flooded playa that is largely vegetation-free. Instrumentation on the playa was primarily focused at one site, labeled "Playa Site" in Fig. 1.1. Instruments there included a tethered balloon, radiosonde launches, and full surface energy balance instrumentation. Five permanently installed AWSs are located at several other locations on the playa.

Granite Mountain (GM) sits immediately east of the margin of the playa and rises a maximum of 800 m above the surrounding basin. GM is approximately 10 km

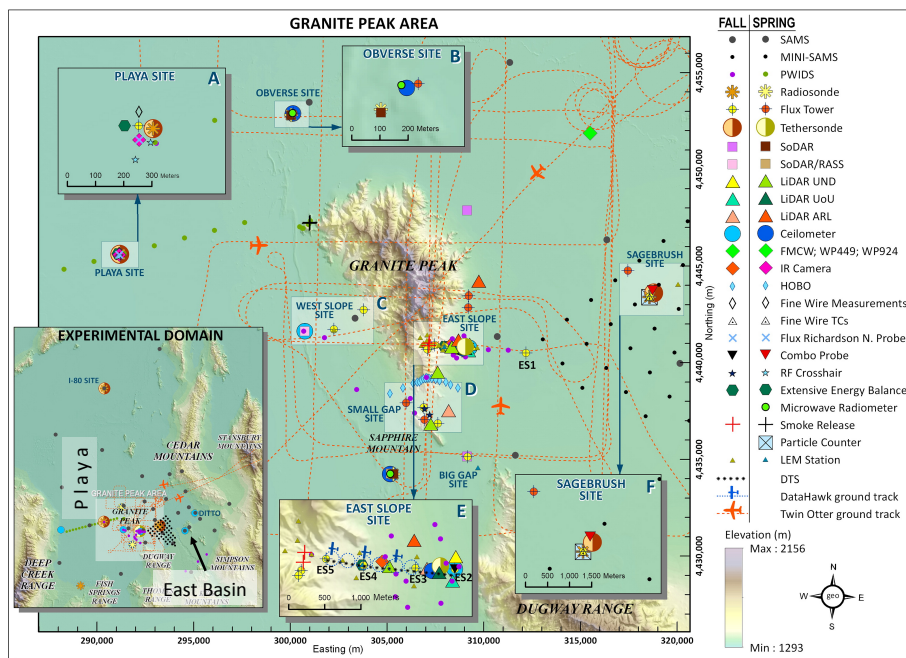Fig. 1.1. Map of the Granite Mountain study area with all deployed instruments shown. The lower left inset shows the full MATERHORN domain. Other insets show specific areas. Only the additional instruments deployed (or relocated) for the spring experiment are shown under the "spring" column. Reprinted with slight modification from Fernando et al. (2015). ©2015 American Meteorological Society. Reprinted with permission.

long, 5 km wide, and is elongated in a north-northwest to south-southeast direction. The upper slopes of GM are steep and rocky with sparse vegetation. Numerous long, relatively uniform alluvial fans surround the base of the peak. One of the alluvial fans on the southeast side of GM was very heavily instrumented during MATERHORN and is labeled the "East Slope Site" in Fig. 1.1 (Lehner et al. 2015a; Grachev et al. 2015). Notable instrumentation at the East Slope site included full surface energy balance instrumentation, 5 atmospheric flux towers, and multiple lidars. A number of portable AWSs were deployed into up-slope and along-slope transects at the East Slope Site. Immediately to the south of the East Slope Site a transect of simple temperature and humidity sensors was deployed up both the east and west flanks of GM. In Chapter 2 and Chapter 3, the East Slope Site will be referred to simply as the East Slope.

The east basin is the large basin east of GM. This basin slopes gradually from southeast to northwest and features sparse grass and shrub vegetation that reaches a maximum of 1 m in height. The east basin includes the Sagebrush Site, where a tethered balloon, flux tower, and full surface energy balance were located (Jensen et al. 2016). The east basin contains the majority of the AWSs deployed for MATERHORN including 51 AWSs that are oriented in a triangular 1.6 km by 1.6 km grid. The east basin merges with the playa on the north end of GM. South of GM and north of the Dugway Range is a topographic gap connecting the playa and east basin that was instrumented with several AWSs, a 30-m tower, and a sodar. This gap will be referred to as the "Gap" throughout this work.

Twenty-six of the permanent AWSs at DPG have been installed for at least 7 years (with a maximum of 17 years). These stations have a period of record sufficient for climatological investigations and are well distributed spatially across the DPG area. They will be the primary focus for the analysis in Chapter 2. Four portable AWSs and one flux tower deployed on the East Slope of GM will be the focus of Chapter 3, although other instruments will be used to supplement these data.

1.3 Characteristics of the ABL in Complex Terrain

The ABL is the atmospheric layer that is influenced on short timescales by its contact with the surface of the Earth. Diurnal and seasonal variations in the ABL structure strongly modulate the interaction of flows forced by differing scales (Stull 1988). This section will discuss the canonical evolution of the ABL, with a specific focus on how the ABL evolves in complex terrain and its application to multiscale flow interactions there.

The basic structure of the ABL over land is modulated diurnally by solar radiation. In mid-afternoon the ABL will typically display a *mixed layer* typically extending to a depth of hundreds or, in the case of arid, summertime conditions, thousands of meters (Stull 1988) with a lapse rate close to dry adiabatic, subgeostrophic wind speeds, and substantial turbulence. The top of the mixed layer is often capped by a stable layer. Above this stable layer lies the free atmosphere, which is characterized by a relative lack of turbulence. Turbulent mixing in the mixed layer can be mechanical or convective in nature. Turbulent eddies at the top of the mixed layer can entrain free-atmosphere air into the mixed layer. Similarly, vertical transport of momentum from the free atmosphere into the ABL can be substantial during this time. The lowest approximately 10% of the mixed layer is called the *surface layer* and is marked by high wind shear values, superadiabatic lapse rates, and approximately constant turbulent fluxes with height.

Near sunset the buoyant turbulent eddies in the mixed layer weaken, beginning what is referred to as the *evening transition* (Sastre et al. 2015). With this decay of turbulence a large part of the mixed layer now becomes the *residual layer*, as it initially retains the mean-state characteristics of the mixed layer. Like the mixed layer, the residual layer is often capped by a stable layer. Mass and momentum exchange to the residual layer from the free atmosphere is reduced relative to the mixed layer.

With the loss of solar radiation the radiation balance at the surface becomes neg-

ative, contributing to a negative surface energy balance and cooling of the air in contact with the ground. This growing layer of cold air is called the *stable boundary layer* (SBL) and can be as shallow as 10 m in depth (Banta et al. 2007). The SBL is characterized by sporadic turbulence and a strong resistance to vertical motions. When confined by terrain the SBL is referred to as a cold-air pool (CAP) (Whiteman et al. 2001). The top of the SBL is often demarcated by a strong gradient in potential temperature or turbulence intensity, although determining this SBL top is often difficult (Pichugina and Banta 2010). Similar to the mixed layer, the lowest 10% of the SBL is also called the surface layer and displays almost constant turbulent fluxes with height. Unlike its analog in the mixed layer, the nocturnal surface layer often displays very strong stratification. Within the SBL vertical momentum transport is often small and local pressure gradients are the primary wind forcing.

Shortly after sunrise the radiation balance again becomes positive, contributing to the development of a positive surface energy balance. As the surface warms, the sensible heat flux can become strongly positive, particularly in dry climates where the Bowen ratio is large. Buoyant turbulent eddies driven by the surface heating begin to erode the SBL. This period is referred to as the *morning transition* (Angevine et al. 2001). As the eddies grow in scale and depth, the mixed layer likewise grows vertically. If the free atmosphere conditions have not changed, buoyant eddies will mix through the entirety of the residual layer until it again begins to entrain air from the free atmosphere.

Complex terrain introduces horizontal heterogeneity to the ABL relative to a flat plain. Heterogeneity in the mixed layer tends to be greatest in the morning when the growing mixed layer strongly follows the terrain. By late afternoon the terrain-induced heterogeneity is reduced (Kossmann et al. 1998; De Wekker et al. 2004) due to faster mixed layer growth over the valley at that time. The SBL in complex terrain can display strong gradients of temperature and wind due to the formation of CAPs in low-lying terrain. For example, the temperature in the bottom of the Peter Sinks

basin in Northern Utah was observed to be over 20 °C colder than the temperature on slopes adjacent to the basin that were only 100 m higher in elevation (Clements et al. 2003). Relative to the ABL over a flat plain, advective flows are generated in complex terrain during both the day and night that can modify the structure of the mixed layer and SBL (Kalthoff et al. 2005; McGowan and Sturman 2013).

Seasonal controls on the evolution of the ABL are also strong. Solar insolation is reduced due to lower sun angles during the cool season, resulting in longer-lived SBLs and shallower mixed layers. During mid-winter persistent CAPs can form due to the persistence of the SBL through the diurnal cycle (Wolyn and McKee 1989; Lareau et al. 2013). In addition to weaker solar irradiance, the cool season often features more frequent synoptic scale trough passages relative to the warm season. Mechanical mixing from strong winds associated with these troughs can prevent the formation of an SBL or erode a preexisting one (Petkovšek 1992; Lareau and Horel 2014). Strong winds in the free atmosphere can likewise deepen the mixed layer or at least enhance its growth rate (Pino et al. 2003). Clouds, through their impact on shortwave and longwave radiative exchange, can impact the evolution of the SBL (Ye et al. 1989) and the mixed layer. Synoptic scale lift in the vicinity of large low-pressure systems can transport air from the ABL sufficiently far that a boundary layer top is difficult to define (Stull 1988).

1.4   Wind in the ABL in Complex Terrain

Near-surface wind can be forced on scales ranging from the synoptic to the microscale. This section will discuss the scales and general mechanisms by which winds can be forced and consider how the ABL structure modulates the interactions between them.

Wind is the dynamic response of the atmosphere to pressure gradients. Pressure gradients on the largest scales over the western United States are controlled by the seasonal migration of the polar jet stream (Lareau and Horel 2012) and transient

troughs and ridges. The upper-level winds associated with these large-scale pressure gradients are generally close to being in gradient balance (Wallace and Hobbs 1977). However, in the ABL or in close proximity to terrain, departures from geostrophy can be observed.

Friction at the Earth's surface and channeling due to terrain can modify the synoptic scale flow (Whiteman and Doran 1993). Frictional drag contributes to the presence of mechanically generated turbulence in the ABL and produces a wind profile in the surface layer that is approximately logarithmic with zero wind speed at the surface. Terrain channeling takes two primary forms, pressure-driven and forced channeling. Pressure-driven channeling causes the surface wind next to a terrain barrier to align with the component of the pressure gradient parallel to the barrier. Forced channeling causes the surface wind next to a terrain barrier to align with the component of the synoptic scale flow parallel to the barrier. Channelling does not require a deep, narrow valley as exemplified by the channeling observed in the very broad upper Rhine Valley (Gross and Wippermann 1987). Pressure-driven and forced channeling can occur individually or in concert, and can result in substantial ageostrophy in the ABL.

Exclusive of a synoptically-imposed pressure gradient, asymmetric solar heating of the ground and atmosphere can induce local pressure gradients that drive thermally driven flows (Whiteman 1990, 2000). As such, thermally driven flows are directly related to the development of mixed layers and SBLs. The typical spatial scales and speeds of thermally driven flows indicate that the Coriolis force can be neglected when considering such flows, with thermal low pressure systems and katabatic flows in Antarctica the notable exceptions, as both can operate on spatial scales approaching 1000 km (Tang and Reiter 1984; Davis and McNider 1997). Three primary scales of flows characterize the thermally driven flow system in complex terrain and will be discussed in the following paragraphs.

The largest scale of thermally driven flows are mountain-plain circulations. In

these circulations, the mountain functions as an elevated heat source during the day and an elevated cooling source during the night. Since the temperature in the free atmosphere above the plain has a much smaller diurnal range, a diurnally reversing temperature gradient (and therefore pressure gradient) is produced that drives a thermally direct circulation with flow toward the mountain during the day and toward the plain at night. The mountain-plain circulation has been observed in both the Alps (Frei and Davies 1993) and the Rocky Mountains (Bossert and Cotton 1994; Li and Smith 2010).

The next scale smaller than the mountain-plain circulation are along-valley winds. Similar to the mountain-plain circulation, these winds blow up a valley during the day and down a valley at night. Valley winds arise as a result of the narrow valley atmosphere warming more readily than an adjacent plain. This excessive warming is due to the topographic amplification factor, where the incident radiation on a given area heats a smaller volume of air in the valley than over a flat plain (McKee and O'Neal 1989). The heating asymmetry produces a diurnally modulated pressure gradient that causes flow into or out of the valley, even in valleys that have flat floors (Rampanelli et al. 2004). However, advective and turbulent heat transport can reduce the daytime heating and nighttime cooling of the valley due to the topographic amplification factor (Schmidli and Rotunno 2010).

The smallest scale of thermally driven flows are slope winds. These flows operate on individual slopes with spatial scales as small as tens of meters. Slope flows are part of a diurnally reversing closed circulation produced by warm or cold boundary layers that form on a slope. Daytime upslope flows are more turbulent, on average, than downslope flows and are contained within the convective-advective boundary layer that envelops a slope. While it might be expected that convective eddies would rise vertically off the slope, they often follow the slope due to the inclined super-adiabatic layer that follows the surface (Zardi and Whiteman 2013). Downslope flows occur in a stably stratified layer and tend to be deepest and strongest on intermediate

angle slopes. On very flat slopes, outgoing longwave radiative loss is large but the component of gravity along the slope is very small. Steep slopes have less effective longwave loss due to their lower sky-view factor and downslope flows on steep slopes can suffer from excessive turbulent entrainment of ambient air, lessening their negative buoyancy (Zardi and Whiteman 2013).

When a stratified flow, whether thermally driven or synoptically forced, encounters a terrain obstacle, complex dynamically-induced flows can result. Such flows can modify the distribution of heat, momentum, and turbulence in the ABL and include vertically propagating mountain waves, orographic wakes, and lee waves. These flows will be discussed in depth in Section 1.5.

1.4.1   Near-Surface Flows at DPG

A number of studies have examined near-surface flows at DPG. Rife et al. (2002) identified a diurnal wind shift in the vicinity of the playa-east basin boundary that was attributed to the presence of a salt breeze. A salt breeze is analogous to a sea breeze, except that the land surface contrast is between the relatively wet, high-albedo playa and the dry, low-albedo east basin. Rife et al. (2002) also attributed a northeasterly flow in the evening to the lake-breeze propagating off the Great Salt Lake and consistent nocturnal southeasterly flow over the east basin to downslope or downvalley flows. Lehner et al. (2015a) and Grachev et al. (2015) identified well-developed up- and downslope flows on the East Slope of GM.

While they have not been identified at DPG in the literature, low-level jets are known to occur in adjacent valleys in Northern Utah (Banta et al. 2004). Low-level jets are a phenomenon often observed in the ABL, particularly in the SBL (Stull 1988). The definition of low-level jets varies in the literature, although Stull (1988) simplified a low-level jet to a boundary layer wind with a velocity 2 ms^{-1} greater than the layer above it. Causal mechanisms for low-level jets include classical thermally driven flows such as downvalley or downslope winds, larger-scale thermal effects such

as baroclinicity in sloping terrain, inertial oscillations, and dynamically induced jets due to large-scale forcing (Kraus et al. 1985).

Compared to heavily studied valleys such as the Inn Valley (Vergeiner and Dreiseitl 1987; Rucker et al. 2008), Owens Valley (Zhong et al. 2004), or Salt Lake Valley (Doran et al. 2002), the playa and east basin areas at DPG have a much lower aspect ratio of height-to-width of approximately 0.002. This makes applying classical expectations of thermally driven flows difficult. It remains a question as to whether the basins and adjacent mountains at DPG function as valleys, as a mountain-plain couplet, or otherwise. Valleys with similar aspect ratios to these basins have been studied, such as the Tennessee Valley, and they display relatively weak thermally driven flows that are easily influenced by synoptic-scale winds (Whiteman and Doran 1993; Eckman 1998). Fernando et al. (2015) hypothesize that the typical flows observed in these basins are up- and downvalley flows, although this conclusion is based on the assumption that these diurnally-varying flows are produced by the local terrain. The only work that has attempted to diagnose flow mechanisms at DPG (Rife et al. 2002) has only conclusively identified playa and lake breezes.

1.4.2 Multiscale Flow Interactions

Previous studies of wind flows at DPG have focused on isolating particular scales of motion. Flows forced on differing scales interact in complex ways, and understanding such interactions is a task complicated by the difficulty of characterizing the flow structure within and above the ABL. Before considering large-scale or dynamically induced motions, the thermally driven wind system alone consists of a complex superposition of the mountain-plain, valley, and slope scales (Zardi and Whiteman 2013), where the flows driven by each scale can interfere constructively or destructively with one another (Doran et al. 1990). For example, Coulter and Gudiksen (1995) examined the impact of mesoscale flows above a canyon on downvalley flows in the canyon. The mesoscale flow was partially driven by the mountain-plain circulation present on the

east slope of the Rocky Mountains in Colorado. The downvalley wind was observed in a steep, 12-km long canyon running from west to east and exiting on the plains east of the Front Range. The mesoscale flow was found to increase the velocity of the downvalley flow if sufficient mechanical turbulence could be produced at the top of the down valley flow, entraining momentum. A weak mesoscale flow did not disturb the canyon atmosphere and the downvalley flow displayed a relatively constant velocity.

The thermally driven flow system can be further modified by mesoscale and synoptic winds. Gudiksen et al. (1992) found that large-scale flows above a valley of greater than 5 ms^{-1} were sufficient to remove the surface temperature inversion on the upper slopes of the valley and retard the drainage flow in the valley. Banta et al. (2004) observed complex flow interactions between synoptic scale, mesoscale, and classical thermally driven flows in the Salt Lake Valley 100 km northeast of DPG during the Vertical Transport and Mixing Experiment (VTMX). A southerly nocturnal low-level jet frequently developed in the western portion of the Salt Lake Valley during VTMX that displayed a jet nose between 30-200 m AGL. While the development of the southerly jet was primarily attributed to regional-scale thermal contrasts, its strength and timing was modulated by the synoptic scale conditions. When the synoptic scale conditions were favorable for a strong jet, outflows from east-west oriented subsidiary canyons of the Salt Lake Valley were reduced due to the turbulent mixing induced by the jet. Downslope flows in the vicinity of the jet were predominately easterly, but would often acquire a southerly cross slope component due to vertical transport of momentum from the jet. Furthermore, obstacle effects and waves due to flow interacting with terrain were more much more prevalent when the jet was present than nights when it was absent.

During one nocturnal period during the Terrain-Induced Rotor Experiment (Grubisič et al. 2008) in the Owens Valley, California, Schmidli et al. (2009) was able to identify three flow regimes at one time, stacked vertically, that were forced by

3 mechanisms operating on 3 separate scales. At the lowest levels of the valley, a northerly thermally driven flow was observed while near and above the top of the valley there was a synoptically driven northwesterly flow. Between these two layers existed a southerly flow that was attributable to pressure-driven channeling of the synoptically imposed pressure gradient. On another night, also with northwesterly flow aloft, the mid-level flow in the Owens Valley was northerly, strongly enhancing the low-level thermally driven flow. In this case the influence of pressure-driven channeling to produce southerly winds was overwhelmed by a pressure gradient associated with the passage of a cold front. The Owens Valley was found to be susceptible to a wide range of synoptic scale forcings originating in the mid-levels of the valley, which are directly superimposed on the low-level thermal forcing. The lower two levels could both differ substantially from the flows observed above the crest height of the Sierra Nevada.

1.4.3 Numerical Modeling of ABL Flows in Complex Terrain

Investigators have used numerical models to simulate many flow processes in complex terrain including channeled flows (Doran and Zhong 2000), mountain-plain circulations (Zängl and Chico 2006), valley flows (Chow et al. 2006), slope flows (Savage III et al. 2008; Zhong and Whiteman 2008), and dynamically induced flows (Colle and Mass 1998; Epifanio and Rotunno 2005; Lawson and Horel 2015). These simulations have been conducted in idealized, semi-idealized, and real situations.

Since the near-surface wind is modulated by the structure of the ABL, high-quality simulations of wind depend on an accurate representation of the ABL structure. In general, numerical models struggle to accurately simulate the structure of daytime mixed layers and nocturnal stable layers. Numerical simulations of the mixed layer tend to be too shallow (Zhong and Fast 2003) and are sensitive to numerous model parameterizations (LeMone et al. 2012), although the sensitivity is less than that of the SBL (Steeneveld et al. 2008). The dependence of the SBL on local, often turbulent,

small-scale processes causes numerical simulations of SBLs to be particularly sensitive (Holtslag et al. 2013), usually resulting in simulated SBLs that are too deep with excessive vertical mixing (Hanna and Yang 2001).

Numerical model performance in complex terrain is dependent on application. Forecasts made at long lead times can benefit from the presence of terrain as the systematic topographic forcing causes relatively flat error growth with time (Vukicevic and Errico 1990). However, numerical simulations at short lead times in complex terrain tend to be poor, and in some cases, worse than over homogeneous terrain (Rife et al. 2004; Hart et al. 2005; Berg and Zhong 2005; Jiménez and Dudhia 2013).

Higher spatial resolution does not always benefit numerical simulations in complex terrain (Mass et al. 2002). While Rife and Davis (2005) found that high horizontal resolution benefitted forecasts of light winds, Zhang et al. (2013) found no benefit of increasing resolution from 3.3 km to 1.1 km for simulations of wind speed and direction over DPG.

Initial or boundary condition errors can be the source of poor forecasts of flows in complex terrain (Reinecke and Durran 2009b; Lombardo et al. 2016). Furthermore, areas downstream of complex terrain are in some cases more sensitive to initial condition errors in the upstream complex terrain than in upstream areas of flat terrain (Bieringer et al. 2012).

While numerical model performance regarding ABL processes has improved substantially in the last decades, work remains to improve parameterizations and other model components (Holtslag et al. 2013). Model improvements must be made carefully, as modifications made to improve the representation of certain processes can be detrimental to others. For instance, a change made to the vertical diffusion scheme of the European Centre for Medium Range Weather Forecasts global model to reduce an excessive dissipation of stratocumulus clouds caused mean nocturnal temperature errors in the model to increase to pre-1997 levels (Holtslag et al. 2013). Such unintended consequences necessitate a thorough understanding of the mechanisms

that are poorly simulated, such that model changes can be targeted and unintended consequences minimized.

In a related idea, Banta et al. (2004) emphasize the need not just for a numerical model that can accurately reproduce a feature under specific conditions, but for a model that changes that feature accurately as external conditions change. To accomplish the latter it is necessary to know how external conditions change that feature in the real atmosphere. A long and comprehensive set of observations is necessary to perform this task, and the fundamental mechanisms driving the feature must be understood.

1.4.4   Diagnosing Flow Mechanisms

Diagnosing the exact forcing mechanism for a given flow is a task complicated by the many possible mechanisms and their combinations, whether one is seeking to establish the mechanism forcing an observed flow or seeking to observe flows forced by a given mechanism. In both of these situations case studies can be combined with numerical simulations to elucidate the forcing mechanisms of a given flow. Case studies are often conducted during periods where large-scale weather conditions are expected to be conducive to a specific flow and to the mechanism forcing it. In these cases, it is important that the large-scale conditions are characterized carefully. Large scale conditions are often characterized by simple objective measures such as upper level wind speed thresholds (Fernando et al. 2015), or subjective assessments such as "anticyclonic conditions prevailed" (Rife et al. 2002), or a mix of the two (Zhang et al. 2013). In this work, no categorization of synoptic forcing will be made, as such a determination did not clearly delineate the actual flows observed. However, a robust measure of the meso-α and larger atmospheric flows is necessary for this work. To do so, wind and geopotential height fields at multiple levels from the ERA-Interim global atmospheric reanalysis will be used. The ERA-Interim has an effective horizontal resolution of approximately 79-km and 60 vertical levels and was chosen

in lieu of the National Centers for Environmental Prediction/National Center for Atmospheric Reasearch Reanalysis or the North American Regional Reanalysis due to its superior performance in the Intermountain West (Jeglum et al. 2010). At 79-km resolution the ERA-Interim does not resolve individual mountain ranges in the DPG area, although it does resolve the north-south oriented basin which is occupied by the Great Salt Lake and Great Salt Lake desert, with higher terrain to the west, south, and east.

In a similar fashion to selecting the preferred large-scale conditions, a specific terrain feature can be selected to isolate a specific flow and forcing mechanism. While this is often effective for isolating a given forcing mechanism it still relies on *a priori* assumptions of the flows that will be observed. For instance, the first Meteor Crater Experiment was designed to study cold-air pools and seiches in the Meteor Crater in Arizona due to the expectation that such ideal topography would effectively isolate the crater atmosphere from exterior influences (Whiteman et al. 2008). Field observations showed that the crater atmosphere was frequently disturbed by flows from outside the crater, even when the large-scale conditions were favorable for isolation of the crater atmosphere, and several unexpected flows and forcing mechanisms have subsequently been identified (Lehner et al. 2015b).

Numerical model simulations can be useful for relating a given flow to a specific forcing mechanism. Advances in numerical modeling and computing speed have allowed researchers to test forcing mechanisms more effectively by conducting many simulations, with changes to features such as the terrain, land surface, or model parameterizations (Rife et al. 2002; Alcott and Steenburgh 2013; Dimitrova et al. 2015). Such tests provide the most effective "control" possible in studies of the atmosphere. Numerical simulations can also be useful for filling in gaps in the observational network if a sufficiently accurate simulation can be made, such as in Schmidli et al. (2009).

Utilization of long periods of observations can offer several benefits over case stud-

ies for diagnosing flow mechanisms. First, a long observational record can establish whether a particular phenomenon is climatologically frequent. Second, a long observational record enables an understanding how that phenomenon changes under various external conditions. By assessing a range of external conditions, likely forcing mechanisms can be established more precisely. This work will observe changes in climatologically persistent flows through the diurnal and seasonal cycles over multiple years. While this method still cannot definitively attribute a flow to a forcing mechanism, it can provide evidence for attributing a climatologically persistent flow regime to a given forcing mechanism.

1.5 Large Surface Temperature Fluctuations

Large temperature fluctuations (LTFs), defined as a temperature drop of at least $3\,^{\circ}$C in 30 min followed by a recovery of at least half the initial drop withing one hour, are a frequent occurence at DPG. LTFs are a surface manifestation of important flow processes in the ABL, and understanding the mechanisms that cause them elucidates important multiscale flow interactions at DPG. This section will review observations of LTFs in the literature and discuss the potential processes producing them.

Causal mechanisms that have been identified for LTFs in the literature fall into two main categories. The first category is movement of a mobile boundary. This category includes slope and valley flow fronts and pulses (Doran and Horst 1981; Blumen et al. 1999), synoptic fronts (Shafer and Steenburgh 2008), and convective outflows (Mueller and Carbone 1987; Johnson et al. 2014). In these cases cold air travels along the ground with the character of a density current (Liu and Moncrieff 2000). The second category is the disturbance of a quasistationary boundary. Differential cooling of the nocturnal SBL in complex terrain readily produces mesoscale and microscale temperature gradients (Steyn et al. 2013), and the disturbance of a quasistationary boundary often takes the form of the displacement of a surface-based stable layer that intersects a slope (Mahrt et al. 2014). Propagating gravity waves (Brown et al.

2003; Viana et al. 2009), solitary waves (Cheung and Little 1990), seiches (Whiteman et al. 2008), and turbulent wakes in the lee of terrain (Epifanio and Rotunno 2005) are known to create such a disturbance. In some cases, the SBL is important not just for the presence of strong temperature contrasts but also for providing a medium by which disruptive mechanisms may travel.

The two categories, mobile and quasistationary boundaries, are not independent as it is possible for a mobile boundary to disturb a quasistationary boundary. Of the mechanisms described here, only two (synoptic fronts and convective outflows) would operate in the absence of a SBL. It is then not surprising that a large majority of investigators have found LTFs to occur during the nocturnal period.

1.5.1 Wave Motions in Stratified Flow

Wave motions are the mechanism responsible for causing LTFs in a number of the studies mentioned above. A stratified atmosphere is necessary to develop wave motions and, as a result, LTFs due to wave motions are primarily limited to the nocturnal period. Common triggers for atmospheric wave motions include the interaction of flow with topography (Epifanio 2003), convection (Stull 1976), and flow collisions (Lin et al. 1993). Waves can be induced locally, such as small motions in a very shallow stable layer (Viana et al. 2010), or travel from relatively remote locations, such as with lee wave trains, hundred of kilometers long (Grubišić and Billings 2008).

The impact of local topography on wave motions is complex. In the case of flow impinging on a terrain barrier, the resulting motions are highly dependent on the speed and stratification of the flow, the height and aspect ratio of the barrier, the incident direction of the flow, and the degree of stationarity of the flow. The non-dimensional mountain height

$$\epsilon = \frac{Nh_0}{U} \tag{1.1}$$

is the primary metric used to diagnose the nature of flow interaction with a topographic obstacle. In this equation

$$N = \sqrt{\frac{g}{\theta}\frac{d\theta}{dz}} \qquad (1.2)$$

is the Brunt-Vaisala frequency, a measure of the static stability, U is the wind speed and h_0 is the terrain height. The inverse of the nondimensional mountain height is the Froude number. A second parameter, β, that is commonly used in conjunction with ϵ expresses the horizontal aspect ratio of the barrier with large β indicating mountains elongated in the cross-flow direction.

Application of these metrics to idealized simulations with constant upstream stratification and wind speeds is straightforward. It is more difficult in heterogeneous real world cases. Reinecke and Durran (2008) evaluated both bulk and layer-averaging methods for computing accurate ϵ values from observed soundings. Neither method was found to be superior for all applications, but the bulk method proved best for predicting the onset of low-level flow diversion.

Fig. 1.2 shows the phase diagram relating flow regimes to different values of ϵ and β. For $\epsilon \ll 1$ the flow, even at low levels, will freely ascend the obstacle. For $\epsilon \gg 1$ substantial blocking of the flow will occur below the top of the terrain. This blocking can lead to flow splitting and lee vortices.

Not all wave motions are likely to produce LTFs. To produce an LTF, the motion must either substantially disturb a pre-existing CAP or create a strong surface temperature gradient. Flows occupying the lower-right section of Fig. 1.2 are unlikely to do this. In a case such as a high-amplitude breaking wave, the conditions necessary to support formation of the wave would tend to remove a CAP unless the CAP is too strong or replenished by forces operating on the synoptic scale, such as when a polar
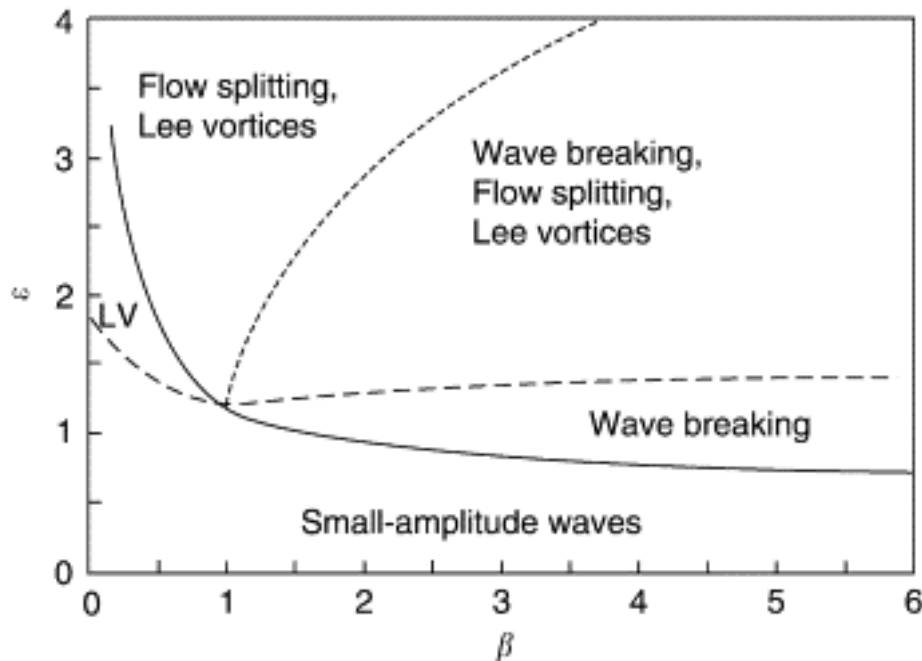
Fig. 1.2. Regime diagram for stratified flow past an isolated ridge as a function of ϵ and β. Reprinted from Epifanio (2003). ©2003 Elsevier. Reprinted with permission.

air mass is dammed against the east side of the Rocky Mountains (Lee et al. 1989).

Flows occupying the upper-left section of Fig. 1.2 are conducive to developing conditions necessary for LTFs as they display the upstream blocking of the low-level flow that is beneficial for producing strong surface temperature gradients. Epifanio and Rotunno (2005) conducted idealized simulations of flow impinging on a terrain barrier with $\epsilon = 4$, $\beta = 3$ and the stratified layer limited to $0.6h_0$ and below, a situation similar to conditions typically observed near GM. In this situation the low-level flow is blocked, forming an orographic wake which causes potentially warm air from crest height to descend in the lee of the barrier. The descending warm air combined with the low-level stratification produces a strong thermal gradient on the lower slope of the barrier. The strong thermal gradient in the lee of the barrier propagates forward relative to the flow (stationary with respect to the mountain) in the manner of a density current. The location of the thermal gradient can fluctuate due to vertical-axis eddies that form on the edges of the barrier or due to nonstationarity of the

flow. Despite substantial work using idealized numerical simulations on this these phenomena, observations are relatively rare (Adler and Kalthoff 2015).

1.5.2 LTFs at DPG

LTFs have previously been observed at DPG by several investigators. Lehner et al. (2015a) observed temperature drops on the East Slope of GM of up to $10\,°\text{C}$ in 20 min during what were considered to be quiescent conditions. Four such LTFs dominated the latter half of the nocturnal period. Fernando et al. (2015) identified similar LTFs on the East Slope on the night of 1-2 October 2012. In both cases LTFs were attributed to the convergence of southwesterly flow through the Gap and southeasterly flow in the east basin that result in the east basin CAP being displaced up the East Slope, although this hypothesis was not investigated in depth.

Two years of numerical model simulations over DPG were used by Serafin et al. (2016) to conclude that stratified flow interacting with GM was the cause of temperature perturbations on the East Slope of GM. While the authors do not explicitly identify LTFs, they calculate the gradient magnitude of temperature over the full DPG domain, a measure of the mean strength of the horizontal thermal gradient. The highest values of this metric over the 2-year period occurred on the east and northeast sides of GM and the Dugway Range, which is immediately southeast of GM. Additionally, they found a relatively high correlation between surface temperature perturbations and zonal wind on the East Slope of GM. With this evidence the authors concluded that strong temperature gradients are produced by the dynamic acceleration of flows down GM that interact with the relatively cold drainage flow over the east basin.

1.5.3 Numerical Model Configuration

The Weather Research and Forecasting (WRF) model (Skamarock et al. 2008) will be used in this work to simulate flows in the vicinity of GM for the purpose of di-

agnosing LTF forcing mechanisms. Careful consideration must be given to the model configuration when attempting to resolve LTF-related flows in complex terrain. Many of the potential LTF forcing mechanisms discussed above operate on horizontal scales of approximately 1-10 km, and GM itself is approximately 5 km wide. According to Skamarock and Klemp (2008), WRF grid spacing should be a minimum of $4\Delta x$ and preferably $6 - 8\Delta x$ to adequately resolve a given phenomenon. Caution also must be exercised when using high horizontal resolution in a domain with terrain as steep as GM, as steep slopes can cause numerical instabilities in the model (Lundquist et al. 2012).

The model configuration used here is identical to that in Dimitrova et al. (2015) with a horizontal resolution of 500 m and 50 vertical levels (22 levels below 600 m). Physical parameterizations include the Quasi-Normal Scale Elimination (QNSE) planetary boundary layer scheme (Sukoriansky et al. 2005), the Lin et al. (1983) microphysical scheme, the RRTM longwave radiation parametrization (Mlawer et al. 1997), and the Dudhia shortwave radiation parametrization (Dudhia 1989). The model also included the improved land cover and Noah land-surface model as described in Massey et al. (2014).

In their assessment of planetary boundary layer scheme skill on the East Slope at DPG, (Dimitrova et al. 2015) found that the QNSE best reproduced the sharp temperature and wind-speed gradients near the ground that are common near the East Slope of GM, as well as other characteristics of the planetary boundary layer. Representation of such gradients will be critical to analyzing LTFs.

The WRF simulations will be used to visualize orographic wakes in the lee of GM, which extend roughly from the crest of GM 6-10 km. The 500 m horizontal resolution being used is sufficient to resolve the orographic wake as well as any other phenomenon with a horizontal scale of at least 3 km. This resolution compares favorably to the effective resolution of idealized numerical simulations of orographic wakes such as those in Epifanio and Rotunno (2005). A fifth-order horizontal advection scheme

should avoid over-amplification errors in the simulation of mountain waves (Reinecke and Durran 2009a).

1.6 Objectives and Outline

This work examines ABL flows in complex terrain at DPG, using both observations and numerical simulations, for the purpose of increasing our understanding of flow interactions on multiple scales in complex terrain.

Chapter 2 of this dissertation examines flows across DPG on spatial scales from meso-γ to synoptic and temporal scales from hourly to seasonal. Surface winds at DPG are shown to display a bimodal distribution of direction that is not primarily forced by thermally driven flows. The two modes of this bimodal distribution are called the Southerly Regime and the Northerly Regime, indicating the predominate flow direction in each regime. The regimes and their seasonal distribution are shown to arise primarily due to mechanisms operating on the mesoscale and synoptic scale that include thermal low pressure and the Great Basin Confluence Zone.

Chapter 3 examines the spatial and temporal distribution of LTFs at DPG and identify the mechanisms that produce them. LTFs are shown to occur preferentially on slopes surrounding the east basin, particularly on the East Slope of GM. The cause of the LTFs on the East Slope are shown to be an orographic wake that arises due to a persistent nocturnal southwesterly flow that impinges on GM. This wake magnifies the preexisting CAP thermal gradient on the East Slope of GM. LTFs are then produced by displacement of the CAP due to variations in the impinging flow and the generation of vertical-axis eddies over the East Slope.

Chapter 4 presents a summary of this work and will propose future research.

1.7 References

Adler, B., and N. Kalthoff, 2015: The impact of upstream flow on the atmospheric boundary layer in a valley on a mountainous island. *Bound.-Layer Meteor.*, **158**,

429–452, doi:10.1007/s10546-015-0092-y.

Alcott, T. I., and W. J. Steenburgh, 2013: Orographic influences on a Great Salt Lake–effect snowstorm. *Mon. Wea. Rev.*, **141**, 2432–2450, doi:10.1175/MWR-D-12-00328.1.

Angevine, W. M., H. K. Baltink, and F. C. Bosveld, 2001: Observations of the morning transition of the convective boundary layer. *Bound.-Layer Meteor.*, **101**, 209–227, doi:10.1023/A:1019264716195.

Banta, R. M., L. S. Darby, J. D. Fast, J. O. Pinto, C. D. Whiteman, W. J. Shaw, and B. W. Orr, 2004: Nocturnal low-level jet in a mountain basin complex. Part 1: Evolution and effects on local flows. *J. Appl. Meteor*, **43**, 1348–1365, doi: 10.1175/JAM2142.1.

Banta, R. M., L. Mahrt, D. Vickers, J. Sun, B. B. Balsley, Y. L. Pichugina, and E. J. Williams, 2007: The very stable boundary layer on nights with weak low-level jets. *J. Atmos. Sci.*, **64**, 3068–3090, doi:10.1175/JAS4002.1.

Berg, L. K., and S. Zhong, 2005: Sensitivity of MM5-simulated boundary layer characteristics to turbulence parameterizations. *J. Appl. Meteor*, **44**, 1467–1483, doi: 10.1175/JAM2292.1.

Bieringer, P. E., P. S. Ray, and A. J. Annunzio, 2012: The effect of topographic variability on initial condition sensitivity of low-level wind forecasts. Part I: Experiments using idealized terrain. *Mon. Wea. Rev.*, **141**, 2137–2155, doi:10.1175/MWR-D-11-00054.1.

Blumen, W., R. L. Grossman, and M. Piper, 1999: Analysis of heat budget, dissipation and frontogenesis in a shallow density current. *Bound.-Layer Meteor.*, **91**, 281–306, doi:10.1023/A:1001813700928.

Bossert, J. E., and W. R. Cotton, 1994: Regional-scale flows in mountainous terrain. Part I: A numerical and observational comparison. *Mon. Wea. Rev.*, **122**, 1449–1471, doi:10.1175/1520-0493(1994)122<1449:RSFIMT>2.0.CO;2.

Brown, A. R., M. Athanassiadou, and N. Wood, 2003: Topographically induced waves within the stable boundary layer. *Quart. J. Roy. Meteor. Soc.*, **129**, 3357–3370, doi: 10.1256/qj.02.176.

Butler, B., J. Forthofer, M. Finney, L. Bradshaw, and R. Stratton, 2006: High resolution wind direction and speed information for support of fire operations. Tech. Rep. RMRS-P-42CD, U.S. Forest Service Proceedings.

Cheung, T. K., and C. G. Little, 1990: Meteorological tower, microbarograph array, and sodar observations of solitary-like waves in the nocturnal boundary layer. *J. Atmos. Sci.*, **47**, 2516–2536, doi:10.1175/1520-0469(1990)047<2516:MTMAAS>2.0.CO;2.

Chow, F. K., A. P. Weigel, R. L. Street, M. W. Rotach, and M. Xue, 2006: High-resolution large-eddy simulations of flow in a steep alpine valley. Part I: Methodology, verification, and sensitivity experiments. *J. Appl. Meteor. Climatol.*, **45**, 63–86, doi:10.1175/JAM2322.1.

Clements, C. B., C. D. Whiteman, and J. D. Horel, 2003: Cold-air-pool structure and evolution in a mountain basin: Peter Sinks, Utah. *J. Appl. Meteor*, **42**, 752–768.

Coen, J. L., M. Cameron, J. Michalakes, E. G. Patton, P. J. Riggan, and K. M. Yedinak, 2012: WRF-fire: Coupled weather–wildland fire modeling with the Weather Research and Forecasting Model. *J. Appl. Meteor. Climatol.*, **52**, 16–38, doi: 10.1175/JAMC-D-12-023.1.

Colle, B. A., and C. F. Mass, 1998: Windstorms along the western side of the Washington Cascade Mountains. Part II: Characteristics of past events and three-dimensional idealized simulations. *Mon. Wea. Rev.*, **126**, 53–71, doi:10.1175/1520-0493(1998)126<0053:WATWSO>2.0.CO;2.

Coulter, R. L., and P. Gudiksen, 1995: The dependence of canyon winds on surface cooling and external forcing in colorado's front range. *J. Appl. Meteor*, **34**, 1419–1429, doi:10.1175/1520-0450(1995)034<1419:TDOCWO>2.0.CO;2.

Davis, A., and R. McNider, 1997: The development of Antarctic katabatic winds and implications for the coastal ocean. *J. Atmos. Sci.*, **54**, 1248–1261.

De Wekker, S. F. J., D. G. Steyn, and S. Nyeki, 2004: A comparison of aerosol-layer and convective boundary-layer structure over a mountain range during Staaarte '97. *Bound.-Layer Meteor.*, **113**, 249–271, doi:10.1023/B:BOUN.0000039371.41823.37.

Dimitrova, R., Z. Silver, T. Zsedrovits, C. Hocut, L. Leo, S. Di Sabatino, and H. S. Fernando, 2015: Assessment of planetary boundary-layer schemes in the weather research and forecasting mesoscale model using MATERHORN field data. *Bound.-Layer Meteor.*, 1–21, doi:10.1007/s10546-015-0095-8.

Doran, J., J. D. Fast, and J. Horel, 2002: The VTMX 2000 campaign. *Bull. Amer. Meteor. Soc.*, **83**, 537–551.

Doran, J. C., and T. W. Horst, 1981: Velocity and temperature oscillations in drainage winds. *J. Appl. Meteor*, **20**, 361–364, doi:10.1175/1520-0450(1981)020<0361:VATOID>2.0.CO;2.

Doran, J. C., T. W. Horst, and C. D. Whiteman, 1990: The development and structure of nocturnal slope winds in a simple valley. *Bound.-Layer Meteor.*, **52**, 41–68, doi:10.1007/BF00123177.

Doran, J. C., and S. Zhong, 2000: Thermally driven gap winds into the Mexico City Basin. *J. Appl. Meteor*, **39**, 1330–1340, doi:10.1175/1520-0450(2000)039<1330:TDGWIT>2.0.CO;2.

Doyle, J. D., C. C. Epifanio, A. Persson, P. A. Reinecke, and G. Zängl, (Eds.), 2013: *Mountain Weather Research and Forecasting: Recent Progress and Current Challenges*, chap. Mesoscale Modeling over Complex Terrain: Numerical and Predictability Perspectives. Springer Netherlands.

Dudhia, J., 1989: Numerical study of convection observed during the winter monsoon experiment using a mesoscale two-dimensional model. *J. Atmos. Sci.*, **46**, 3077–3107, doi:10.1175/1520-0469(1989)046<3077:NSOCOD>2.0.CO;2.

Eckman, R. M., 1998: Observations and numerical simulations of winds within a broad forested valley. *J. Appl. Meteor*, **37**, 206–219, doi:10.1175/1520-0450(1998)037<0206:OANSOW>2.0.CO;2.

Epifanio, C. C., 2003: *Lee Vortices*, 1150–1160. Academic Press, Oxford, doi: http://dx.doi.org/10.1016/B0-12-227090-8/00241-4.

Epifanio, C. C., and R. Rotunno, 2005: The dynamics of orographic wake formation in flows with upstream blocking. *J. Atmos. Sci.*, **62**, 3127–3150, doi: 10.1175/JAS3523.1.

Fernando, H. J. S., and Coauthors, 2015: The MATERHORN - unraveling the intricacies of mountain weather. *Bull. Amer. Meteor. Soc.*, doi:10.1175/BAMS-D-13-00131.1.

Frei, C., and H. C. Davies, 1993: Anomaly in the Alpine diurnal pressure signal: Observations and theory. *Quart. J. Roy. Meteor. Soc.*, **119**, 1269–1289, doi: 10.1002/qj.49711951403.

Grachev, A. A., L. S. Leo, S. D. Sabatino, H. J. S. Fernando, E. R. Pardyjak, and C. W. Fairall, 2015: Structure of turbulence in katabatic flows below and above the wind-speed maximum. *Bound.-Layer Meteor.*, 1–26, doi:10.1007/s10546-015-0034-8.

Gross, G., and F. Wippermann, 1987: Channeling and countercurrent in the upper Rhine Valley: Numerical simulations. *J. Clim. Appl. Meteor.*, **26**, 1293–1304, doi: 10.1175/1520-0450(1987)026<1293:CACITU>2.0.CO;2.

Grubišić, V., and B. J. Billings, 2008: Climatology of the Sierra Nevada mountain-wave events. *Mon. Wea. Rev.*, **136**, 757–768, doi:10.1175/2007MWR1902.1.

Grubisič, V., and Coauthors, 2008: The Terrain-Induced Rotor Experiment: A field campaign overview including observational highlights. *Bull. Amer. Meteor. Soc.*, **89**, 1513–1533.

Gudiksen, P. H., J. M. Leone, C. W. King, D. Ruffieux, and W. D. Neff, 1992: Measurements and modeling of the effects of ambient meteorology on nocturnal drainage flows. *J. Appl. Meteor*, **31**, 1023–1032, doi:10.1175/1520-0450(1992)031<1023:MAMOTE>2.0.CO;2.

Hanna, S. R., and R. Yang, 2001: Evaluations of mesoscale models' simulations of near-surface winds, temperature gradients, and mixing depths. *J. Appl. Meteor*, **40**, 1095–1104, doi:10.1175/1520-0450(2001)040<1095:EOMMSO>2.0.CO;2.

Hart, K. A., W. J. Steenburgh, and D. J. Onton, 2005: Model forecast improvements with decreased horizontal grid spacing over finescale intermountain orography during the 2002 Olympic Winter Games. *Wea. Forecasting*, **20**, 558–576, doi:10.1175/WAF865.1.

Holtslag, A. A. M., and Coauthors, 2013: Stable atmospheric boundary layers and diurnal cycles: Challenges for weather and climate models. *Bull. Amer. Meteor. Soc.*, **94**, 1691–1706, doi:10.1175/BAMS-D-11-00187.1.

Jeglum, M. E., W. J. Steenburgh, T. P. Lee, and L. F. Bosart, 2010: Multi-reanalysis climatology of Intermountain Cyclones. *Mon. Wea. Rev.*, **138**, 4035–4053, doi:10.1175/2010MWR3432.1.

Jensen, D. D., D. F. Nadeau, S. W. Hoch, and E. R. Pardyjak, 2016: Observations of near-surface heat-flux and temperature profiles through the early evening transition over contrasting surfaces. *Bound.-Layer Meteor.*, 1–21, doi:10.1007/s10546-015-0067-z.

Jerrett, M., and Coauthors, 2005: Spatial analysis of air pollution and mortality in Los Angeles. *Epidemiology*, **16**, 727–736.

Jiménez, P. A., and J. Dudhia, 2013: On the ability of the WRF model to reproduce the surface wind direction over complex terrain. *J. Appl. Meteor. Climatol.*, **52**, 1610–1617, doi:10.1175/JAMC-D-12-0266.1.

Johnson, R. H., R. S. Schumacher, J. H. R. Jr., D. T. Lindsey, J. E. Ruthford, and L. Kriederman, 2014: The role of convective outflow in the Waldo Canyon Fire. *Mon. Wea. Rev.*, **142**, 3061–3080, doi:10.1175/MWR-D-13-00361.1, `http://dx.doi.org/10.1175/MWR-D-13-00361.1`.

Kalthoff, N., C. Kottmeier, J. Thurauf, U. Corsmeier, F. Said, E. Fréjafon, and P. E. Perros, 2005: Mesoscale circulation systems and ozone concentrations during ESCOMPTE: a case study from IOP 2b. *Atmos. Res.*, **74**, 355–380, doi:http://dx.doi.org/10.1016/j.atmosres.2004.04.006.

Kossmann, M., R. Vogtlin, U. Corsmeier, B. Vogel, F. Fiedler, H. J. Binder, N. Kalthoff, and F. Beyrich, 1998: Aspects of the convective boundary layer structure over complex terrain. *Atmos. Envir.*, **32**, 1323–1348, doi:http://dx.doi.org/10.1016/S1352-2310(97)00271-9.

Kraus, H., J. Malcher, and E. Schaller, 1985: A nocturnal low level jet during PUKK. *Bound.-Layer Meteor.*, **31**, 187–195, doi:10.1007/BF00121177.

Lareau, N. P., E. Crosman, C. D. Whiteman, J. D. Horel, S. W. Hoch, W. O. Brown,

and T. W. Horst, 2013: The Persistent Cold-Air Pool Study. *Bull. Amer. Meteor. Soc.*, **94**, 51–63.

Lareau, N. P., and J. D. Horel, 2012: The climatology of synoptic-scale ascent over western North America: A perspective on storm tracks. *Mon. Wea. Rev.*, **140**, 1761–1778, doi:10.1175/MWR-D-11-00203.1.

Lareau, N. P., and J. D. Horel, 2014: Turbulent erosion of persistent cold-air pools: Numerical simulations. *J. Atmos. Sci.*, **72**, 1409–1427, doi:10.1175/JAS-D-14-0173.1.

Lawson, J., and J. Horel, 2015: Ensemble forecast uncertainty of the 1 December 2011 Wasatch windstorm. *Wea. Forecasting*, **30**, 1749–1761, doi:10.1175/WAF-D-15-0034.1.

Lee, T. J., R. A. Pielke, R. C. Kessler, and J. Weaver, 1989: Influence of cold pools downstream of mountain barriers on downslope winds and flushing. *Mon. Wea. Rev.*, **117**, 2041–2058, doi:10.1175/1520-0493(1989)117<2041:IOCPDO>2.0.CO;2.

Lehner, M., C. D. Whiteman, S. W. Hoch, D. Jensen, E. R. Pardyjak, L. S. Leo, S. Di Sabatino, and H. J. S. Fernando, 2015a: A case study of the nocturnal boundary layer evolution on a slope at the foot of a desert mountain. *J. Appl. Meteor. Climatol.*, **54**, 732–751, doi:10.1175/JAMC-D-14-0223.1.

Lehner, M., and Coauthors, 2015b: The METCRAX II field experiment: A study of downslope windstorm-type flows in Arizona's Meteor Crater. *Bull. Amer. Meteor. Soc.*, **97**, 217–235, doi:10.1175/BAMS-D-14-00238.1.

LeMone, M. A., M. Tewari, F. Chen, and J. Dudhia, 2012: Objectively determined fair-weather CBL depths in the ARW-WRF model and their comparison to CASES-97 observations. *Mon. Wea. Rev.*, **141**, 30–54, doi:10.1175/MWR-D-12-00106.1.

Li, S., L. Zhang, S. Kang, L. Tong, T. Du, X. Hao, and P. Zhao, 2015: Comparison of several surface resistance models for estimating crop evapotranspiration over the entire growing season in arid regions. *Agric. For. Meteor*, **208**, 1–15, doi: http://dx.doi.org/10.1016/j.agrformet.2015.04.002.

Li, Y., and R. B. Smith, 2010: Observation and theory of the diurnal continental thermal tide. *J. Atmos. Sci.*, **67**, 2752–2765, doi:10.1175/2010JAS3384.1.

Lin, Y.-L., R. D. Farley, and H. D. Orville, 1983: Bulk parameterization of the snow field in a cloud model. *J. Clim. Appl. Meteor.*, **22**, 1065–1092, doi:10.1175/1520-0450(1983)022<1065:BPOTSF>2.0.CO;2.

Lin, Y.-L., T.-A. Wang, and R. P. Weglarz, 1993: Interactions between gravity waves and cold air outflows in a stably stratified uniform flow. *J. Atmos. Sci.*, **50**, 3790–3816, doi:10.1175/1520-0469(1993)050<3790:IBGWAC>2.0.CO;2.

Liu, C., and M. W. Moncrieff, 2000: Simulated density currents in idealized stratified environments. *Mon. Wea. Rev.*, **128**, 1420–1437, doi:10.1175/1520-0493(2000)128<1420:SDCIIS>2.0.CO;2.

Liu, Y., and Coauthors, 2008: The operational mesogamma-scale analysis and forecast system of the U.S. Army Test and Evaluation Command. Part I: Overview of the modeling system, the forecast products, and how the products are used. *J. Appl. Meteor. Climatol.*, **47**, 1077–1092, doi:10.1175/2007JAMC1653.1.

Lombardo, K., E. Sinsky, Y. Jia, M. M. Whitney, and J. Edson, 2016: Sensitivity of simulated sea breezes to initial conditions in complex coastal regions. *Mon. Wea. Rev.*, **144**, 1299–1320, doi:10.1175/MWR-D-15-0306.1.

Lundquist, K. A., F. K. Chow, and J. K. Lundquist, 2012: An immersed boundary method enabling large-eddy simulations of flow over complex terrain in the WRF model. *Mon. Wea. Rev.*, **140**, 3936–3955, doi:10.1175/MWR-D-11-00311.1.

Mahrt, L., J. Sun, S. P. Oncley, and T. W. Horst, 2014: Transient cold air drainage down a shallow valley. *J. Atmos. Sci.*, **71**, 2534–2544, doi:10.1175/JAS-D-14-0010.1.

Mass, C. F., D. Ovens, K. Westrick, and B. A. Colle, 2002: Does increasing horizontal resolution produce more skillful forecasts? *Bull. Amer. Meteor. Soc.*, **83**, 407–430, doi:10.1175/1520-0477(2002)083<0407:DIHRPM>2.3.CO;2.

Massey, J. D., W. J. Steenburgh, S. W. Hoch, and J. C. Knievel, 2014: Sensitivity of near-surface temperature forecasts to soil properties over a sparsely vegetated dryland region. *J. Appl. Meteor. Climatol.*, **53**, 1976–1995, doi:10.1175/JAMC-D-13-0362.1.

McGowan, H. A., and A. P. Sturman, 2013: Interacting multi-scale wind systems within an alpine basin, Lake Tekapo, New Zealand. *Meteor. Atmos. Phys.*, **58**, 165–177, doi:10.1007/BF01027563.

McKee, T. B., and R. D. O'Neal, 1989: The role of valley geometry and energy budget in the formation of nocturnal valley winds. *J. Appl. Meteor*, **28**, 445–456, doi:10.1175/1520-0450(1989)028<0445:TROVGA>2.0.CO;2.

Mlawer, E. J., S. J. Taubman, P. D. Brown, M. J. Iacono, and S. A. Clough, 1997: Radiative transfer for inhomogeneous atmospheres: RRTM, a validated correlated-k model for the longwave. *J. Geo. Res. Atmos.*, **102**, 16 663–16 682, doi:10.1029/97JD00237.

Mueller, C. K., and R. E. Carbone, 1987: Dynamics of a thunderstorm outflow. *J. Atmos. Sci.*, **44**, 1879–1898, doi:10.1175/1520-0469(1987)044<1879:DOATO>2.0.CO;2.

Petkovšek, Z., 1992: Turbulent dissipation of cold air lake in a basin. *Meteor. Atmos. Phys.*, **47**, 237–245, doi:10.1007/BF01025620.

Pichugina, Y. L., and R. M. Banta, 2010: Stable boundary layer depth from high-resolution measurements of the mean wind profile. *J. Appl. Meteor. Climatol.*, **49**, 20–35, doi:10.1175/2009JAMC2168.1.

Pino, D., J. Vilà-Guerau de Arellano, and P. G. Duynkerke, 2003: The contribution of shear to the evolution of a convective boundary layer. *J. Atmos. Sci.*, **60**, 1913–1926, doi:10.1175/1520-0469(2003)060<1913:TCOSTT>2.0.CO;2.

Rampanelli, G., D. Zardi, and R. Rotunno, 2004: Mechanisms of up-valley winds. *J. Atmos. Sci.*, **61**, 3097–3111, doi:10.1175/JAS-3354.1.

Reinecke, P. A., and D. Durran, 2009a: The overamplification of gravity waves in numerical solutions to flow over topography. *Mon. Wea. Rev.*, **137**, 1533–1549, doi:10.1175/2008MWR2630.1.

Reinecke, P. A., and D. R. Durran, 2008: Estimating topographic blocking using a Froude number when the static stability is nonuniform. *J. Atmos. Sci.*, **65**, 1035–1048, doi:10.1175/2007JAS2100.1.

Reinecke, P. A., and D. R. Durran, 2009b: Initial-condition sensitivities and the predictability of downslope winds. *J. Atmos. Sci.*, **66**, 3401–3418, doi:10.1175/2009JAS3023.1.

Rife, D. L., and C. A. Davis, 2005: Verification of temporal variations in mesoscale numerical wind forecasts. *Mon. Wea. Rev.*, **133**, 3368–3381, doi:10.1175/MWR3052.1.

Rife, D. L., C. A. Davis, Y. Liu, and T. T. Warner, 2004: Predictability of low-level winds by mesoscale meteorological models. *Mon. Wea. Rev.*, **132**, 2553–2569, doi:10.1175/MWR2801.1.

Rife, D. L., T. T. Warner, F. Chen, and E. G. Astling, 2002: Mechanisms for diurnal boundary layer circulations in the Great Basin Desert. *Mon. Wea. Rev.*, **130**, 921–938, doi:10.1175/1520-0493(2002)130<0921:MFDBLC>2.0.CO;2.

Rucker, M., R. M. Banta, and D. G. Steyn, 2008: Along-valley structure of daytime thermally driven flows in the Wipp Valley. *J. Appl. Meteor. Climatol.*, **47**, 733–751, doi:10.1175/2007JAMC1319.1.

Sastre, M., C. Yagüe, C. Román-Cascón, and G. Maqueda, 2015: Atmospheric boundary-layer evening transitions: A comparison between two different experimental sites. *Bound.-Layer Meteor.*, **157**, 375–399, doi:10.1007/s10546-015-0065-1.

Savage III, L. C., S. Zhong, W. Yao, W. J. Brown, T. W. Horst, and C. D. Whiteman, 2008: An observational and numerical study of a regional-scale downslope flow in northern Arizona. *J. Geophy. Res.*, **113**, D14 114.

Schmidli, J., G. S. Poulos, M. H. Daniels, and F. K. Chow, 2009: External influences on nocturnal thermally driven flows in a deep valley. *J. Appl. Meteor. Climatol.*,

48, 3–23, doi:10.1175/2008JAMC1852.1.

Schmidli, J., and R. Rotunno, 2010: Mechanisms of along-valley winds and heat exchange over mountainous terrain. *J. Atmos. Sci.*, **67**, 3033–3047, doi:10.1175/2010JAS3473.1.

Seaman, N. L., B. J. Gaudet, D. R. Stauffer, L. Mahrt, S. J. Richardson, J. R. Zielonka, and J. C. Wyngaard, 2011: Numerical prediction of submesoscale flow in the nocturnal stable boundary layer over complex terrain. *Mon. Wea. Rev.*, **140**, 956–977, doi:10.1175/MWR-D-11-00061.1.

Serafin, S., S. J. De Wekker, and J. Knievel, 2016: A mesoscale model-based climatography of nocturnal boundary-layer characteristics over the complex terrain of north-western Utah. *Bound.-Layer Meteor.*, 1–25, doi:10.1007/s10546-015-0044-6.

Shafer, J. C., and W. J. Steenburgh, 2008: Climatology of strong Intermountain cold fronts. *Mon. Wea. Rev.*, **136**, 784–807, doi:10.1175/2007MWR2136.1.

Skamarock, W., and Coauthors, 2008: A description of the Advanced Research WRF Version 3. Tech. Rep. NCAR/TN-475+STR, NCAR Technical Note.

Skamarock, W. C., and J. B. Klemp, 2008: A time-split nonhydrostatic atmospheric model for weather research and forecasting applications. *J. Comput. Phys.*, **227**, 3465–3485.

Steeneveld, G. J., T. Mauritsen, E. I. F. de Bruijn, J. Vilà-Guerau de Arellano, G. Svensson, and A. A. M. Holtslag, 2008: Evaluation of limited-area models for the representation of the diurnal cycle and contrasting nights in CASES-99. *J. Appl. Meteor. Climatol.*, **47**, 869–887, doi:10.1175/2007JAMC1702.1.

Steyn, D. G., S. F. J. De Wekker, M. Kossmann, and A. Martilli, (Eds.), 2013: *Mountain Weather Research and Forecasting: Recent Progress and Current Challenges*, chap. Boundary Layers and Air Quality in Mountainous Terrain. Springer Netherlands.

Stull, R., 1988: *An Introduction to Boundary Layer Meteorology*. Kluwer Academic Publishers.

Stull, R. B., 1976: Internal gravity waves generated by penetrative convection. *J. Atmos. Sci.*, **33**, 1279–1286, doi:10.1175/1520-0469(1976)033<1279:IGWGBP>2.0.CO;2.

Sukoriansky, S., B. Galperin, and I. Staroselsky, 2005: A quasinormal scale elimination model of turbulent flows with stable stratification. *Phys. Fluids*, **17**, 085107, doi:http://dx.doi.org/10.1063/1.2009010.

Tang, M., and E. R. Reiter, 1984: Plateau monsoons of the Northern Hemisphere:

A comparison between North America and Tibet. *Mon. Wea. Rev.*, **112**, 617–637, doi:10.1175/1520-0493(1984)112<0617:PMOTNH>2.0.CO;2.

Vergeiner, I., and E. Dreiseitl, 1987: Valley winds and slope winds: Observations and elementary thoughts. *Meteor. Atmos. Phys.*, **36**, 264–286, doi:10.1007/BF01045154.

Viana, S., E. Terradellas, and C. Yagüe, 2010: Analysis of gravity waves generated at the top of a drainage flow. *J. Atmos. Sci.*, **67**, 3949–3966, doi:10.1175/2010JAS3508.1.

Viana, S., C. Yagüe, and G. Maqueda, 2009: Propagation and effects of a mesoscale gravity wave over a weakly-stratified nocturnal boundary layer during the SABLES2006 field campaign. *Bound.-Layer Meteor.*, **133**, 165–188, doi:10.1007/s10546-009-9420-4.

Vukicevic, T., and R. M. Errico, 1990: The influence of artificial and physical factors upon predictability estimates using a complex limited-area model. *Mon. Wea. Rev.*, **118**, 1460–1482, doi:10.1175/1520-0493(1990)118<1460:TIOAAP>2.0.CO;2.

Wallace, J. M., and P. V. Hobbs, 1977: *Atmospheric Science: An Introductory Survey.* Academic Press, London, 467pp.

Whiteman, C. D., 1990: Observations of thermally developed wind systems in mountainous terrain. *Atmospheric Processes over Complex Terrain, Meteor. Monogr*, **23 (45)**, 5–42.

Whiteman, C. D., 2000: *Mountain Meteorology: Fundamentals and Applications.* Oxford University Press, New York, 355 pp.

Whiteman, C. D., and J. C. Doran, 1993: The relationship between overlying synoptic-scale flows and winds within a valley. *J. Appl. Meteor*, **32**, 1669–1682, doi:10.1175/1520-0450(1993)032<1669:TRBOSS>2.0.CO;2.

Whiteman, C. D., S. W. Hoch, J. D. Horel, and A. Charland, 2014: Relationship between particulate air pollution and meteorological variables in Utah's Salt Lake Valley. *Atmos. Envir.*, **94**, 742 – 753, doi:http://dx.doi.org/10.1016/j.atmosenv.2014.06.012.

Whiteman, C. D., S. Zhong, W. J. Shaw, J. M. Hubbe, X. Bian, and J. Mittelstadt, 2001: Cold pools in the Columbia Basin. *Wea. Forecasting*, **16**, 432–447, doi:10.1175/1520-0434(2001)016<0432:CPITCB>2.0.CO;2.

Whiteman, C. D., and Coauthors, 2008: METCRAX 2006: Meteorological experiments in Arizona's Meteor Crater. *Bull. Amer. Meteor. Soc.*, **89**, 1665–1680.

Wilczak, J., and Coauthors, 2014: The wind forecast improvement project (wfip): A public–private partnership addressing wind energy forecast needs. *Bull. Amer. Meteor. Soc.*, **96**, 1699–1718, doi:10.1175/BAMS-D-14-00107.1.

Wolyn, P. G., and T. B. McKee, 1989: Deep stable layers in the intermountain western United States. *Mon. Wea. Rev.*, **117**, 461–472, doi:10.1175/1520-0493(1989)117<0461:DSLITI>2.0.CO;2.

Ye, Z. J., M. Segal, J. R. Garratt, and R. A. Pielke, 1989: On the impact of cloudiness on the characteristics of nocturnal downslope flows. *Bound.-Layer Meteor.*, **49**, 23–51, doi:10.1007/BF00116404.

Zängl, G., and S. G. Chico, 2006: The thermal circulation of a grand plateau: Sensitivity to the height, width, and shape of the plateau. *Mon. Wea. Rev.*, **134**, 2581–2600, doi:10.1175/MWR3207.1.

Zardi, D., and C. D. Whiteman, (Eds.), 2013: *Mountain Weather Research and Forecasting*, chap. Diurnal Mountain Wind Systems. Springer.

Zhang, H., Z. Pu, and X. Zhang, 2013: Examination of errors in near-surface temperature and wind from wrf numerical simulations in regions of complex terrain. *Wea. Forecasting*, **28**, 893–914, doi:10.1175/WAF-D-12-00109.1.

Zhong, S., and J. Fast, 2003: An evaluation of the MM5, RAMS, and meso-eta models at subkilometer resolution using VTMX field campaign data in the Salt Lake Valley. *Mon. Wea. Rev.*, **131**, 1301–1322, doi:10.1175/1520-0493(2003)131<1301:AEOTMR>2.0.CO;2.

Zhong, S., and C. D. Whiteman, 2008: Downslope flows on a low-angle slope and their interactions with valley inversions. Part II: Numerical modeling. *J. Appl. Meteor. Climatol.*, **47**, 2039–2057, doi:10.1175/2007JAMC1670.1.

Zhong, S., C. D. Whiteman, and X. Bian, 2004: Diurnal evolution of three-dimensional wind and temperature structure in California's Central Valley. *J. Appl. Meteor*, **43**, 1679–1699, doi:10.1175/JAM2154.1.

CHAPTER 2

MULTISCALE CHARACTERISTICS OF SURFACE WINDS IN AN
AREA OF COMPLEX TERRAIN IN NORTHWEST UTAH[1]

2.1 Abstract

Climatological features of the surface wind on diurnal and seasonal timescales over
a 17-yr period in an area of complex terrain at Dugway Proving Ground in north-
western Utah are analyzed and potential synoptic-scale, mesoscale, and microscale
forcings on the surface wind are identified. Analysis of the wind climatology at 26
automated weather stations revealed a bimodal wind direction distribution at times
when thermally driven circulations were expected to produce a single primary direc-
tion. The two modes of this distribution are referred to as the northerly and southerly
regimes. The northerly regime is most frequent in May and the southerly regime is
most frequent in August. January, May, and August constitute a "tripole seasonality"
of the wind evolution.

While both regimes occur in all months, the monthly changes in regime frequency
are related to changes in synoptic and mesoscale phenomena including the climato-
logical position of the primary synoptic baroclinic zone in the western United States,
interaction of the large-scale flow with the Sierra Nevada, and thermal low pressure
systems that form in the Intermountain West in summer.

Numerous applications require accurate forecasts of surface winds in complex ter-

---

rain, yet mesoscale models perform relatively poorly in these areas, contributing to poor operational forecast skill. Knowledge of the climatologically persistent wind flows and their potential forcings will enable relevant model deficiencies to be addressed.

2.2 Introduction

Mountainous areas cover 25% of the Earth's land surface and contain 26% of the global population (Meybeck et al. 2001). As a result, phenomena unique to the atmosphere in complex terrain have significant impacts on a large part of the human population. This impact extends beyond relatively rare but potentially damaging events such as down-slope windstorms and extreme precipitation events to the daily wind patterns whose variations are significant for air quality (Jerrett et al. 2005; Coen et al. 2012; Whiteman et al. 2014), wind energy generation (Wilczak et al. 2014), wildfire suppression and prediction (Butler et al. 2006), agriculture (Li et al. 2015), emergency response and military operations (Liu et al. 2008). Accurate forecasts of the surface and near-surface wind in complex terrain are important for these applications. Unfortunately, mesoscale models run at high resolution often fail to produce accurate simulations of the wind field in complex terrain (Hart et al. 2005; Rife et al. 2004) and tend to be worse over complex terrain than elsewhere (Jiménez and Dudhia 2013).

Winds in much of the western United States are heavily influenced by the thermal and dynamic impacts of the complex topography that characterizes the region. The Mountain Terrain Atmospheric Modeling and Observations (MATERHORN) program was conducted at Dugway Proving Ground (DPG) in northwestern Utah for the purpose of testing and improving mesoscale models and, by extension, operational forecasts (Fernando et al. 2015). To achieve this objective a better understanding of how flows on multiple scales interact in complex terrain is necessary.

Wind is a dynamic response to pressure gradients in the atmosphere and are forced

by mechanisms operating on a wide range of spatial and temporal scales. The passage of *synoptic-scale* troughs and ridges constitutes the largest scale of control on surface winds. On a smaller scale, there are numerous thermally induced and dynamically induced *mesoscale* forcings that can modify or even overwhelm the synoptic-scale flow. At the smallest scale, differential heating of small terrain features can induce *microscale* flows that also may dominate those imposed from larger scales.

Synoptic-scale weather in the western United States is controlled by the seasonal migration of the polar jet stream (Lareau and Horel 2012). While spatial variations of the synoptic-scale flow in the horizontal are usually very gradual, the vertical variations are often significant. In areas of complex terrain with large topographic relief, knowledge of these vertical variations is particularly important to assessing the synoptic forcing on the surface flow.

Whiteman and Doran (1993) posit that synoptically forced flows influence the surface flow in complex terrain in three primary ways. The first is through downward transport of momentum to the surface due to turbulent mixing. This mechanism is common when a well-developed convective boundary layer is present and results in minimal directional shear between the surface and upper levels. In situations where there is vertical wind shear, significant variation of the surface wind can occur as momentum from different levels is turbulently transported to the surface by a growing convective boundary layer.

The two other methods are pressure-driven channeling and forced channeling, when a terrain barrier forces the flow out of geostrophic balance through friction and blockage. Pressure-driven channeling occurs when the surface wind next to a terrain barrier aligns with the component of the pressure gradient parallel to the barrier. Forced channeling, on the other hand, occurs when the surface wind next to a terrain barrier aligns with the component of the flow parallel to the barrier. Depending on the orientation of the wind relative to the terrain, pressure-driven and forced channeling can either reinforce or oppose one another.

In complex terrain, strong local horizontal gradients in temperature exist near the surface due to differential heating of the land surface. These temperature differences hydrostatically produce pressure gradients, which in turn drive winds (Defant 1949). For meso-β and smaller scales, these flows tend to have a low Rossby number and flow up or down terrain under the influence of the buoyancy force (Zardi and Whiteman 2013). Such flows are referred to as *thermally driven* flows. In locations where these flows are particularly strong or synoptic-scale flows are particularly weak, the thermally driven flows can dominate the surface wind evolution. The largest in scale of these flows, the mountain-plain circulation, is driven by the large contrast in daytime heating and nighttime cooling that occurs over the mountains versus the surrounding free atmosphere (Weissmann et al. 2005).

On a smaller scale, thermally driven valley circulations have been observed during daytime and nighttime in individual valleys (Pinto et al. 2006) including two valleys adjacent to DPG (Stewart et al. 2002; Doran et al. 2002; Ludwig et al. 2004). In some cases, thermally driven nocturnal valley flows can take the form of low-level jets (Banta et al. 2004). thermally driven slope circulations have also been observed on individual slopes (Doran and Horst 1983; Whiteman and Zhong 2008; Lehner et al. 2015), in closed basins (Steinacker et al. 2007) and on elevated plateaus (Bossert 1997).

Thermally driven flows can also occur as a result of large land surface contrasts. Lake breezes are common to the valleys close to the Great Salt Lake and were studied by Zumpfe and Horel (2007). Rife et al. (2002) identified slope and valley flows as well as lake breezes and playa breezes at DPG. The playa breeze is driven by temperature contrasts between the playa and surrounding terrain. The playa surface remains cooler during the day and warmer during the night, primarily due to a higher thermal conductivity of the playa soil and due to a higher surface albedo (Hoch et al. 2014).

This research uses both available long-term data sets and high-resolution datasets collected during MATERHORN to understand the climatological evolution of the

surface wind field at DPG on diurnal and seasonal timescales. This climatology, combined with atmospheric reanalysis data, will allow us to identify potential forcing mechanisms causing the observed diurnal and seasonal changes. A better understanding of the forcings will allow investigators to target particular aspects of the numerical model for verification and improvement efforts.

2.3   Data and Methods

The region of interest for this work, the Intermountain West (IMW), consists largely of semiarid high-elevation basins punctuated by meridionally elongated mountain ranges and includes the western half of Utah and nearly all of Nevada. Relative to much of the IMW, the area controlled by the US Army's Dugway Proving Ground (DPG) has an extensive meteorological observation network which hosted two extensive field campaigns as part of the MATERHORN program.

The specific focus of this work is the northeastern quadrant of the IMW where DPG is located, an area that includes much of northwestern Utah (Fig. 2.1). Since the region under examination includes much of the area covered by Pleistocene Lake Bonneville, we will refer to this area as the Bonneville basin (BB).

Average annual precipitation over the valleys of the BB is 150-200 mm. Occupying the lowest elevations of the BB is a seasonally flooded playa that is largely vegetation-free. This area is minimally confined by terrain and will be referred to in this paper as the playa. Ground cover off the playa generally consists of 0.5-1 m-high grasses and shrubs. Mountain ranges in the BB rise 200-800 m above the surrounding plain. The basin to the east of the playa, in this paper referred to as the east basin, is surrounded by higher terrain that forms a horseshoe-shape. The basin opens to the northwest where it empties onto the playa. All the significant mountain ranges and valleys at DPG are oriented roughly north-south.

Dugway Proving Ground maintains 32 Surface Automated Meteorological Stations (SAMS) that are mostly situated on the basin floors. We will only use the 26 stations
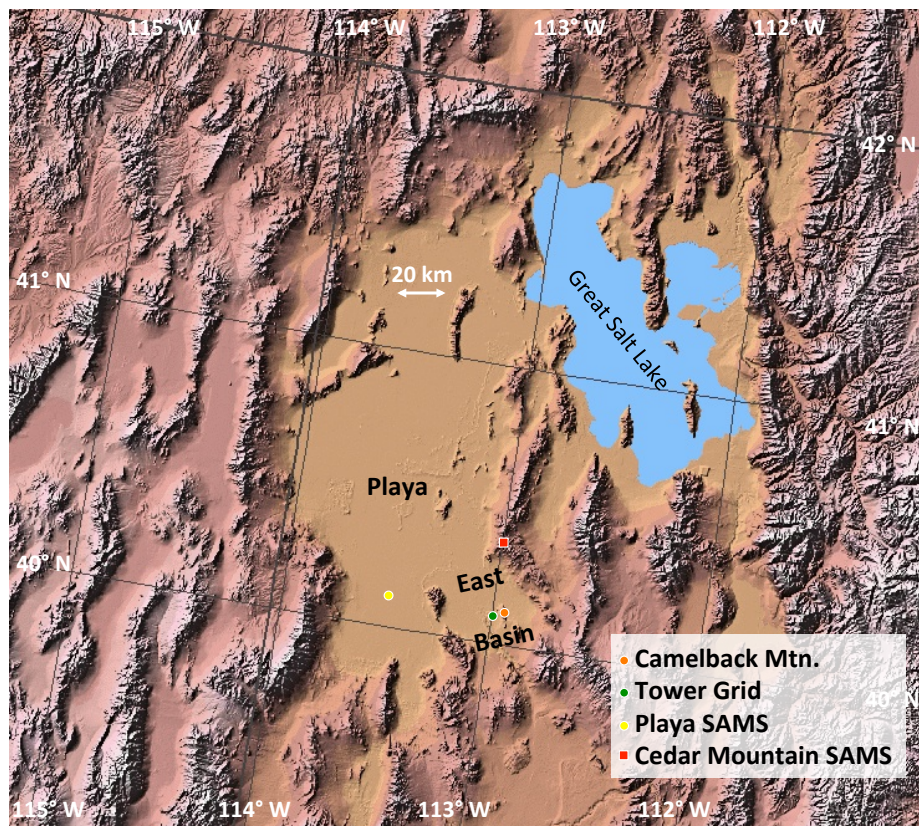
Fig. 2.1. Terrain of the Bonneville basin. The location of selected automatic weather stations (circles), and terrain features are annotated. The Bonneville basin is roughly outlined by tan colors.

with the longest periods of record. Several stations are installed on the playa and two are installed on topographic highpoints. Variables measured at these stations include 2-m temperature, 2- and 10-m wind speed and direction, atmospheric pressure, 2-m humidity, and incoming solar radiation. Our wind analysis will be limited to the 10-m wind field. All data are reported as 5-min or 15-min averages. The SAMS chosen for this analysis have long periods of record (between 7 and 17 yrs) while 6 SAMS with shorter periods of record were excluded from our analysis. Only 3% of the SAMS data is missing due to instrument or data communication failure. 15% is missing for the station with the poorest data coverage.

Quality control of the SAMS observations consisted of plausible value and time-consistency checks. To reduce systematic errors in the dataset, all SAMS sensors are

calibrated once per year.

All available data were averaged to 15-min means. 10-m wind speed and direction were calculated as vector means before being converted to polar coordinates. Monthly climatological averages and statistics were then calculated using all available data for each station. Monthly mean diurnal cycles derived from the dataset permit the analysis of climatologically persistent flows that occur on both the seasonal and diurnal time scales.

Three representative SAMS will be referred to intensively in this work to describe the conditions observed at DPG. The first station, Tower Grid SAMS, is located at 1325 m MSL on the floor of the east basin. The second station, Camelback Mountain SAMS (1547 m MSL) sits atop Camels Back Ridge, a steep and narrow isolated ridgeline protruding up to 225 m from the floor of east basin. Camelback Mountain SAMS provides information on the flow field above the basin surface. The third station, Playa SAMS, is located at 1294 m MSL on the playa, 15 km west of the closest large topographic feature. The locations of these three representative SAMS are shown in Fig. 2.1.

To characterize dynamic and thermodynamic patterns imposed upon the DPG area at the meso-α scale and larger, European Centre for Medium-Range Weather Forecasts (ECMWF) interim reanalysis (ERA-Interim) global reanalysis data from 1995-2012 are used. The ERA-Interim runs with 60 vertical levels and a reduced Gaussian grid with 79-km spacing for surface and other gridpoint fields (Dee et al. 2011). The ERA-Interim was chosen due to its improved representation of the atmosphere over the IMW (Jeglum et al. 2010) relative to the NCEP/NCAR reanalysis and the North American Regional Reanalysis (NARR). We used 850 mb and 700 mb (1 mb = 1 hPa) levels to analyze above-surface flows as they were the most effective for characterizing the synoptic-to-mesoscale environment in an elevated area such as the IMW (Stewart et al. 2002; Steenburgh 2003; Ludwig et al. 2004; Jeglum et al. 2010).

With its relatively coarse resolution the ERA-Interim does not resolve any individual mountain ranges in the BB (see Fig. 4 in (Jeglum et al. 2010)), instead integrating them into large plateaus. Thus, processes and features on the meso-β scale and smaller, such as slope and small valley circulations, are not resolved. However, the north-south oriented topography of the BB and the meso-α and larger flows there are resolved.

2.4 Results

Fig. 2.2 shows surface wind roses for the DPG area for the full period of record (between 7 and 17 years) for all 26 stations. Observations below 1 ms^{-1} have been
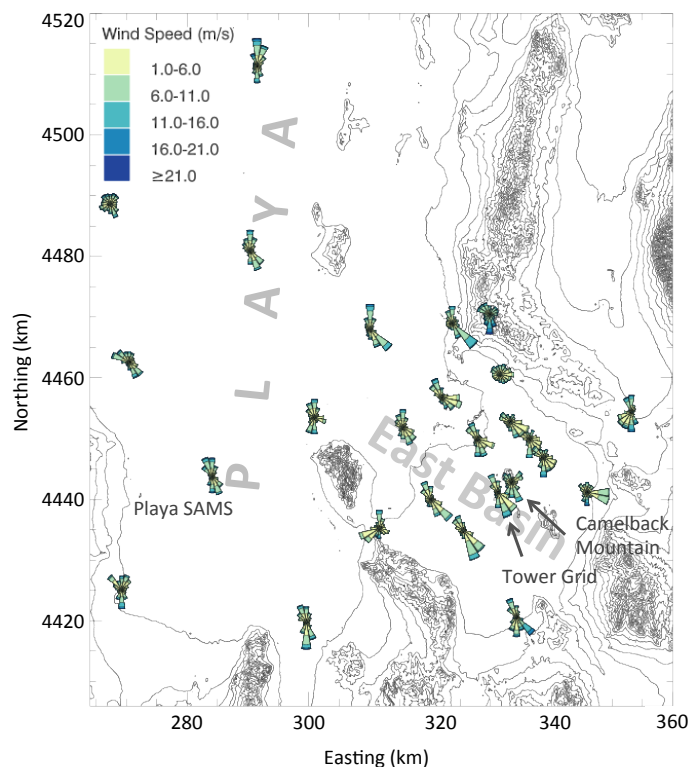

Fig. 2.2. Wind rose map of all DPG SAMS stations. Each station is represented by a wind rose that includes all hourly winds observed over the full period of record for each station (the period 1995-2012 for most stations). The stations are plotted on a UTM grid with 80-m vertical resolution of the terrain contours.

excluded (less than 5% of the data at all stations). Most sites show a pronounced bimodality in the wind direction with winds blowing either from the southern or northern direction. This bimodality could arise from diurnal shifts of the thermally driven valley wind circulation in north-south oriented valleys (Whiteman 2000).

However, the bimodality persists when the data are stratified by hour and month. For instance, at 1600 mountain standard time (MST) in August the wind at most DPG stations is either southerly or northwesterly (Fig. 2.3). If the afternoon flow at DPG was dominated by local thermally driven upvalley flows, there would be a clear single maximum in the upvalley (northerly or northwesterly) direction. We call this bimodality the nondiurnal bimodality and it refers specifically to the surface wind. In order to better understand what causes the nondiurnal bimodality, the data were subjectively divided into three regimes, a northerly regime, a southerly regime, and
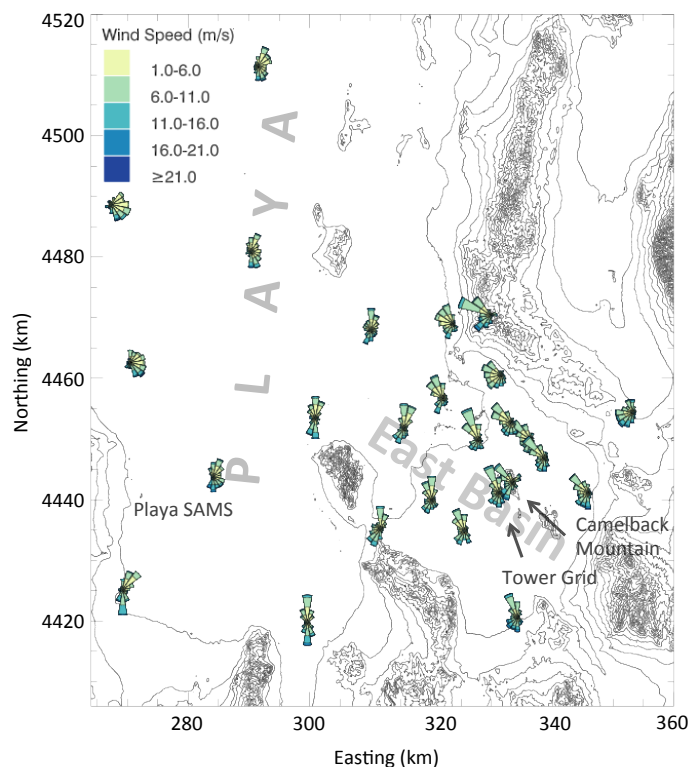

Fig. 2.3. Same as Fig. 2.2 except only winds at 1600 MST in August are included.

a calm regime.

To define these regimes, each 24-h period from 0 UTC to 24 UTC at each station at DPG was designated as being in either the Northerly, Southerly, or Calm Regime based on the direction of the daily mean wind (mean wind for that 24 h period). For each station a given day was considered to be in the northerly regime if the daily mean wind was dominated by a northerly component and the mean wind speed was at least $1\ ms^{-1}$. southerly regime days were designated similarly, by having a dominating southerly component and a mean wind speed of at least $1\ ms^{-1}$. Calm days consisted of the days with a mean wind speed below $1\ ms^{-1}$. Nearly all the DPG surface stations display wind direction distributions that are extremely elongated in the north-south direction, making this method robust. Finally, each day over the 1995-2012 period was designated as being in the Northerly, Southerly or Calm Regime based on the designated regime of the plurality of stations on that particular day. If more than 25 percent of the SAMS-wide data was missing on a given day, the day was excluded from the analysis. Since these regimes are very often coherent across the entirety of DPG, there were only few days that were not clearly in one regime or another.

Fig. 2.4 shows the monthly mean frequencies of the days in the Northerly, Southerly and Calm Regimes for the 1995-2012 period. The difference between Northerly and southerly regimes frequencies is statistically significant at the 0.05 level in the months of January, May, July, August, and December. The northerly regime is most frequent in May and least frequent in August and January. The southerly regime is most frequent in August, and least frequent in May. This produces a tripolar seasonal distribution with poles in May, August and January.

The tripolar seasonal changes in the surface wind field are also apparent in the ERA-Interim mean wind vectors at levels above the surface as shown in Fig. 2.5. Fig. 2.5 displays the monthly mean geostrophic wind at 850 mb and 700 mb and the thermal wind for the intervening layer for the afternoon period. The thermal wind is proportional to the mean horizontal temperature gradient in the 850 mb -700 mb
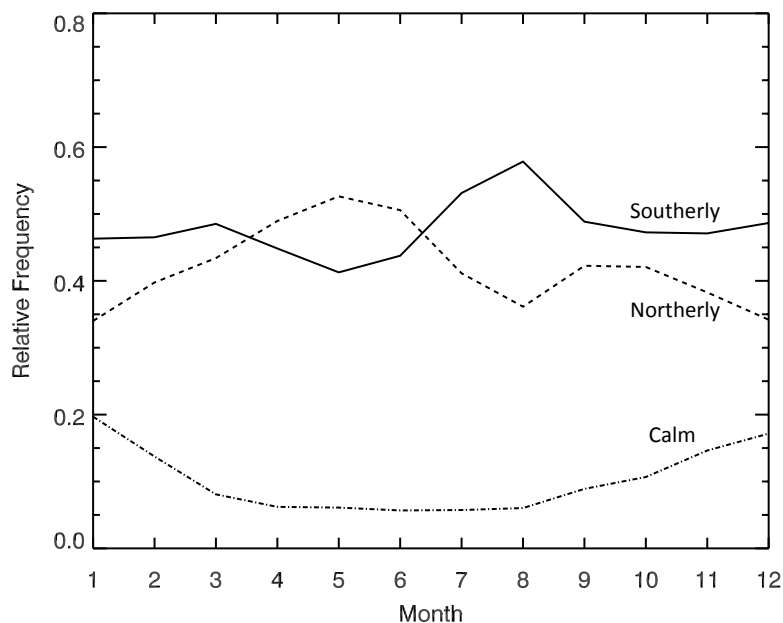
Fig. 2.4. Relative frequencies of the Southerly (solid), Northerly (dash) and Calm (dot-dash) Regimes over the DPG area by month. The sum of the three lines adds up to one for each month. Using Pearson's chi-squared test, the frequency difference between the Northerly and southerly regimes in January, May, July, August, and December are statistically significant at the 0.05 level.

layer and is identical to the magnitude of the geostrophic wind shear vector between 850 mb and 700 mb (Wallace and Hobbs 1977). The tripolar distribution is visible in the seasonal variation of the 850 mb geostrophic wind and the thermal wind. The 700 mb geostrophic wind, in contrast, displays a bipolar pattern, indicating that the primary drivers for the tripolarity are likely below 700 mb.

In May the 850 mb geostrophic wind is primarily easterly and in August it is primarily southwesterly. The 700 mb geostrophic wind, however, is westerly in May and southwesterly in August with a similar magnitude during both months. In May the magnitude of the thermal wind vector is larger than the geostrophic wind at 700 mb. Such a situation requires a reversed pressure gradient at lower levels. January exhibits stronger flow at 700 mb and a moderately strong thermal gradient.

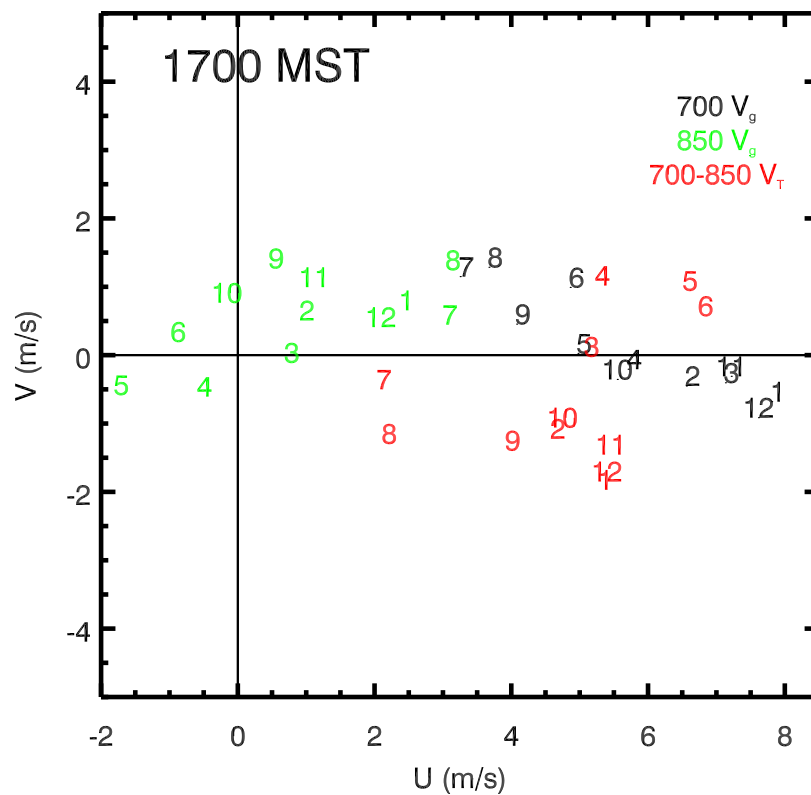The strong non-diurnal bimodality and the tripolar seasonal variation of the sur-

Fig. 2.5. Hodograph plot at 1700 MST of the monthly vector mean 700 mb geostrophic wind (black), 850 mb geostrophic wind (green) and 700-850 mb thermal wind (red) over DPG from the ERA-Interim for 1995-2012. Each number corresponds to the end of a vector starting at the origin representing the mean value for the month indicated by the number.

face wind will be discussed in the following sections through investigating the large scale patterns that characterize the southerly regime in August, the northerly regime in May, and both regimes in January. This will be followed by a discussion of the surface wind flows common to each regime and the forcing mechanisms behind those flows.

2.4.1 Synoptic Patterns of the Three Poles

August is one pole of the tripole distribution because it sees the seasonal maximum in southerly regime conditions. August exemplifies the phenomena that characterize the southerly regime during the warm season, as discussed below.

The synoptic conditions during southerly regime conditions (see Fig. 2.6) are characterized by southwesterly flow at 700 mb, the positioning of the primary mid-latitude baroclinic zone northwest of Utah, and a meridionally-oriented trough at 850 mb. At 850 mb a low is centered over the UT-NV-ID triple point as part of the larger positively tilted trough over the IMW (Fig. 2.6b). Strong southerly flow at 850 mb extends from southern California up to the BB. Additionally, a thermal maximum is visible over eastern Nevada at 700 mb (Fig. 2.6a).

May is the second pole of the tripole and sees the seasonal maximum in northerly regime conditions. While many of the same phenomena that are observed in August are present in May, the relative strength and position of them is sufficiently different such that northerly regime conditions predominate.

In the northerly regime in May, the 700 mb baroclinic zone is now draped across the BB (Fig. 2.6c) and there is no thermal maximum over eastern Nevada. The 850 mb trough axis is now almost zonally oriented, with northwesterly flow at 850 mb (Fig. 2.6d) over the BB. Directional shear in the geostrophic wind between 850 mb and 700 mb is much larger during the northerly regime than the southerly regime.

Evident in the 850 mb wind field in both Fig. 2.6b and 2.6d is a pronounced confluence of the wind in the lee of the Sierra Nevada. This confluence has been
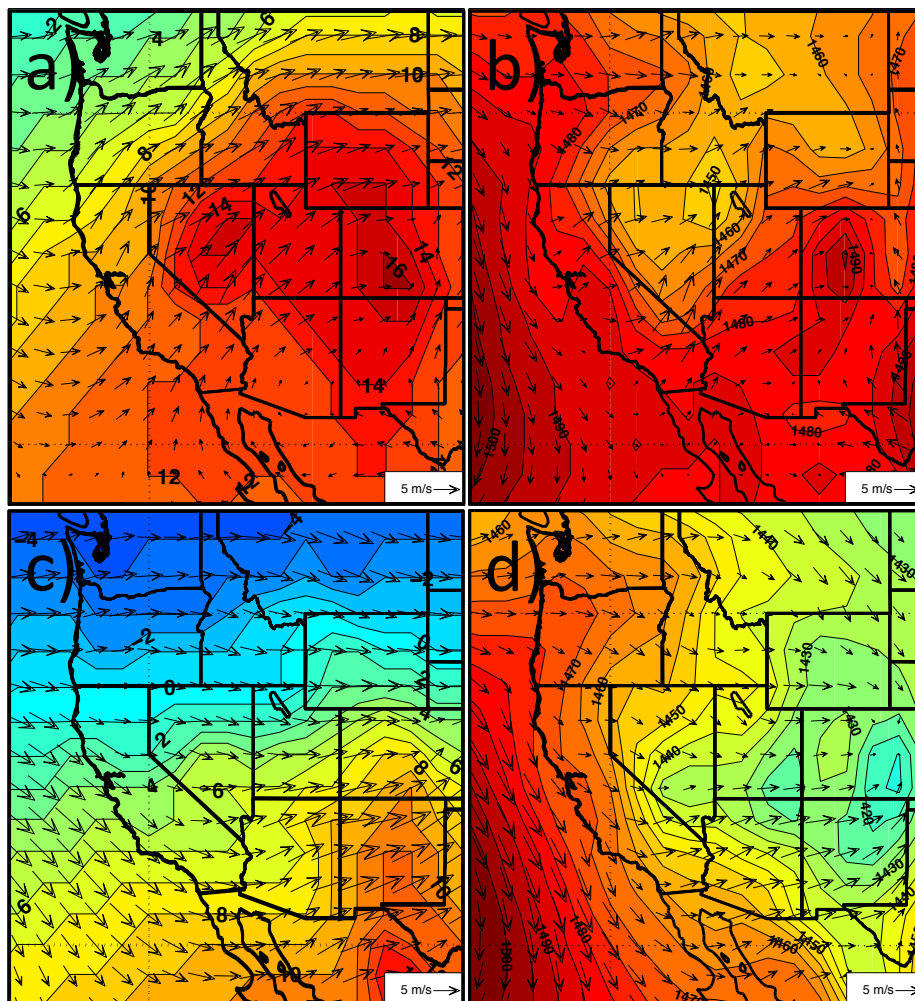
Fig. 2.6. (a) Composite mean 1700 MST 700 mb wind (vectors) and temperature (color contours) for southerly regime days in August taken from the ERA-Interim grid point over DPG for the years 1995-2012. (b) Composite mean 850 mb wind (vectors) and geopotential height (color contours) for southerly regime days in August taken from the ERA-Interim grid point over DPG for the years 1995-2012. c) Same as a) except for northerly regime days in May. The color scale is the same as in a). d) Same as b) except northerly regime days in May. The color scale is the same as in b).

identified as the Great Basin confluence zone (GBCZ) (West and Steenburgh 2010) and is a semi-permanent airstream boundary that results from the flow near and below 700 mb splitting around the highest terrain of the Sierra Nevada and converging in their lee. Its position influences whether the BB will be dominated by southerly or northerly flow. The GBCZ often crosses DPG as a coherent surface boundary that may mark the abrupt transition from southerly regime to northerly regime conditions. During southerly regime conditions the GBCZ is located north of the BB while in northerly regime conditions it lies over the Utah-Arizona border.

The January synoptic patterns present a strong contrast to May and August. Only 850 mb maps are shown, in Fig. 2.7a for the southerly regime and Fig. 2.7b for the northerly regime. 850 mb winds across the IMW are quite weak compared to those during May and June. During southerly regime conditions in January both the 850 and 700 mb (not shown) geostrophic winds are westerly and the atmosphere is relatively stable throughout the day. Under these conditions pressure-driven channeling in the BB may be responsible for producing the southerly surface winds.
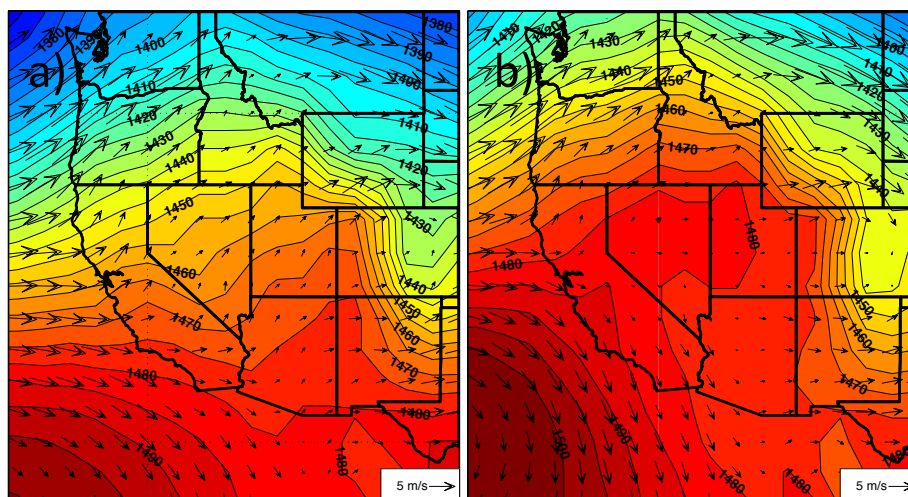

Fig. 2.7. (a) Composite mean 850 mb wind (vectors) and geopotential height (color contours) for southerly regime days in January from the ERA-Interim over the time period 1995-2012. (b) Same as a) except for northerly regime days in January. Color scale is the same for both maps.

The most remarkable feature of the mean January 850 mb geopotential height field under the northerly regime is the lack of a pressure gradient over Utah. The northerly surface flow on these days is due to forced channeling of the climatological northwesterly 700 mb flow.

2.4.2   Surface Station Evolution

The Southerly and northerly regime definitions are based on the dominating daily mean surface wind direction. A more detailed investigation of the diurnal variations of the surface wind direction and wind speed as well as the surface temperature under the different regimes follows. The goal is to highlight the possible forcing mechanisms influencing the surface wind field throughout a full diurnal cycle under both regimes.

The diurnal and seasonal evolution of the surface winds during the Northerly and southerly regimes is illustrated in Fig. 2.8 using composite diurnal hodographs. The three representative locations (Tower Grid, Camelback, and Playa SAMS) are shown for three representative months (January, May and August) that define the tripolar seasonality.

In January (Figs. 2.8a,d,g) the diurnal variations of the surface wind are relatively small at all three stations. The difference between the two regimes is large compared to the diurnal wind variations.

At the Playa SAMS, the diurnal variations of the surface winds in May and August are small compared to the other two sites (Figs. 2.8g-i). Interestingly, the wind field variations at Playa SAMS in August show a meridional variation under southerly regime, and a zonal diurnal variation under northerly regime conditions.

The diurnal variation of the winds at Tower Grid and Camelback in May and August are shown in Figs. 2.8b-c and Figs. 2.8e-f. During both regimes the diurnal patterns follow a preference for westerly flow in the early afternoon and easterly flow in the evening. A preference for southerly flow is observed in the early morning, peaking after sunrise at around 0800 MST. The strength of this early morning
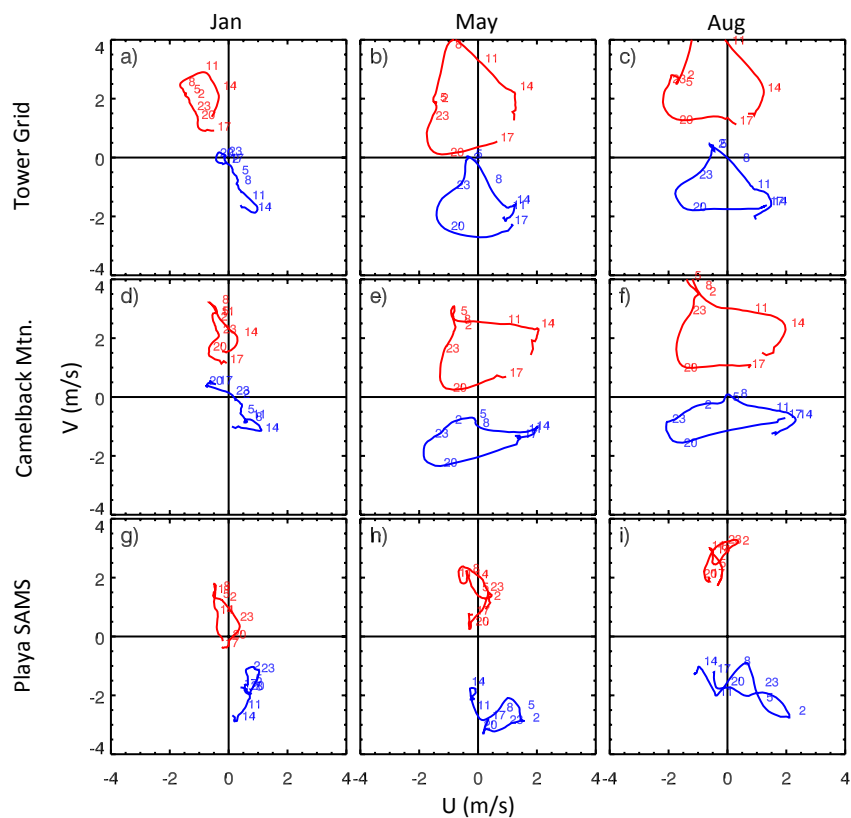
Fig. 2.8. Temporal hodographs illustrating the diurnal wind evolution at three surface meteorological stations during three different months. Each line traces the composite mean wind vector with a time resolution of 15 min. The lines are labeled every 3 hours in MST. Red lines show composite means of southerly regime days at the given station in the given month. Blue lines show composite means of northerly regime days. Each diurnal cycle shown has a sample size of at least 200 days.

southerly component marks the biggest difference between Northerly and southerly regime conditions. The difference between the daily average wind vectors in each regime is comparable with those observed in January.

The variations at Camelback and Tower Grid do not occur on a strictly bimodal diurnal timescale, where the variation is controlled by night or daytime conditions. Instead, the extremes of the diurnal variations occur at approximately 0800 MST, 1500 MST, and 2100 MST. We can separate two modes of variations, one that is roughly east-west oriented and one roughly oriented in the north-south directions. The east-west variations are somewhat enhanced at Camelback, and the north-south variation is larger at the Tower Grid site. The north-south oriented variations could point to an influence of thermal forcing that would lead to a valley circulation in the absence of other forcing mechanisms. However, the large east-west oriented variations point to forcing mechanisms other than local thermally driven circulations.

To examine the regime differences in more detail, Fig. 2.9 compares composite median wind speed, wind direction, and temperature at the Tower Grid and Camelback Mountain SAMS sites during southerly regime days in August. The former station is on the floor of the east basin while the latter sits atop a steep and narrow isolated ridgeline just 4 km horizontally and 220 m vertically away. The station locations are shown in Fig. 2.2. In this analysis we will be using Camelback Mountain as a proxy for the winds in the free-air above Tower Grid. Comparison of the winds at Camelback Mountain with free-air winds observed by a tethered balloon 15 km to the west (comparison not shown) indicate that Camelback Mountain winds are not overly sensitive to local terrain effects.

The composite wind speeds and directions are very similar at both sites during the day. Due to a deep convective boundary layer both stations are aligned with the prevailing southwesterly 700 mb flow and the temperature difference between the two sites follows the dry-adiabatic lapse rate. The surface wind at Tower Grid is not strongly influenced at this time by a thermally driven upvalley wind, as such a wind
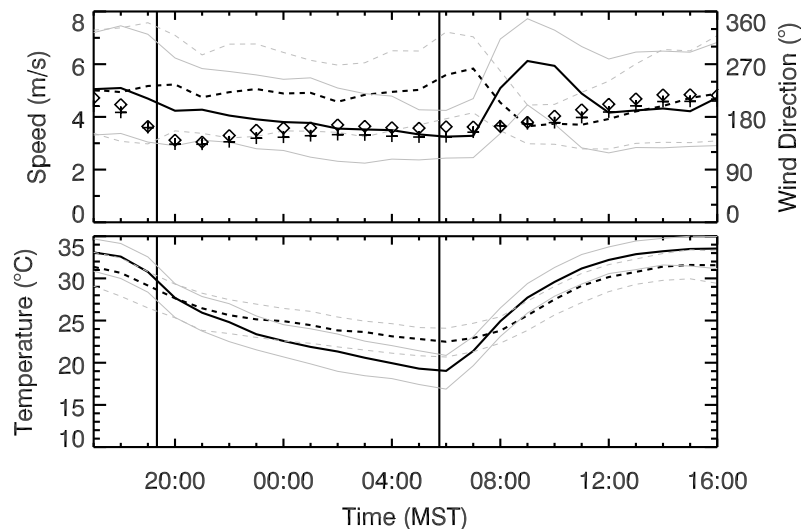
Fig. 2.9. Meteogram showing median daily conditions at Tower Grid (solid black line for wind speed, plus shape for wind direction) and Camelback Mountain (dashed black line for wind speed, diamond shape for wind direction) during the southerly regime in August. Gray lines indicate the interquartile range for each station. Vertical black lines indicate average times of astronomical sunrise and sunset in August.

would be northwesterly.

After sunset the composite temperatures at Tower Grid drop more quickly than at the ridge top (Camelback) due to the development of the basin cold pool. This cold pool strengthens throughout the night. The winds at Tower Grid decrease as the growing stability in the cold pool reduces the momentum exchange with the free atmosphere. Wind speeds at Camelback decrease more slowly than at Tower Grid until 0200 MST, after which they begin to increase, reaching their diurnal maximum shortly after sunrise.

Shortly after sunrise the composite temperature at Tower Grid increases quickly, indicating the development of a convective boundary layer that destroys the nocturnal stable layer. This development coincides with a wind speed increase at Tower Grid while wind speeds at Camelback Mountain decrease, suggesting an enhanced turbu-

lent momentum exchange between the surface and the layers above as the convective boundary layer grows. The flow at Tower Grid remains stronger than at Camelback Mountain through 1200 MST. Wind speeds during the morning transition at Tower Grid are the highest of the diurnal period.

The composite median diurnal evolution of winds and temperatures during northerly regime days in August at the two selected stations are shown in Fig. 2.10. A comparison with Fig. 2.9 illustrates the differences between the two regimes. On average, temperatures during the northerly regime are lower, mainly due to much lower nighttime temperatures. The stronger nighttime valley cold-pools further reflect in lower surface winds and a larger diurnal temperature cycle.

Under northerly regime conditions in August the composite afternoon surface winds and temperatures are similar at both stations due to the deep convective boundary layer present at that time. The mean afternoon wind direction differs by $90\,^\circ$ between the Northerly and southerly regimes, reflecting the $70\,^\circ$ mean 700 mb wind direction difference between them.

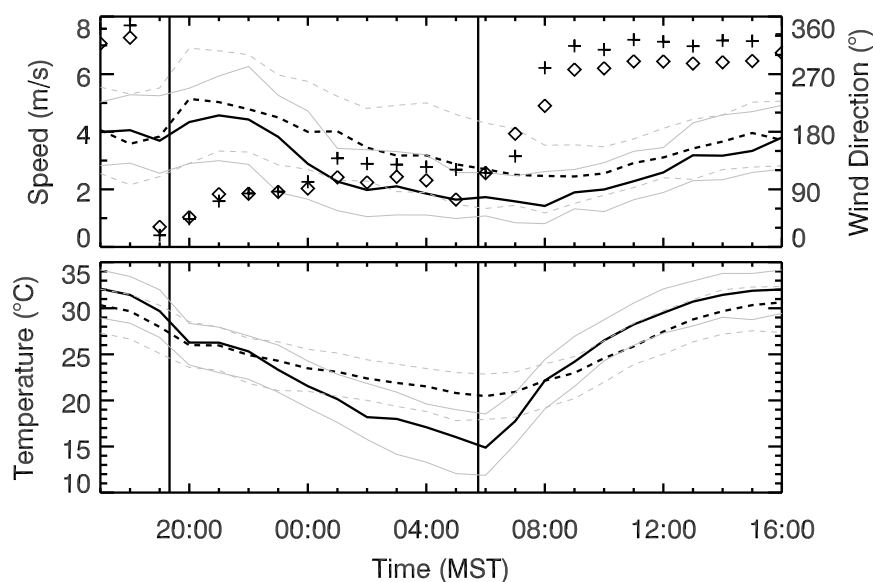Composite winds show an increase near sunset (roughly 1920 MST) under the

Fig. 2.10. Same as Fig. 2.9 except for northerly regime.

northerly regime, especially at the Camelback ridge top site. The wind speed increase coincides with a directional shift from NW to NE and a reduced vertical momentum exchange due to the collapse of the daytime convective boundary layer (CBL). The relatively stronger composite north-northeasterly to easterly surface flow observed at both Tower Grid and Camelback persists from 1900 MST through roughly 2300 MST. A similar shift of the Tower Grid surface flow towards the easterly direction is observed during the southerly regime (see Fig. 2.8c), although it is superimposed on a preexisting southerly instead of a northerly flow.

The composite northeasterly flow weakens after 2200 MST. With the weakening flow and resulting reduced mixing the surface wind at Tower Grid decouples from the atmosphere above and temperatures and wind speeds drop. Further, the wind direction at Tower Grid switches from the mesoscale flow direction of roughly $70\,^\circ$ to the local down-valley flow direction of approximately $145\,^\circ$. DPG SAMS south and east of Tower Grid observe the strongest down-valley flows (not shown). Stations to the north and west of Tower Grid are both further removed from the terrain and on a flatter part of the east basin floor and therefore experience a very weak or non-existent down-valley flow (not shown). Camelback Mountain, elevated above the basin floor, remains above the downvalley flow layer and in easterly flow.

Under the northerly regime, the composite nighttime temperatures at Tower Grid fall more rapidly than temperatures at Camelback Mountain. The maximum nighttime temperature difference between the two sites reaches $7\,^\circ$C , almost doubling the $4\,^\circ$C maximum difference seen during the southerly regime.

Composite wind speeds reach their diurnal minimum during the morning transition under northerly regime conditions. Unlike during the southerly regime, both stations see only a slow increase in wind speeds in the northerly regime during the morning transition. However, there is a marked switch from southeasterly nighttime flow at both stations to a northwesterly daytime flow. Wind directions change minimally through the morning transition on southerly regime days.

2.5   Discussion and Conclusions

We demonstrated that two surface wind regimes dominate at DPG, the southerly regime and the northerly regime. The resulting bimodal distribution of wind direction was shown to be poorly related to the diurnal variations of the thermally driven flow directions. In addition to lacking the expected diurnal changes from up-valley to down-valley flows, the absence of wind speed minima around the evening and morning transition times illustrate the importance of other forcing mechanisms. At DPG, wind speed maxima are instead observed during the morning (southerly regime) and evening transition times (northerly regime).

We found that the largest differences between the Northerly and southerly regimes in the temperature and wind field evolution occur during the morning transition, when a median daily maximum in wind speed is observed during the southerly regime. The median daily maximum in wind speed during the northerly regime is actually observed in the evening. The regime differences were illustrated for two representative sites in DPG's east basin (one on the basin floor, the other on top of an isolated 220 m high, steep-sided ridgeline (see Fig. 2.1). The pronounced maximum in wind speed during southerly regime mornings at Tower Grid may be due to the turbulent mix out of a nocturnal southerly mesoscale flow under southerly regime conditions. This mesoscale flow can include periods with a low-level jet structure, as observed with tethered balloons and radiosondes during MATERHORN under southerly regime conditions (not shown). The southerly mesoscale flow likely arises from the strong synoptic-scale 850 mb pressure gradient over Utah during the southerly regime (see Fig. 2.6b).

Under northerly regime conditions, a strong northeasterly flow was observed through-out DPG during the evening transition. This flow is observed over terrain that would induce a southerly or southeasterly thermally driven down-valley flow and despite a mean westerly 700 mb wind. This points to the importance of the 850 mb pressure gradient during the evening transition period, when the decay of the convective boundary layer decouples the near-surface flow from the westerly 700 mb wind field

aloft. The 850 mb pressure gradient is likely the result of strong synoptic-scale and mesoscale thermal gradients over Northern Utah.

We found that the two regimes correspond to distinct synoptic patterns that differ substantially from one another. This illustrates that the different surface wind forcing is a result of variations in the large-scale flow as well as mesoscale processes that modify the large-scale flow, such as thermal low pressure and lee troughing.

The zonally-oriented 850 mb trough that exists under southerly regime conditions (Fig. 2.6b) likely includes contributions from the Nevada thermal low and the dynamic effects of lee troughing. The thermal low is an important feature of the warm season synoptic pattern over the IMW that develops due to strong heating of the arid, elevated surface. According to Tang and Reiter (1984), there are two primary lobes of the thermal low in the IMW: One over southern Nevada and another over northwestern Utah. The former is present from March to September with a broad peak in strength from April to August. The latter is present from June to August and helps to develop southerly flow at low levels over the BB, contributing to the preponderance of southerly regime conditions in July and August. southerly regime days in August display a 700 mb height minimum over Nevada and northwest Utah (not shown) similar to that seen by Tang and Reiter (1984).

Lee troughs in the IMW may contribute to the strengthening of the meridional pressure gradient over the BB under southerly regime conditions. While they are generally considered a spring phenomenon in the IMW (Jeglum et al. 2010), there is evidence to support lee trough occurrence even in July and August.

The primary ingredient for lee troughing is flow impinging upon a large topographic barrier, and the distribution of 700 mb winds during the southerly regime in August (Fig. 2.11a) shows a clear bias toward southwesterly flow crossing the Sierra Nevada during those conditions. When the 700 mb wind is directly out of the southwest, the flow passes over the high terrain of the Sierra Nevada and Eastern Nevada directly upstream of the BB. It is possible that the integrated effect of the basin-and-
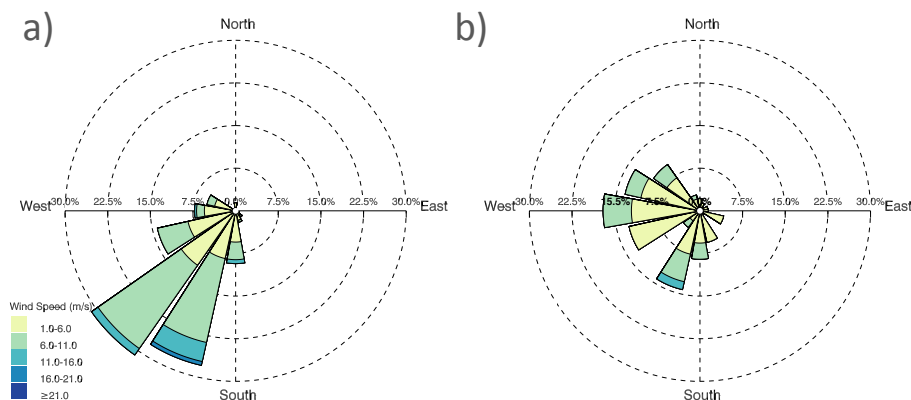
Fig. 2.11. (a) Wind rose showing the distribution of 700 mb winds during the southerly regime in August at the ERA-Interim grid point over DPG. Note dramatic maximum from the southwest. 325 of 558 total August days fall into this category. (b) Wind rose showing the distribution of 700 mb winds during the northerly regime in August. Note dramatic minimum from the southwest. 151 out of 558 total August days fall into this category.

range topography of Eastern Nevada combine to produce a broad plateau that slopes downward toward the northeast into the BB. Under southwesterly flow a lee trough could be generated north and east of this plateau, directly over the BB, as seen in Fig. 2.6b. In this case, the lee trough likely results from a combination of adiabatic descent-induced warming and column stretching.

The mean synoptic pattern under southerly regime conditions bears a strong similarity to that identified by Adams and Comrie (1997) as the prototypical pattern of the North American Monsoon (NAM) with relatively low 850 mb geopotential heights oriented southwest-northeast over Nevada and Utah. 700 mb flow during the southerly regime is southerly or even southeasterly over northern Mexico, New Mexico and Arizona and resembles the typical NAM pattern at this level.

With the trough axis oriented zonally, and relatively strong southwesterly 700 mb flow across Mexico, New Mexico and Arizona, the northerly regime differs from the flow typical of the NAM. It does, however, resemble the prototypical precursor pattern of the West Coast Thermal Trough (WCTT) identified by Brewer et al. (2012). In

this situation the primary IMW baroclinic zone has been pushed southeast over Utah and the GBCZ is southeast of the BB, and there is a positively-tilted trough at 700 mb (not shown). Correspondingly, the southerly regime is similar to the post-WCTT period shown in Brewer et al. (2012) where both the IMW baroclinic zone and GBCZ are north of Utah and the 700 mb trough has moved west and acquired a more negative tilt.

We have identified several likely forcing mechanisms of the surface wind at DPG and discussed their potential contributions to the observed diurnal and seasonal cycles. While persistent ("climatological") flow patterns such as the Northerly and southerly regime can be readily identified when decadal datasets are available, quantifying the contribution of different forcing mechanisms to a given surface wind pattern is exceedingly difficult.

During MATERHORN one objective was to capture the flows at DPG under "synoptically quiescent" conditions when surface flows are purely thermally driven, while other observations targeted moderately to strongly synoptically forced conditions. The strength of the 700 mb flow was used to distinguish between these three forcing categories. However, periods with weak 700 mb flow aloft still displayed surface flows that could not be explained by thermally driven processes alone. The use of other proxies such as mountaintop wind speed thresholds or synoptic-scale pressure gradients from the ERA-Interim were similarly unsuccessful in limiting the observations to purely thermally driven conditions.

Instead of trying to remove certain scales of forcing with simple proxies and *a priori* assumptions, in this research we first searched for the most coherent surface flow regimes at DPG. By analyzing the composite synoptic-scale pattern and the composite surface wind evolution of these regimes we can illustrate the potential forcing mechanisms.

To illustrate the two different approaches, we can compare our findings with those of Rife et al. (2002). In their study, "well-established synoptic-scale anticyclonic

conditions" with clear skies were used as the criteria to define days with dominating thermally driven circulations. As a result, an evening northeasterly flow in the east basin of DPG was attributed to the propagation of the lake breeze from the Great Salt Lake into the east basin, across a distance of 80 km.

The time of the case study presented by Rife et al. (2002) is characteristic for northerly regime conditions (not shown). From our analysis of northerly regime conditions, we learned that northeasterly surface winds are extremely common across all of DPG during the evening hours. These flows frequently persist until 2200 MST or later, extend into areas more than 120 km from the lake, and are also observed at a mountain-top station 800 m above the valley floor (Cedar Mountain SAMS). Our analysis suggests that this flow may be related to the low-level easterly synoptic-scale pressure gradient that exists despite a westerly pressure gradient aloft. This pressure gradient reversal in the vertical is due to the relatively strong baroclinic zone over Utah under northerly regime conditions.

Based on our analysis of northerly regime conditions, we speculate that the thermal contrast between the Great Salt Lake and the elevated terrain to the south likely strengthens the zonal low-level pressure gradient that drives the northeasterly flow. During the day and late afternoon on northerly regime days, the terrain contrast results in a north-south temperature gradient that can magnify the synoptically imposed pressure gradient that encourages northerly or northeasterly flow. At night, the temperature contrast reverses, opposing the synoptically imposed gradient.

When using long-term datasets it is common to combine observations from several months to calculate mean persistent or climatological wind patterns. For example, data collected during June, July and August is averaged to indicate mean summer conditions. The large, high-quality dataset used here to examine the surface wind forcing mechanisms allowed us to identify the climatologically persistent flow patterns on smaller than seasonal (i.e. monthly) timescales. We found a tripolar seasonal evolution of the surface wind fields at DPG, with large changes in the forcing mechanisms

between June and August. Our work thus demonstrates that a traditional seasonal averaging can lead to results that may disguise the forcing mechanisms governing the wind field evolution.

Operational forecasters at DPG are frequently required to produce high-resolution forecasts in both time and space. In many cases this leaves the forecaster dependent on high-resolution mesoscale model forecasts (Liu et al. 2008). However, these forecasts are only available at short lead times due to high computational expense. Being able to identify the large-scale patterns unique to each regime would allow a forecaster to anticipate surface flows characteristic of the southerly regime or northerly regime and lengthen the lead time in anticipation of weather events ideal for DPG operations.

Observations collected during MATERHORN have been (Massey et al. 2014; Serafin et al. 2016; Dimitrova et al. 2015) and will continue to be used to test and improve NWP model parameterizations. We hope to have provided sufficient insight into the variety of forcing mechanisms of the surface wind field at DPG that modelers can better pinpoint model deficiencies and validate their results based on resolved flow patterns instead of being limited to a statistical evaluation. For example, if a particular model run underestimates the speed of the nocturnal southeasterly flow in the east basin, our analysis would tell the investigator that the error could lie in an underestimation of the mesoscale southerly flow, an underprediction of the strength of the thermally driven down-valley flows, or a combination of both.

Due to the multiscalar nature of the forcing mechanisms, deficiencies in numerical model forecasts of surface wind may arise from several sources. An accurate prediction of the placement and strength of boundaries such as the GBCZ is critical for avoiding large errors in surface wind predictions. synoptic-scale features such as the GBCZ and lee troughing require an accurate representation of both the terrain and the large-scale incident flow to be forecast well. The ability of global or mesoscale models to accurately represent the GBCZ is not known, although anecdotal evidence from the MATERHORN field campaigns indicated that forecasts of the GBCZ suffered from

phase and amplitude errors. Mesoscale models are likely sensitive to errors passed from the initial and boundary conditions in these cases (Etherton and Santos 2008). Increased horizontal and vertical resolution of global and mesoscale models should be beneficial for predicting such features (McGinley and Goerss 1986).

The correct forecast of the strength and temporal evolution of mesoscale thermal circulations such as the Nevada low is expected to strongly depend on an accurate representation of sensible heating and therefore of the surface radiation and energy budgets. Massey et al. (2016) showed how poor representation of soil moisture in the IMW in global models has lead to errors in surface temperature forecasts. Addressing model deficiencies affecting surface temperature forecasts over large areas such as these are expected to improve the model representation of mesoscale thermal circulations.

On a smaller scale, an accurate representation of land surface contrasts and of energy exchange processes at the land-atmosphere interface are necessary in NWP models to successfully model the forcing mechanisms of local thermally driven flows. Massey et al. (2014) demonstrated an improvement in surface temperature forecasts over certain soil types at DPG by modifications to the parameterization of soil thermal properties and of soil moisture initial conditions. Future validation and improvements to the land-surface model components are expected to lead to a better representation of surface temperature contrasts and thus the forcing mechanisms of thermally driven flows.

Our analysis has primarily been focused on the area of DPG, but a preliminary look at observations throughout northern Utah revealed a bimodal surface wind pattern very similar to those of the Southerly and northerly regime identified over DPG. Diagnosing the pertinent wind regimes and their forcing mechanisms could be especially useful in the Salt Lake City basin in context of the significant air-quality issues experienced by its 2 million residents (Whiteman et al. 2014).

2.6 References

Adams, D. K. and A. C. Comrie, 1997: The North American Monsoon. *Bull. Amer. Meteor. Soc.*, **78**, 2197–2213, doi:10.1175/1520-0477(1997)078<2197:TNAM>2.0.CO;2.

Banta, R. M., L. S. Darby, J. D. Fast, J. O. Pinto, C. D. Whiteman, W. J. Shaw, and B. W. Orr, 2004: Nocturnal low-level jet in a mountain basin complex. Part 1: Evolution and effects on local flows. *J. Appl. Meteor*, **43**, 1348–1365, doi: 10.1175/JAM2142.1.

Bossert, J. E., 1997: An investigation of flow regimes affecting the Mexico City region. *J. Appl. Meteor*, **36**, 119–140, doi:10.1175/1520-0450(1997)036<0119:AIOFRA>2.0.CO;2.

Brewer, M. C., C. F. Mass, and B. E. Potter, 2012: The West Coast Thermal Trough: Climatology and synoptic evolution. *Mon. Wea. Rev.*, **140**, 3820–3843, doi:10.1175/MWR-D-12-00078.1.

Butler, B., J. Forthofer, M. Finney, L. Bradshaw, and R. Stratton, 2006: High resolution wind direction and speed information for support of fire operations. Tech. Rep. RMRS-P-42CD, U.S. Forest Service Proceedings.

Coen, J. L., M. Cameron, J. Michalakes, E. G. Patton, P. J. Riggan, and K. M. Yedinak, 2012: WRF-fire: Coupled weather–wildland fire modeling with the Weather Research and Forecasting Model. *J. Appl. Meteor. Climatol.*, **52**, 16–38, doi: 10.1175/JAMC-D-12-023.1.

Dee, D. P., et al., 2011: The ERA-Interim reanalysis: configuration and performance of the data assimilation system. *Quart. J. Roy. Meteor. Soc.*, **137**, 553–597, doi: 10.1002/qj.828.

Defant, F., 1949: Zur Theorie der Hangwinde, nebst Bemerkungen zur Theorie der Berg- und Talwinde. *Arch. Meteor. Geophys. Bioclimatol., Ser. A*, **(1)**, 421–450.

Dimitrova, R., Z. Silver, T. Zsedrovits, C. Hocut, L. Leo, S. Di Sabatino, and H. S. Fernando, 2015: Assessment of planetary boundary-layer schemes in the weather research and forecasting mesoscale model using MATERHORN field data. *Bound.-Layer Meteor.*, 1–21, doi:10.1007/s10546-015-0095-8.

Doran, J., J. D. Fast, and J. Horel, 2002: The VTMX 2000 campaign. *Bull. Amer. Meteor. Soc.*, **83**, 537–551.

Doran, J. C. and T. W. Horst, 1983: Observations and models of simple nocturnal slope flows. *J. Atmos. Sci.*, **40**, 708–717, doi:10.1175/1520-0469(1983)040<0708:OAMOSN>2.0.CO;2.

Etherton, B. and P. Santos, 2008: Sensitivity of wrf forecasts for south florida to

initial conditions. *Wea. Forecasting*, **23**, 725–740, doi:10.1175/2007WAF2006115.1.

Fernando, H. J. S., et al., 2015: The MATERHORN - unraveling the intricacies of mountain weather. *Bull. Amer. Meteor. Soc.*, doi:10.1175/BAMS-D-13-00131.1.

Hart, K. A., W. J. Steenburgh, and D. J. Onton, 2005: Model forecast improvements with decreased horizontal grid spacing over finescale intermountain orography during the 2002 Olympic Winter Games. *Wea. Forecasting*, **20**, 558–576, doi:10.1175/WAF865.1.

Hoch, S. W., D. Jensen, J. D. Massey, E. R. Pardyjak, and H. J. S. Fernando, 2014: Surface energy balance observations during materhorn. *16th Conference on Mountain Meteorology, San Diego, CA*, Poster, 18-22 August, 2014.

Jeglum, M. E., W. J. Steenburgh, T. P. Lee, and L. F. Bosart, 2010: Multi-reanalysis climatology of Intermountain Cyclones. *Mon. Wea. Rev.*, **138**, 4035–4053, doi: 10.1175/2010MWR3432.1.

Jerrett, M., et al., 2005: Spatial analysis of air pollution and mortality in Los Angeles. *Epidemiology*, **16**, 727–736.

Jiménez, P. A. and J. Dudhia, 2013: On the ability of the WRF model to reproduce the surface wind direction over complex terrain. *J. Appl. Meteor. Climatol.*, **52**, 1610–1617, doi:10.1175/JAMC-D-12-0266.1.

Lareau, N. P. and J. D. Horel, 2012: The climatology of synoptic-scale ascent over western North America: A perspective on storm tracks. *Mon. Wea. Rev.*, **140**, 1761–1778, doi:10.1175/MWR-D-11-00203.1.

Lehner, M., C. D. Whiteman, S. W. Hoch, D. Jensen, E. R. Pardyjak, L. S. Leo, S. Di Sabatino, and H. J. S. Fernando, 2015: A case study of the nocturnal boundary layer evolution on a slope at the foot of a desert mountain. *J. Appl. Meteor. Climatol.*, **54**, 732–751, doi:10.1175/JAMC-D-14-0223.1.

Li, S., L. Zhang, S. Kang, L. Tong, T. Du, X. Hao, and P. Zhao, 2015: Comparison of several surface resistance models for estimating crop evapotranspiration over the entire growing season in arid regions. *Agric. For. Meteor*, **208**, 1–15, doi: http://dx.doi.org/10.1016/j.agrformet.2015.04.002.

Liu, Y., et al., 2008: The operational mesogamma-scale analysis and forecast system of the U.S. Army Test and Evaluation Command. Part I: Overview of the modeling system, the forecast products, and how the products are used. *J. Appl. Meteor. Climatol.*, **47**, 1077–1092, doi:10.1175/2007JAMC1653.1.

Ludwig, F. L., J. Horel, and C. D. Whiteman, 2004: Using EOF analysis to identify important surface wind patterns in mountain valleys. *J. Appl. Meteor*, **43**, 969–983, doi:10.1175/1520-0450(2004)043<0969:UEATII>2.0.CO;2.

Massey, J. D., W. J. Steenburgh, S. W. Hoch, and J. C. Knievel, 2014: Sensitivity of near-surface temperature forecasts to soil properties over a sparsely vegetated dryland region. *J. Appl. Meteor. Climatol.*, **53**, 1976–1995, doi:10.1175/JAMC-D-13-0362.1.

Massey, J. D., W. J. Steenburgh, J. C. Knievel, and W. Y. Y. Cheng, 2016: Regional soil moisture biases and their influence on wrf model temperature forecasts over the intermountain west. *Wea. Forecasting*, 197–216, doi:10.1175/WAF-D-15-0073.1.

McGinley, J. A. and J. S. Goerss, 1986: Effects of terrain height and blocking initialization on numerical simulation of alpine lee cyclogenesis. *Mon. Wea. Rev.*, **114**, 1578–1590, doi:10.1175/1520-0493(1986)114<1578:EOTHAB>2.0.CO;2.

Meybeck, M., P. Green, and C. Vörösmarty, 2001: A new typology for mountains and other relief classes: An application to global continental water resources and population distribution. *Mount. Res. Develop.*, **21**, 34–45, doi:10.2307/3674130.

Pinto, J. O., D. B. Parsons, W. O. J. Brown, S. Cohn, N. Chamberlain, and B. Morley, 2006: Coevolution of down-valley flow and the nocturnal boundary layer in complex terrain. *J. Appl. Meteor. Climatol.*, **45**, 1429–1449, doi:10.1175/JAM2412.1.

Rife, D. L., C. A. Davis, Y. Liu, and T. T. Warner, 2004: Predictability of low-level winds by mesoscale meteorological models. *Mon. Wea. Rev.*, **132**, 2553–2569, doi:10.1175/MWR2801.1.

Rife, D. L., T. T. Warner, F. Chen, and E. G. Astling, 2002: Mechanisms for diurnal boundary layer circulations in the Great Basin Desert. *Mon. Wea. Rev.*, **130**, 921–938, doi:10.1175/1520-0493(2002)130<0921:MFDBLC>2.0.CO;2.

Serafin, S., S. J. De Wekker, and J. Knievel, 2016: A mesoscale model-based climatography of nocturnal boundary-layer characteristics over the complex terrain of north-western Utah. *Bound.-Layer Meteor.*, 1–25, doi:10.1007/s10546-015-0044-6.

Steenburgh, W. J., 2003: One hundred inches in one hundred hours: Evolution of a wasatch mountain winter storm cycle. *Wea. Forecasting*, **18**, 1018–1036, doi:10.1175/1520-0434(2003)018<1018:OHIIOH>2.0.CO;2.

Steinacker, R., et al., 2007: A sinkhole field experiment in the Eastern Alps. *Bull. Amer. Meteor. Soc.*, **88**, 701–716.

Stewart, J. Q., C. D. Whiteman, W. J. Steenburgh, and X. Bian, 2002: A climatological study of thermally driven wind systems of the U.S. Intermountain West. *Bull. Amer. Meteor. Soc.*, **83**, 699–708, doi:10.1175/1520-0477(2002)083<0699:ACSOTD>2.3.CO;2.

Tang, M. and E. R. Reiter, 1984: Plateau monsoons of the Northern Hemisphere: A comparison between North America and Tibet. *Mon. Wea. Rev.*, **112**, 617–637,

doi:10.1175/1520-0493(1984)112<0617:PMOTNH>2.0.CO;2.

Wallace, J. M. and P. V. Hobbs, 1977: *Atmospheric Science: An Introductory Survey.* Academic Press, London, 467pp.

Weissmann, M., F. J. Braun, L. Gantner, G. J. Mayr, S. Rahm, and O. Reitebuch, 2005: The Alpine mountain–plain circulation: Airborne doppler lidar measurements and numerical simulations. *Mon. Wea. Rev.*, **133**, 3095–3109, doi:10.1175/MWR3012.1.

West, G. L. and W. J. Steenburgh, 2010: Life cycle and mesoscale frontal structure of an Intermountain Cyclone. *Mon. Wea. Rev.*, **138**, 2528–2545, doi:10.1175/2010MWR3274.1.

Whiteman, C. D., 2000: *Mountain Meteorology: Fundamentals and Applications.* Oxford University Press, New York, 355 pp.

Whiteman, C. D. and J. C. Doran, 1993: The relationship between overlying synoptic-scale flows and winds within a valley. *J. Appl. Meteor*, **32**, 1669–1682, doi:10.1175/1520-0450(1993)032<1669:TRBOSS>2.0.CO;2.

Whiteman, C. D., S. W. Hoch, J. D. Horel, and A. Charland, 2014: Relationship between particulate air pollution and meteorological variables in Utah's Salt Lake Valley. *Atmos. Envir.*, **94**, 742 – 753, doi: http://dx.doi.org/10.1016/j.atmosenv.2014.06.012.

Whiteman, C. D. and S. Zhong, 2008: Downslope flows on a low-angle slope and their interactions with valley inversions. Part I: Observations. *J. Appl. Meteor. Climatol.*, **47**, 2023–2038, doi:10.1175/2007JAMC1669.1.

Wilczak, J., et al., 2014: The wind forecast improvement project (wfip): A public–private partnership addressing wind energy forecast needs. *Bull. Amer. Meteor. Soc.*, **96**, 1699–1718, doi:10.1175/BAMS-D-14-00107.1.

Zardi, D. and C. D. Whiteman, (Eds.), 2013: *Mountain Weather Research and Forecasting*, chap. Diurnal Mountain Wind Systems. Springer.

Zumpfe, D. E. and J. D. Horel, 2007: Lake-breeze fronts in the Salt Lake Valley. *J. Appl. Meteor. Climatol.*, **46**, 196–211, doi:10.1175/JAM2449.1.

CHAPTER 3

LARGE TEMPERATURE FLUCTUATIONS DUE TO COLD AIR
POOL DISPLACEMENT ALONG THE LEE SLOPE OF A
DESERT MOUNTAIN[1]

3.1 Abstract

Large temperature fluctuations (LTFs), defined as a drop of the near-surface temperature of at least 3°C in less than 30 min followed by a recovery of at least half the initial drop, are frequently observed at Dugway Proving Ground in northwest Utah. Time series of temperature at over 100 surface stations were examined in an automated fashion to identify and characterize LTFs. LTFs are most common at night and at locations elevated 50-100 m above the basin floors including on the east slope of an isolated peak named Granite Mountain (GM). The temperature fall associated with an LTF can be as large as 13°C and is typically greatest at heights of 4-10 m AGL. Westerly flows often precede LTFs, whereas northerly winds accompany the temperature drop.

Observational analysis and numerical simulations demonstrate that the dominant causal mechanism of LTFs is the displacement of a valley cold-air pool (CAP) due to an orographic wake. This wake forms preferentially over the east side of GM when stratified southwesterly nocturnal flow impinges on GM and is blocked at low levels.

Warm crest-level air then descends in the lee of the barrier, along with the periodic development of a vertical-axis eddy. These processes enhance the temperature gradient in the lee of the mountain and cause displacement of the CAP edge, which produces the LTF. This mechanism explains the low frequency of LTFs on the west slope of GM as well as the preference for LTFs to occur at higher elevations later at night, as the CAP depth increases.

3.2 Introduction

Fluctuations of near-surface temperature are a common feature of the stable nocturnal boundary layer. In this study we will define a large temperature fluctuation (LTF) as a drop of at least 3°C in less than 30 min followed by a recovery of at least half the initial temperature drop within one hour of the temperature minimum. LTFs can indicate substantial modification of the horizontal and vertical structure of the stable boundary layer.

The potential mechanisms that could produce LTFs can be split into two primary groups. The first group involves significant horizontal advection of cold air and includes synoptic fronts (Shafer and Steenburgh 2008), convective outflows (Mueller and Carbone 1987; Johnson et al. 2014) and slope and valley flow fronts (Doran and Horst 1981; Blumen et al. 1999). The second group involves the displacement of a cold-air pool (CAP)(Whiteman et al. 2001) such that cold air ascends and descends the slopes confining the CAP, producing LTFs in the area that the CAP periodically envelops.

CAPs can form via in-situ cooling, advection of cold air into basins and valleys by katabatic flows (Neff and King 1989; De Wekker and Whiteman 2006), or by warm air advection above the basin (Wolyn and McKee 1989). The depth of a mature CAP can vary widely, from less than 100 m to nearly 1000 m (Clements et al. 2003; Lareau et al. 2013). While cold-air pools typically will deepen and strengthen through the nocturnal period, variability occurs due to synoptic and mesoscale influences

(Steinacker et al. 2007).

Numerous mechanisms for CAP displacement have been advanced in the literature. The strong stratification observed in CAPs permits the development of wave motions such as internal gravity waves and Kelvin-Helmholtz instabilities that can produce temperature and wind variations at the surface (Cheung and Little 1990). These wave motions can be induced by flow collisions (Lin et al. 1993), convection (Stull 1976), or by the interaction of flow with terrain (Brown et al. 2003; Epifanio 2003).

When a stably stratified flow encounters a terrain barrier, four distinct 3-dimensional flow structures can develop (Epifanio 2003): (1) small-amplitude waves; (2) wave breaking; (3) upstream stagnation and flow-splitting; and (4) lee vortices. Two parameters, ϵ and β can be used to determine, for a given flow and barrier, which class of motions will be observed. The first parameter, ϵ, is the nondimensional mountain height

$$\epsilon = \frac{Nh_0}{U} \tag{3.1}$$

where N is the Brunt-Väisälä frequency, a measure of the static stability of the flow impinging on the barrier, U is the upstream wind speed, and h_0 is the terrain height. The second parameter, β, expresses the horizontal aspect ratio of the barrier with large β indicating mountains elongated in the cross-flow direction.

For large β and $\epsilon \ll 1$, small-amplitude waves or wave breaking are the likely flow structures that will develop. However, the stability and flow structure is not conducive to creating large thermal gradients near the surface. A strong preexisting CAP that can be disturbed would be necessary for LTFs to occur (Lee et al. 1989; Lareau and Horel 2014).

Situations with values of $\epsilon \gg 1$ are likely to result in blocked flow at low levels which can induce flow splitting or an orographic wake in the lee of the barrier. Orographic wakes are potentially conducive to LTF development. During an orographic wake, potentially warmer air descending in the lee of terrain and relatively cold, stable air flowing around the terrain can produce a stationary boundary that resembles a density current in the lee of the barrier (Epifanio and Rotunno 2005). If the position of this boundary fluctuates, LTFs may be produced at the surface.

Due to their small spatial scale and short temporal duration, LTFs present a challenge for numerical models. Models may not resolve the phenomena that contribute to LTFs or may have difficulty parameterizing those phenomena. Strong CAPs, an important component of LTFs, are particularly difficult to simulate, and often display excessive vertical mixing (Holtslag et al. 2013; Neemann et al. 2015). Simulations of mountain waves, a potential LTF causal mechanism, have been shown to be highly sensitive to initial and boundary conditions and model parameterizations (Reinecke and Durran 2009a,b). No previous investigators have specifically attempted to replicate observed LTFs in complex terrain using numerical simulations.

The Mountain Terrain Atmospheric Modeling and Observations (MATERHORN) program has the primary goal of addressing deficiencies in our understanding of boundary layer processes in complex terrain and deficiencies in the representation of such processes in mesoscale models (Fernando et al. 2015). LTFs are the surface manifestation of a significant disturbance of the nocturnal SBL, and they were observed in many locations across the MATERHORN study domain in Northern Utah. A thorough understanding of the causal mechanisms of LTFs will be beneficial for understanding boundary layer processes in complex terrain and insight gained will aid the model verification and improvement efforts of the MATERHORN program and others.

To investigate LTFs an automated algorithm is applied to systematically identify LTFs at over 100 automatic weather stations (AWSs). The events identified by the

algorithm will be shown to occur primarily at night on slopes elevated above the main basin and with temperature variations of up to 13°C in less than 30 min. Case study and composite mean analyses of LTFs, combined with high-resolution numerical simulations, will be used to conclude that the primary causal mechanism for the observed LTFs is the displacement of a cold-air pool by an orographic wake that forms in the lee of a topographic barrier when a persistent stably-stratified nocturnal flows impinges on the barrier.

3.3 Location and Instruments

The observational component of the MATERHORN program was conducted at Dugway Proving Ground (DPG) in northwest Utah. DPG was chosen due to its complex terrain, accessibility, and an extensive network of preexisting meteorological sensors. Terrain at DPG is characterized by relatively tall, steep-sided mountain ranges interspersed with wide flat valleys (see Fig. 3.1). The climate in the area is semiarid with a mean annual precipitation of around 200 mm.

The western part of DPG, labeled "Playa" in Fig. 3.1, consists of extremely flat (slopes as low as 0.0001%) and largely vegetation-free mud flats or playas. The basin in the eastern portion of DPG, labeled "east basin", is covered by sparse, low brush and grass with a mean slope of around 0.002%. The land-surface contrast between the two basins causes the east basin to develop a CAP that is stronger than its counterpart over the playa (Rife et al. 2002). Separating these two basins is Granite Mountain (GM), which rises up to 800 m above the basin floors. The upper half of GM has numerous slopes exceeding 100% while the lower slopes consist mainly of alluvial fans whose slopes are much gentler. One particular alluvial fan, on the southeast side of GM (see inset in Fig. 3.1), was the location of intensive observation during the MATERHORN field experiment. Data collected there have been used in multiple previous studies (Lehner et al. 2015; Grachev et al. 2015). This area will be referred to here as the east slope and will be the primary focus for analysis in this
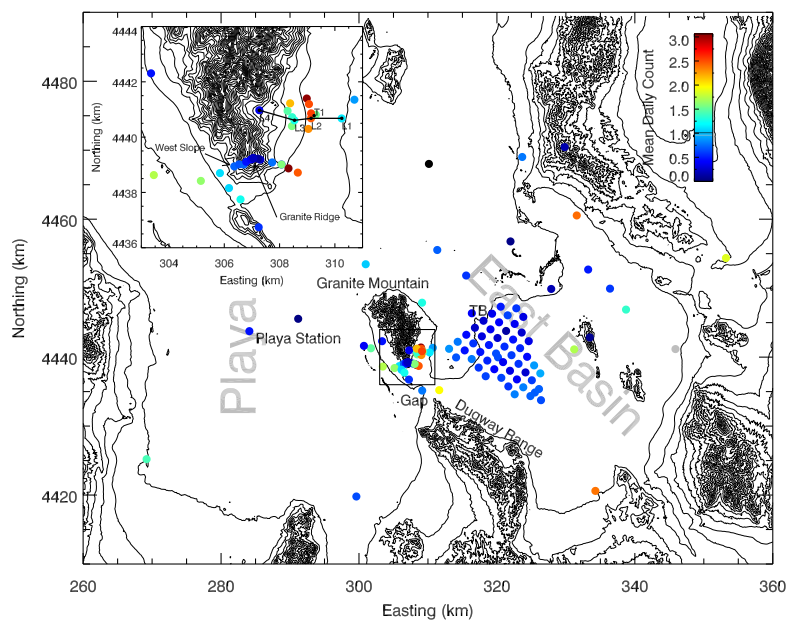
Fig. 3.1. Universal transverse Mercator zone-12T map of the study area at DPG with the southern part of Granite Mountain detailed in the inset. The color-coded circles indicate the daily frequency of LTFs at various sites at DPG. Elevation contours are 80 m in the main plot, 30 m in the inset. The transect in the inset marked L1-L4 is the primary slope transect in this study. The location of the flux tower ES2, and the Granite Ridge and West Slope sites are annotated in the inset.

paper.

An extensive array of surface AWSs was installed across DPG during the MATER-HORN field campaign. This includes 81 permanent and 40 portable stations that are shown as colored circles in Fig. 3.1. 104 of the stations measured 2 m temperature, 2 m wind speed and direction, atmospheric pressure, and 2-m relative humidity. The remaining 17 stations, installed on a transect across the southern end of GM, only measured temperature and relative humidity at approximately 1.5 m AGL. 5-minute averages of all AWS variables will be analyzed. Four AWSs, labeled L1-L4 in Fig. 3.1, will be a focal point for analysis of LTFs on the east slope.

In addition to the AWSs, several 32-m atmospheric flux measurement towers were deployed during the MATERHORN field campaign. In this study we will be using data from one of these towers located near the bottom of the east slope (labeled ES2 in Fig. 3.1). Temperature, wind speed, wind direction, vertical velocity, turbulent kinetic energy, and sensible heat flux are available for 4 levels on ES2: 0.5 m, 4 m, 10 m, and 20 m AGL. All data were quality controlled and averaged to 5 min using the Utah Turbulence in Environmental Studies Processing and Analysis Code (Jensen et al. 2016). The ES2 tower is nearly co-located with the L2 AWS.

The flows in the topographic gap between the southern end of GM and the Dugway Range were observed with a sodar wind profiler. The sodar recorded 10-min average wind speed and direction at 10 m intervals up to 200 m AGL. The wind measured by the sodar at 150 m AGL in the Gap will be used here to characterize the flow impinging on the southern end of GM.

Vertical profiles of temperature were measured by tethered balloon soundings to heights of 400 m AGL. The tethersonde was operated 13 km northeast of the east slope of GM, and is labeled TB in Fig. 3.1.

More detail on the instrumentation used here can be found in the supplemental materials of Fernando et al. (2015).

To supplement the observations, numerical simulations were conducted using the

Weather Research and Forecasting (WRF) model version 3.4.1 (Skamarock et al. 2008). The model configuration included four one-way nested domains, 50 vertical levels (22 levels below 600 m), and a horizontal resolution of 500 m in the innermost domain, which is a 60 km square centered on the east slope of GM. Physical parameterizations include the Lin et al. (1983) microphysical scheme, the RRTM long-wave radiation parameterization (Mlawer et al. 1997), the Dudhia shortwave radiation parameterization (Dudhia 1989), and the Quasi-Normal Scale Elimination (QNSE) planetary boundary layer scheme (Sukoriansky et al. 2005). The model also included the improved land cover and Noah land-surface model as described in Massey et al. (2014). The National Centers for Environmental Prediction Final Operational Model Global Tropospheric Analyses were used for initial and boundary conditions. This configuration, in particular the planetary boundary layer scheme, was identified by Dimitrova et al. (2015) to offer the best representation of flows in the Gap and near the east slope. WRF simulation of one case study night, 1-2 October 2012, will be used in this paper and consists of instantaneous values of modeled variables at 20-min intervals. The simulation was initialized at 1700 MST on 30 September 2012 and was 48 h long. This provided a 28-h lead time before the first observed LTF on the night of 1-2 October 2012.

3.4 LTF Identification Algorithm

An automated algorithm was developed to identify LTFs and was applied to all 121 AWS datasets from 26 September-29 October 2012. This time period corresponds to the MATERHORN Fall intensive field campaign. LTFs were identified using two criteria. First, a temperature drop of at least 3°C must occur within 30 min using data at a resolution of 5 min. This effectively isolates the sporadic LTF occurrences from the regular fluctuations of $1 - 2$°C that are observed at DPG. Second, at least half of the original temperature drop must be recovered within one hour of the minimum temperature. It is relatively rare that temperatures recover to their initial value, as the

LTFs are usually superimposed on a nocturnal cooling trend. This last requirement excludes synoptic frontal passages, which are relatively common in this area during the fall months. Each LTF identified by the algorithm at the 4 AWSs that comprise the L1-L4 transect was verified manually to ensure the quality of the algorithm.

More restrictive thresholds such as a larger temperature drop criterion or a shorter time period criterion lower the number of LTFs identified but do not fundamentally change the structure of the composite LTF. Less restrictive thresholds dramatically increase the number of LTFs identified at all stations. Additionally, the composite LTF becomes much less coherent when the temperature drop requirement is set below 2.5°C, as many small temperature fluctuations that exhibit a substantially different morphology are included in the sample. A 3°C drop within 30 min provides the optimum balance between having a large sample size while preserving the characteristics of the large fluctuations.

3.5   Temporal and Spatial Distribution of LTFs

The spatial distribution of LTF frequency is shown by color coded circles in Fig. 3.1. The colors indicate the mean daily number count of LTFs at each AWS as identified by the automated algorithm. LTFs are rare at the bottom of both the east basin and the playa. Mountaintop locations also observe few LTFs. LTFs are frequent on the slopes slightly above the valley floors, particularly near GM. The inset in the upper left of Fig. 3.1 shows the southern end of GM in more detail. Locations near the bottom of the east slope of GM average up to 3 LTFs per night. This is the highest frequency observed at DPG. The frequency of LTFs decreases dramatically only 50 m altitude higher up the slope, and continues to decrease up to the ridgetop. Sites on the more sparsely instrumented west slope of GM exhibit much lower LTF frequencies than the east slope. Due to the high frequency of LTFs on the east slope of GM and the extensive observational network there, our analysis will focus on this area.

The hourly frequency of LTFs on the east slope of GM is shown in Fig. 3.2. Overall, LTF frequency increases dramatically near sunset (between 1730 and 1820 mountain standard time (MST)), is elevated through the night, then decreases to near zero by 1000 MST.

LTFs are extremely rare between 1000 MST and 1700 MST. The only LTFs observed between 1200-1400 MST are attributable to convective outflows observed at L1 on 25 October 2012. Manual analysis indicated that these were the only convective outflows identified as LTFs by the automated algorithm at L1-L4. LTF frequency at L1 (bottom of the slope) quickly reaches its peak at 2200 MST, after which it decreases through 1000 MST. At L2, 35 m higher on the slope, the highest LTF frequencies are observed. A broad plateau in frequency is observed here between 2200 MST and 0500 MST. At L3, 23 m higher than L2, the overall frequency is again lower, although a steady increase is seen to a pronounced maximum at 0500 MST. At L4, 74 m higher than L3, a similar pattern to L3 is shown, but a lower maximum is observed.

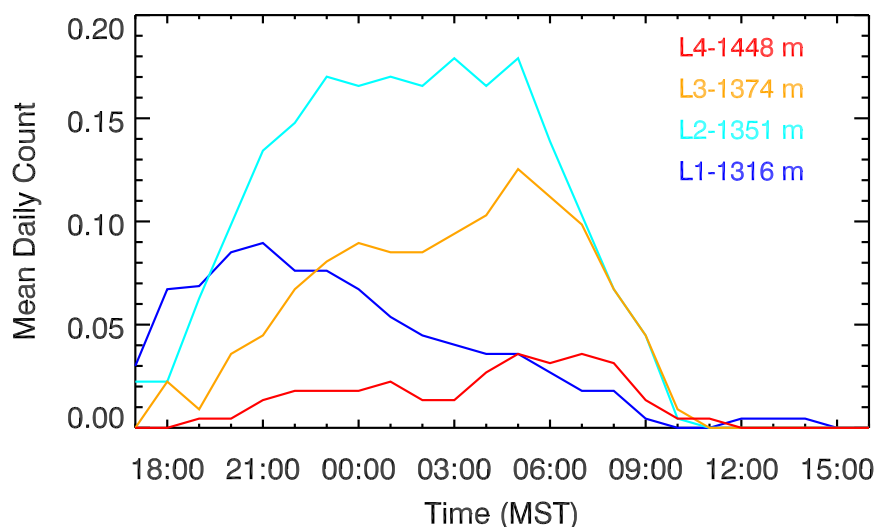While the hourly frequencies of LTFs at L1-L4 differ, LTFs at the 4 levels tend to

Fig. 3.2. Mean daily count of LTFs in an individual hour over the 34-day observation period on the east slope at L1 (dark blue), L2 (light blue), L3 (yellow) and L4 (red).

occur on the same days and under the same general atmospheric conditions. Fig. 3.3a shows daily counts of LTFs at L1-L4 for each of the 34-day study period. No LTFs were observed at any level on the slope on 6 of the 34 days. No LTFs were observed at L4 on 23 days, the most in the L1-L4 transect. LTFs tend to be observed at each level of the slope on the same nights. This is particularly true at L2 and L3 where there are only 3 days where LTFs are observed at one but not the other. On nearly all days the largest number of LTFs is observed at L2 and the fewest at L4.

To investigate a possible connection between LTF occurrences and synoptic or mesoscale conditions, ERA-Interim reanalyses and additional observations at DPG were used. LTFs were found to depend most strongly on the stability of the atmospheric layer below the GM ridge and the speed and direction of the wind in the vicinity of GM. To characterize the static stability near GM during LTFs we will use the mean nocturnal lapse rate of two layers on the west side of GM (Fig. 3.3b). Data from the west side of GM is used as it is typically the upstream side during the nocturnal period. Lapse rates are calculated using the Granite Ridge, West Slope, and Playa Station AWSs (locations shown in Fig. 3.1). The lower of the two layers is approximately 100 m thick and its lapse rate (shown in red in Fig. 3.3b) provides an estimate of the CAP strength west of GM. The upper layer (shown in orange in Fig. 3.3b) is 280 m thick and characterizes the stability of the residual layer above the CAP and below the GM ridgeline. The highest numbers of LTFs, particularly at L2 and L3, are observed when the residual layer is at least isothermal and the lapse rate of the CAP exceeds $30°C/km$. Multivariable linear regression indicates that these two lapse rates can explain 86% of the day-to-day LTF variance at L1-L4. The bulk lapse rate determined from temperature readings between Granite Ridge and Playa (shown in blue in Fig. 3.3b) will be later used to characterize the stability upstream of GM.

Mean nocturnal wind speed and direction in the Gap at 150 m AGL is shown in Fig. 3.3c for the 34-day study period. The mean wind speed tends to be less than 4
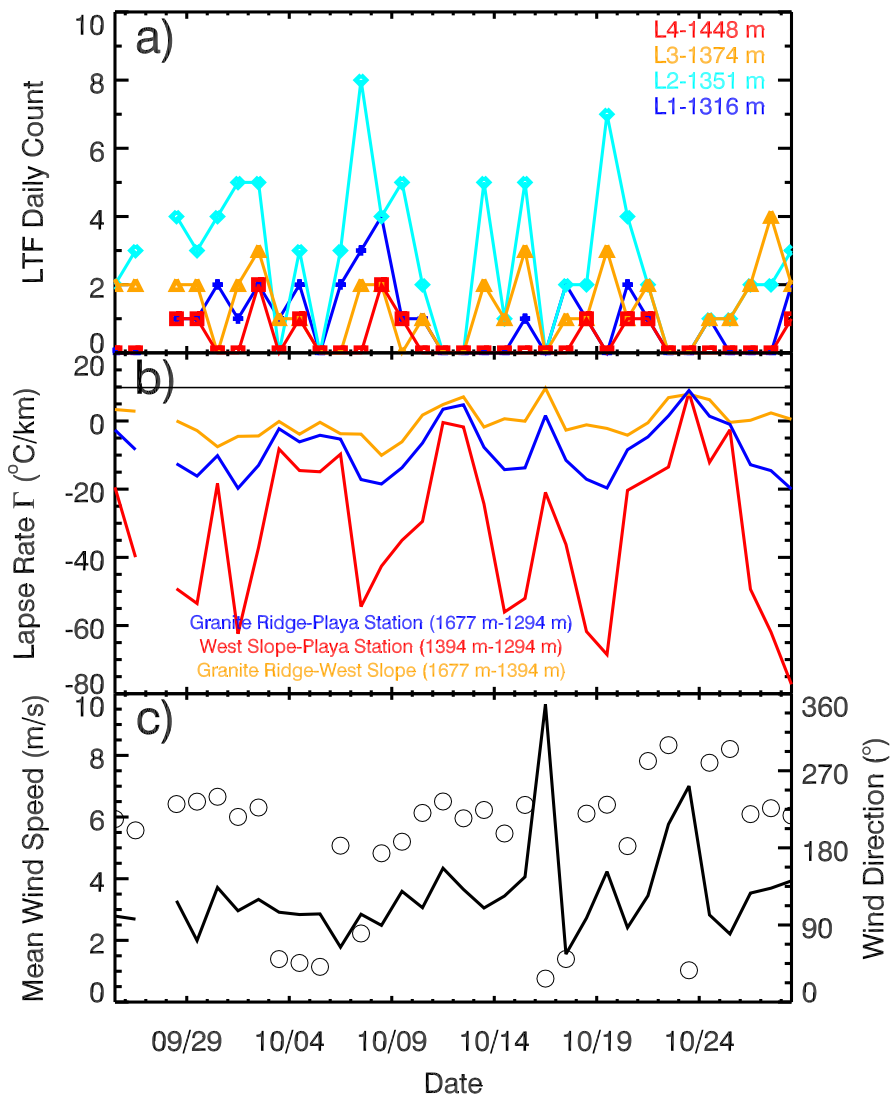
Fig. 3.3. (a) Daily count of LTFs at L1 (blue), L2 (cyan), L3 (orange), and L4 (red) for the 34-day period of record. (b) Mean nocturnal (1900-0500 MST) lapse rate of the residual layer (orange, from Granite Ridge and the West Slope observations), of the CAP (red, from West Slope and Playa Station observations), and of the bulk stability below the GM ridgeline that includes the residual layer and CAP (blue). The horizontal black line indicates a dry adiabatic lapse rate. (c) Mean nocturnal (1900-0500 MST) sodar-derived wind speed (solid line) and wind direction (circles) in the Gap at 150 m AGL.

m/s and the wind direction tends to be southwesterly on nights with a large number of LTFs. An easterly mean nocturnal wind is observed on the night of October 7-8 despite this night displaying the highest number of LTFs. This is due to easterly winds during the first half of the night that switched to westerly after 0100 MST, producing a mean vector that is easterly, despite the LTFs occurring with westerly winds.

The lack of LTFs on 3 nights, 12-13 October, 16-17 October, and 23-24 October, is likely due to light precipitation and extensive cloud cover that limited the development of a nocturnal stable boundary layer. The latter two nights also observed relatively high winds. The other 3 nights without LTFs are among the nights with the weakest static stability during the 34-day period, despite the absence of precipitation and high winds.

Fig. 3.4 illustrates the relationship between the bulk lapse rate (determined from temperature readings at Granite Ridge and Playa Station) and wind direction at 150 m AGL during individual LTF events and shows that LTFs occur most often when the atmosphere is strongly stable and the flow impinging on GM is from the southwest.

Over 80% of observations made during an LTF occur with southwesterly winds impinging on GM and lapse rates more stable than isothermal. LTF observations concurrent with northeasterly flow are often seen at nights when low-level flow reversals (up to 150 m AGL, not shown) in the Gap are observed. These cases often coincide with particularly strong LTFs.

There is a noticeable absence of northeasterly flow in the Gap once the bulk lapse rate drops below $\Gamma = -8°Ckm^{-1}$. The bias toward southwesterly flow in the Gap under increasingly stable conditions (bulk lapse rate is highly negative) offers insight into the mechanism driving the flow in the Gap. During the 34-day study period over a wide range of synoptic scale weather conditions, west or southwesterly flow is the dominant flow over GM and through the Gap from 2200 MST-1300 MST (not shown). The onset of this flow typically occurs 4-5 h after sunset and the cessation of
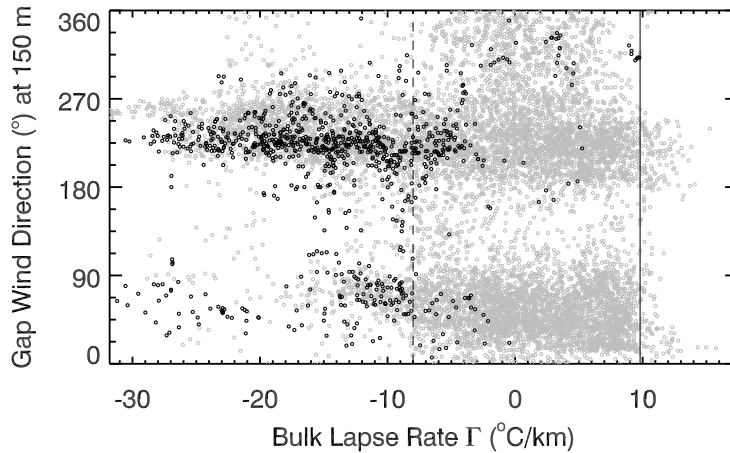
Fig. 3.4. Scatter plot of the bulk lapse rate (based on observations at Playa and Granite Ridge) and sodar-derived wind direction in the Gap at 150 m AGL. All 5-minute observations during the Fall period at L2 (grey) and all observations made during an LTF event at L2 (black) are shown. The vertical solid line marks the dry adiabatic lapse rate and the dashed line marks $\Gamma = -8°C/km$, below which northeasterly flow is very rare.

the flow lags sunrise by a similar amount of time. Local horizontal thermal contrasts due to the playa surface remaining much warmer at night than the east basin (Rife et al. 2002) would be expected to produce an easterly or northeasterly flow in the Gap at night. The observed flow in the Gap is directly opposed to this. The strong bias toward southwesterly flow under higher static stability may indicate that regional scale boundary layer heterogeneity may instead be responsible for the nocturnal flow observed in the Gap.

3.6 Composite Structure of East Slope LTFs

After establishing that LTFs observed on the east slope occur under distinct mesoscale conditions, we composite data from L2 and the adjacent ES2 tower during detected LTFs to identify the key characteristics of the LTFs.

To make this composite, the time of minimum temperature of each LTF will be designated as $t = 0$. Time series for the 60 min preceding and the 40 min following each LTF are normalized by the mean temperature during that period and then averaged. In the case of pressure, the time series is also detrended. Manual subjective analysis of each LTF at ES2 was performed to establish that the composite pattern is representative of the individual cases. Since only 4 of 43 LTFs deviated substantially from the composite evolution, we conclude that the composite mean is representative of the evolution of LTFs in general. Fig. 3.5 shows the composite mean temperature, wind, pressure, nonrotated vertical velocity, and stability evolution during an LTF at Tower ES2. Time $t = 0$ corresponds to the time when the minimum temperature is reached.

Prior to the initiation of the LTF the flow field and temperature structure indicate the presence of a katabatic flow. Fig. 3.5a shows that the wind is out of the west (downslope), with a jet structure with peak speeds at 4 m (Fig. 3.5b) and relatively strong near-surface stratification of $1°Cm^{-1}$. These flow characteristics are indicative of downslope flows (Haiden and Whiteman 2005; Grachev et al. 2015).

At $t = -20$ min the composite LTF begins. The temperature drops sharply at all levels of the tower, the wind speed at all tower levels drops below 0.5 ms^{-1}, and the near-surface stratification begins to weaken. The maximum rate of temperature change occurs at $t = -15$ min. At this time the katabatic jet structure is no longer present and the wind has shifted to northeasterly at all levels with the exception of the 0.5 m level. Vertical velocity at 20 m, which had been slowly increasing for the previous 20 min, reaches a maximum at $t = -15$ min.

The temperature minimum of the composite LTF is reached at $t = 0$. The temperature drops observed at the 4 m and 10 m levels are 40% larger than at 0.5 m or 20 m (Fig. 3.5a), contributing to the near-surface stratification reaching its least stable value at $t = -5$ (Fig. 3.5c). The three lowest levels on the tower display northwesterly winds while the 20 m level retains northeasterly winds (Fig. 3.5b). This directional
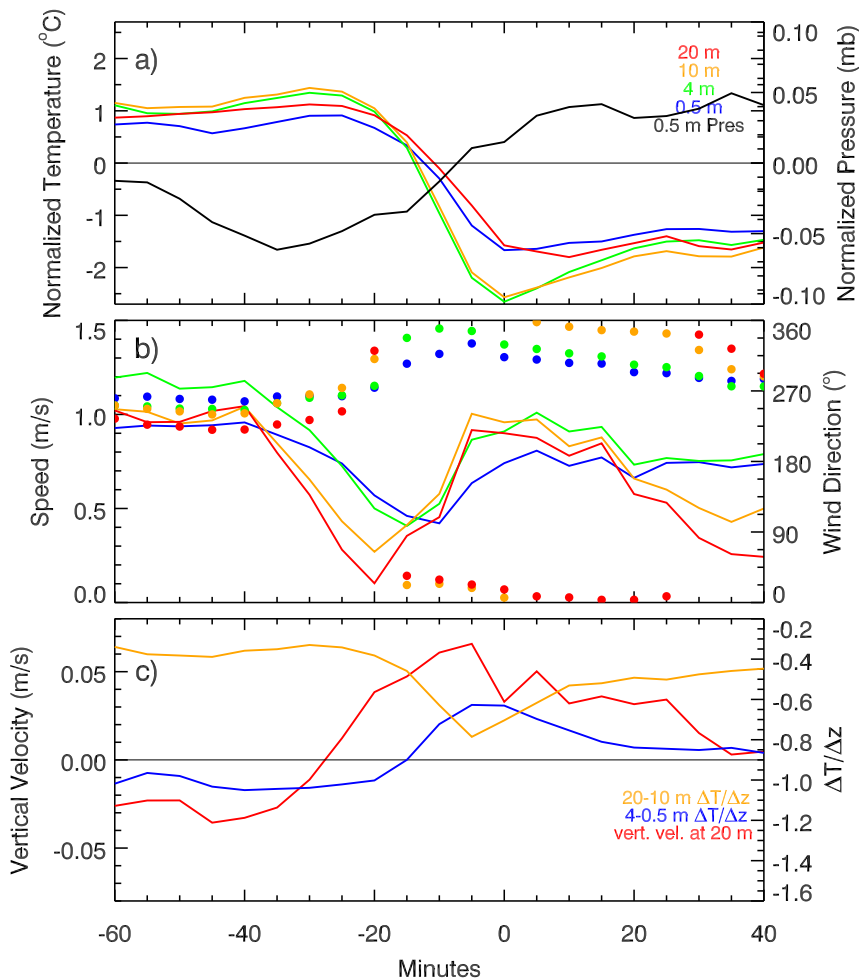
Fig. 3.5. Temporal evolution of the composite LTF at the ES2 tower of (a) normalized temperature and normalized and detrended pressure (black) and (b) wind speed and direction. Colored lines in (a) and (b) correspond to the following tower levels: 0.5 m (blue), 4 m (green), 10 m (orange), and 20 m (red). In (c) vertical velocity is plotted in red and vertical temperature gradient in blue. Sample size for all variables is 43 LTFs.

shear indicates that the katabatic flow has not redeveloped at this point.

The rise in temperature ends by $t = 35$ min and the katabatic flow has reestablished as indicated by the near-surface jet structure, lack of directional shear with westerly winds, and increased near-surface stratification. In the composite LTF, the temperature only recovers 35% of the original drop, instead of the 50% prescribed by the algorithm. This is because the post-LTF temperature recovery often occurs as a sharp increase, after which the temperature continues its nocturnal decrease, rather than remaining elevated. As the exact timing of the temperature recovery varies, the magnitude seen in the composite LTF is smaller than in the individual cases.

The composite LTF pressure trace is shown in Fig. 3.5a. Prior to LTF initiation the pressure decreases. The pressure begins to increase shortly before the temperature fall begins and continues rising until the minimum temperature is reached. However, the amplitude of these fluctuations is less than 0.05 mb. Individual cases display a similar, slowly varying, pressure evolution that does not indicate the presence of solitary waves or transient gravity waves like those in observed Cheung and Little (1990). Potential causes of a pressure signal of this magnitude include hydrostatic effects of the cold air, a pressure signal associated with an orographic wake, or a combination of the two.

Turbulent kinetic energy and sensible heat flux show no consistent pattern in the LTF composites from ES2. Large spikes in turbulent kinetic energy and sensible heat flux often occur in individual LTF cases with the onset or cessation of a LTF, but their timing relative to the occurrence of the LTF minimum temperature are not consistent enough for them to be presented in the composites.

3.7 Case Study of October 1-2 2012

To investigate the causal mechanisms of LTFs, observations from the ES2 tower (Fig. 3.6) and numerous AWSs (Fig. 3.7) will be compared to WRF simulations in a case study for the night of 1-2 October 2012.
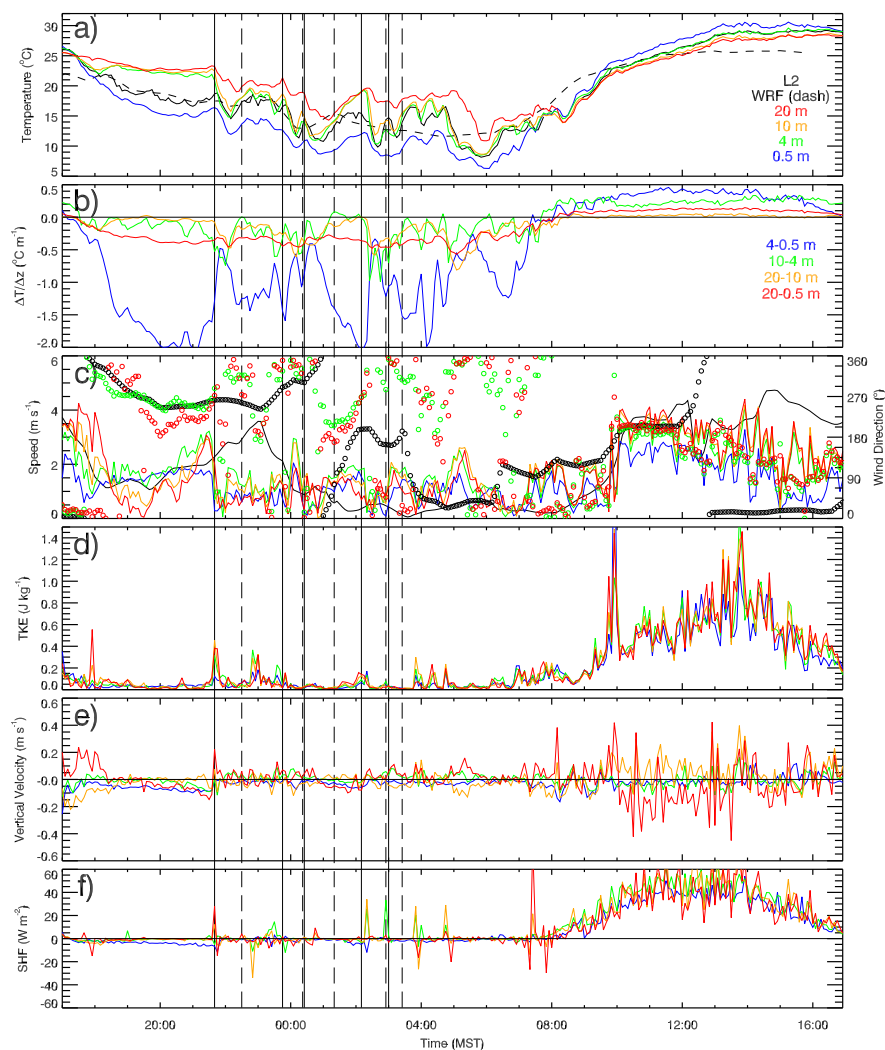
Fig. 3.6. Time series of meteorological variables at ES2, L1 and 2-m data at the WRF grid point closest to ES2 during the night of 1-2 October 2012. (a) Temperature at 2 m at L1 (black), in WRF (black dash), at the 0.5 m level of ES2 (blue), 4 m on ES2 (green), 10 m on ES2 (orange), and 20 m on ES2(red). This color scheme is used similarly in (c)-(f). (b) Temperature difference between specified tower levels. (c) Wind speed (solid line) and wind direction (circles) at ES2 and in WRF. WRF values are at 10 m. (d) Turbulent Kinetic Energy (TKE) at ES2. (e) Vertical velocity at ES2. (f) Sensible heat flux (SHF) at ES2. Vertical black lines denote LTFs as identified by the automated algorithm. The WRF time series has been shifted earlier by 80 min.
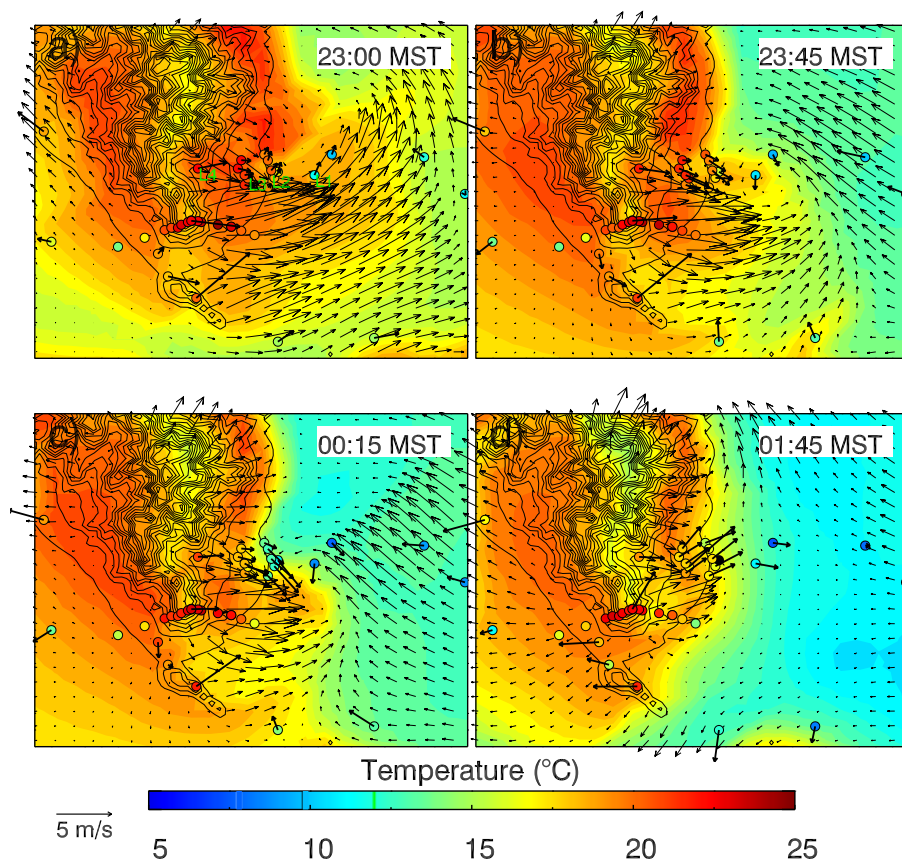
Fig. 3.7. Observations and WRF simulated conditions of an LTF on the east slope of GM during the night of 1-2 October 2012. Color-coded circles represent 2 m temperature and vectors represent 10 m wind speed and direction measured at various AWSs. The L1-L4 AWSs are marked in green in (a). In the case of the transect over GM the color represents the 1.5 m temperature. 2-m temperature from WRF is shown in color contours and WRF 10-m winds with vectors. The WRF data have been shifted earlier by 80 min. The local terrain is shown with a 30 m contour interval. WRF grid points are plotted at 500 m spacing.

This particular night was the second Intensive Observation Period (IOP) of the MATERHORN Fall field campaign.

Five LTFs were observed at L2. The synoptic environment was relatively quiescent as a high-amplitude ridge was centered just to the west of Utah with 700 mb wind speeds less than 6 ms^{-1} throughout the period. The observational data for this night will be described first, followed by a comparison with WRF simulations. Observations from ES2 and L2 will be compared to WRF simulations of 2-m data at the nearest WRF gridpoint (150 m and 130 m southeast of ES2 and L2, respectively, and 16 m below). The WRF simulation reproduced the observed LTFs, but at a later time. For our analysis of the LTF event, we therefore shifted the simulations by 80 min, to synchronize the modeled and observed events. All times shown in the figures and discussed in the text are those corresponding to the observed dataset. With small-scale, discrete phenomena such as LTFs, simulations with temporal or spatial errors can still be quite valuable, such as with simulations of severe convection (Lack et al. 2010).

Fig. 3.6 shows a time series of numerous observed variables at L2 and ES2 along with the WRF simulated values. Local sunset occurs at roughly 1815 MST, after which a katabatic flow develops on the east slope. This flow is marked at ES2 by the onset of weak westerly winds with a jet structure and wind maximum at 4 m. At 2100 MST the flow in the Gap becomes southwesterly (sodar observations, not shown). At this time the katabatic flow structure on the slope disappears and at all levels of the tower the wind speed increases.

Examination of AWSs early in the evening of 1-2 October indicate a growing stable nocturnal boundary layer in the east basin (not shown). Tethered balloon sounding data to illustrate this growth were unfortunately unavailable from 1915-0525 MST on this night. At 1915 the cooling associated with the developing stable boundary layer has just begun. A mature stable boundary layer can be seen in Fig. 3.8 at 0600 MST.

Due to the confinement by terrain this stable boundary layer forms a 150-m deep
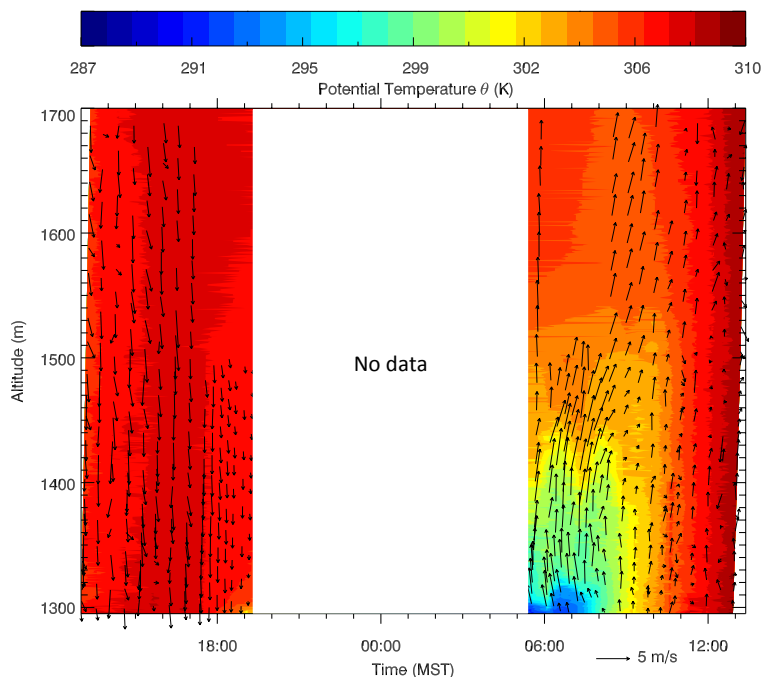
Fig. 3.8. Time-height plot of potential temperature (color contours) and wind (vectors) from a tethered balloon in the east basin during the night of 1-2 October 2012.

CAP that includes a distinct 30-m deep surface-based inversion.

At 2140 MST, with the CAP in place and southwesterly flow over GM, the first LTF occurs. A 7°C temperature drop is observed at the 4 m and 10 m levels of the tower during this LTF. Less pronounced temperature falls are observed at 0.5 and 20 m. As a result, near surface stability decreases dramatically, consistent with the composite LTF structure.

At 2300 MST, 50 min prior to the initiation of the second LTF, L1 is still in the CAP (Fig. 3.7a). The flow through the Gap at 150 m AGL is relatively strong (7 ms^{-1}) from the southwest (not shown) and L2 displays weak southwest winds. At 2320 MST the pre-LTF southwesterly flow is interrupted and the temperature drops briefly. At 2345 MST, the flow at L1 is northerly and a noticeable easterly push can be seen to the east of L1. The temperature drop associated with the second LTF at ES2 begins at 2350 MST. Plan views of the periods immediately before and immediately after the temperature fall of the second LTF are shown in Fig. 3.7b-c.

At 0015 MST the minimum temperature during the second LTF has nearly been reached. Northerly flow predominates at L2 and at areas lower on the slope. Only a moderate temperature drop is observed at L3.

After another brief warm-up, a third LTF begins at 0025 MST. Only after this LTF does the CAP fully retreat from all but the lowest portions of the east slope. The cold air is replaced by relatively warm southwesterly flow which initiates a warming trend that lasts for nearly 90 min (Fig. 3.7d). Additionally, the near-surface stratification strengthens and a katabatic flow structure begins to reappear. The fourth LTF begins at 0210 MST as the CAP envelops ES2 again. After brief warming a fifth marginal LTF occurs at 0305 MST. After this LTF the CAP retreats from ES2. While small temperature fluctuations continue during the rest of the night, none meet the prerequisites for a LTF.

3.7.1 WRF Simulation of 1-2 October 2012

Only one LTF occurred in the WRF simulation, corresponding to a combination of the second and third LTFs in the observations. We will not perform a systematic verification of WRF skill, rather we present a single case to aid in diagnosing the causal mechanism of this LTF and, by extension, LTFs in general.

Fig. 3.9 compares a time series of observations at L2 with data from the WRF grid point closest to L2. At L2, several temperature fluctuations are superimposed upon the general temperature trend that can be represented by a smoothed time series. Averaging the temperature observations to the same 20-min time interval for which WRF data is available produces much better agreement, although this indicates that there are variations in the CAP edge that are not resolved by WRF at 20-min sampling. The biggest wind direction discrepancies between the observations and the WRF simulation are seen between 2300 MST and 0030 MST. Wind speed discrepancies are largest immediately before and after the LTF.

Fig. 3.7a demonstrates that the pre-LTF conditions are well simulated by WRF
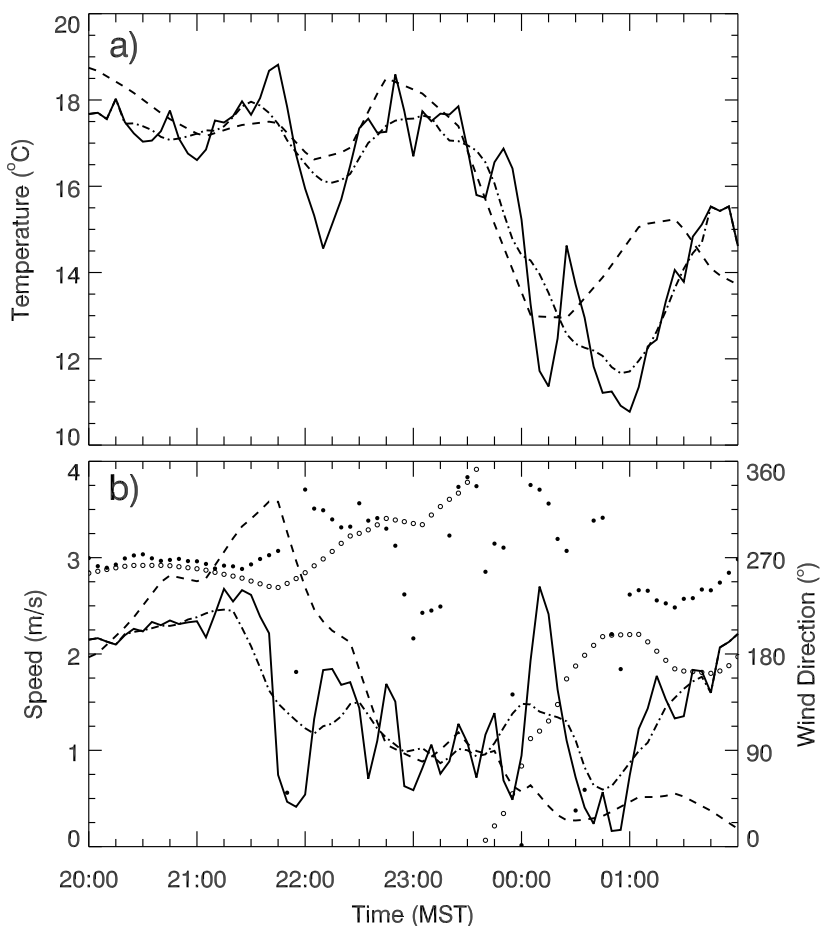
Fig. 3.9. Time series comparison of observations WRF simulations during the LTF shown in Fig. 3.7. (a) Temperature at L2 (solid, temperature at L2 averaged to 20-min (dash-dot) and 2-m from the WRF grid point closest to L2 (dash). (b) 2-m wind speed and direction at L2 (solid line, filled circles), wind speed at L2 averaged to 20-min (dash-dot line) and 10-m wind speed and direction from the WRF grid point closest to L2 (dashed line, open cicles). The time corresponds to the L2 observations. The WRF time series has been shifted earlier by 80 min.

with southwesterly flow through the Gap, westerly flow over the east slope and northeasterly flow over the east basin. However, the lowest portions of both the west slope and east slope are too warm in WRF. At 2345 (Fig. 3.7b), immediately prior to the initiation of the LTF, a vertical-axis eddy is visible in both the observation and WRF, with the CAP moving up the slope in the WRF simulation.

At 0015 (Fig. 3.7c) the CAP has enveloped L1 as the vertical-axis eddy advects cold air across the slope. Agreement between the observations and WRF is reasonable, although strong northeasterly winds are present on the lower slope where WRF has weak northerly or northeasterly winds. Post-LTF conditions (Fig. 3.7d) display westerly winds and warming on the east slope. Also, the low-level flow in the Gap has reversed. This reversal is likely due to the propagation of the vertical axis eddy into the Gap (not shown). WRF resolves this reversal, although the flow in the observations soon returns to southwesterly, while WRF maintains the low-level northeasterly flow in the Gap.

Based on the evidence presented in Fig. 3.7, the LTF is linked to an orographic wake and the associated vertical-axis eddy that forms in the lee of GM. Zonal WRF cross-sections across GM at the latitude of ES2 are shown in Fig. 3.10 and Fig. 3.11 and help in investigating the orographic wake further.

These cross-sections represent the time just before the CAP reaches ES2. Relatively strong flow can be seen descending the east side of GM (Fig. 3.10) with a positive potential temperature anomaly there. The flow on the west side of GM is blocked, with reversed easterly zonal component of the flow in the lowest 100 m. Easterly flow is also present in the lowest levels of the CAP on the east slope, with relatively undisturbed southwesterly flow just above it. Nondimensional mountain height ϵ can be used to test whether the conditions upstream of GM at this time would be conducive to blocked flow and the formation of an orographic wake. At the initiation of this LTF $\epsilon = 3$ due to a wind speed at 150 m AGL in the gap of 4.2 ms^{-1} and a Granite Ridge to Playa Station temperature difference of 9°C. This supports
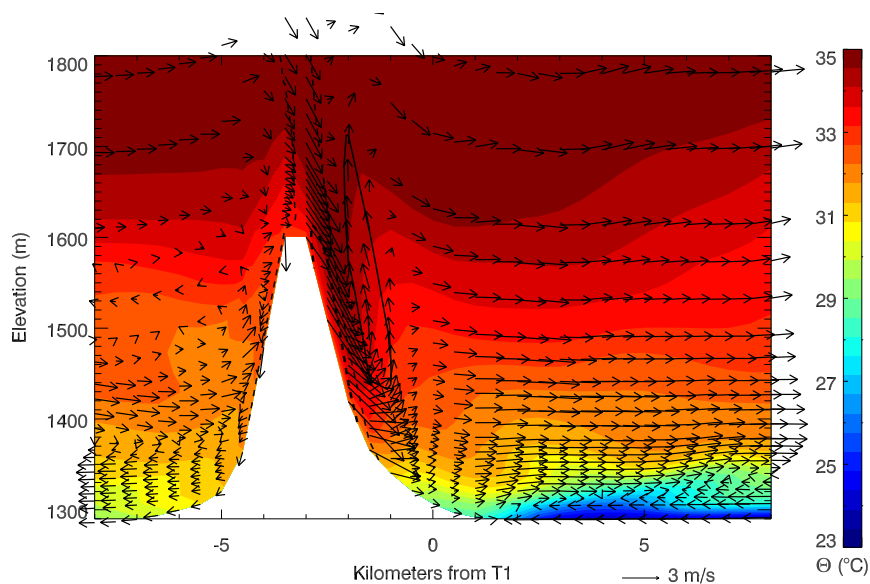
Fig. 3.10. Cross-section of zonal winds from WRF taken along the L1-L4 transect at 2340 MST on 2 October 2012. The cross-section is centered on L2/ES2. Color contours are potential temperature and wind vectors are winds in the x-z plane. Thin solid contours indicate vertical velocities above 0.2 m/s and thin dashed contours indicate vertical velocities below 0.2 m/s. Thick dashed contours indicate vertical velocities below -0.5 m/s. The size of the vectors in the z-direction is exaggerated by a factor of 10. This time is immediately before the LTF occurs at ES2 and L2.
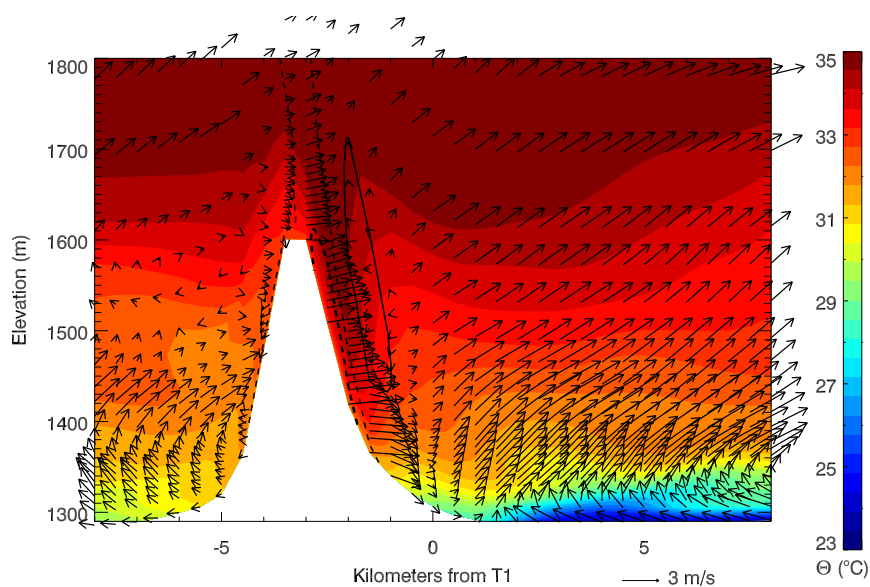

Fig. 3.11. Same as Fig. 3.10 except that the wind vectors are in the x-y plane and are proportionally sized.

the occurrence of blocked flow upstream of GM and a lee wake.

3.8   Discussion of LTF Causal Mechanisms

Our case study analysis of LTFs on the east slope of GM indicated that the observed LTFs were caused by a stably stratified westerly or southwesterly nocturnal flow interacting with GM, which produced an orographic wake and vertical-axis eddy in the lee of GM. The orographic wake and vertical-axis eddy disturb a CAP in the east basin. Displacement of the CAP along the east slope produces the observed LTFs. This mechanism is likely the cause for the large majority of LTFs observed along the east slope of Granite Mountain. We have shown that LTFs occur predominantly during nights where the mesoscale conditions favor the formation of orographic wakes. Furthermore, microscale atmospheric structures observed on the ES2 tower in the composite LTF are consistent with those produced by the orographic wake in the case study. For example, the orographic wake mechanism explains why the winds in the composite LTF at ES2 are consistently northerly or even northwesterly during the temperature drop, why there are relatively few LTFs on the west side of GM, and why LTFs occur later in the night at higher elevations of the east slope. This section will provide additional analysis of the orographic wake mechanism.

A conceptual understanding of the orographic wake is discussed here. The onset of orographic wake conditions occurs when southwesterly flow is impacting GM and the bulk lapse rate is near or below $-8°Ckm^{-1}$. Under these conditions blocking of the flow occurs on the upstream (western) side of GM. The blocked flow is approximately 100 m deep. Due to the upstream blocking, air from aloft descends to replace the colder surface air blocked upstream. Since it descends from crest level, this flow tends to be warm and acts to magnify the preexisting temperature gradient of the CAP on the east slope. While warm air from aloft replaces cold air on much of the east slope, cold low-level air from upstream of GM is able to flow freely past the southern end of GM. The lateral buoyancy gradient that results from these two airstreams causes the

formation of a vertical-axis eddy through the baroclinic generation of vorticity. As this counter-clockwise rotating eddy is inherently linked to the low-level baroclinicity on the east slope, on its northern end, it acts to advect cold air up the east slope in the vicinity of the instruments installed for MATERHORN. Variations in the strength of the warm flow descending from crest level and the periodic nature of the vertical-axis eddy produce significant variability in the location of the temperature gradient on the east slope. It is this variability that produces LTFs.

The orographic wake and an associated vertical-axis eddy observed here resemble those simulated in Epifanio and Rotunno (2005). Epifanio and Rotunno (2005) conducted idealized simulations prescribing a flow with nonuniform stratification ($\epsilon = 4$) impinging on a uniform terrain barrier with $\beta = 3$. Nonuniform stratification is a better approximation of the conditions observed upstream of GM than uniform stratification below the ridgetop height.

In the simulation by Epifanio and Rotunno (2005) the low-level flow is blocked on the upwind side. Warming occurs on the lee side of the barrier as potentially warmer air descends the lee side of the mountain replacing cold-air near the surface on the lee side. This results in a strong potential temperature gradient at the base of the mountain that resembles a density current that is continuously propagating upward against the flow. Furthermore, Epifanio and Rotunno (2005) demonstrate that the lowering of the isentropes on the lee side leads to positive buoyancy and baroclinic vorticity generation that induces the formation of counter-rotating vortices on both ends of the barrier. The WRF cross-section shown in Fig. 3.10 ($\epsilon \approx 3$) clearly displays the upstream blocking, lee warming, and the density current at the base of the terrain. Figs. 3.7 and 3.11 confirm the presence of a counter-rotating vortex (called a vertical-axis eddy here) confined within the stably-stratified CAP layer that advects the CAP up the slope in the shape of a density current.

Mean values of ϵ and β during LTFs indicate that conditions are conducive to developing an orographic wake. The average wind speed observed by the sodar at the

150 m level during LTFs is 3 ms^{-1}, and the average temperature at Granite Ridge is 6°C higher than at Playa Station. Assuming a barrier height of 500 m for GM, $\epsilon \approx 3$ under these conditions, meaning blocked flow is expected on the upstream side of GM, with potential for the development of an orographic wake. While assessment of ϵ in real-world situations can be difficult, the bulk stability method used here provides the best characterization of the incoming flow for situations where low-level blocking is expected (Reinecke and Durran 2008).

Dynamic terrain interactions have previously been advanced by Serafin et al. (2016) as a possible mechanism for temperature perturbations in the vicinity of GM. They identified high-frequency perturbations in the wind, temperature, and pressure fields in WRF simulations and used them as a proxy for identifying areas of flow separation at DPG. Our results confirm that dynamic terrain interactions are the cause of temperature perturbations, at least on the east slope of GM. Serafin et al. (2016) also speculate that this is in fact the cause for the LTFs (referred to as "collisions") discussed in Lehner et al. (2015), a conclusion that is also confirmed by this research.

It is possible that the CAP is merely advected by the vertical-axis eddy in the lee of GM to produce an LTF without contributing to the generation of the orographic wake or the vertical-axis eddy. Calculation of ϵ in the residual layer alone, below GM but above the CAP, shown in Fig. 3.3b, is rarely sufficient to generate the orographic wake. The CAP on the upstream side is likely necessary to produce the flow blocking that allows the orographic wake and vertical-axis eddy to form. The CAP on the eastern (lee) side of GM remains relatively quiescent until it is displaced by the dynamically induced flows.

Moderate sensitivity of the orographic wake to model configuration was found when comparing two separate planetary boundary layer schemes. Simulations utilizing the Yonsei University (YSU) planetary boundary layer scheme (Hong et al. 2006) produced an orographic wake and vertical-axis eddy at approximately the same time as the simulation utilizing the QNSE. However, the vertical-axis eddy was displaced

further from GM and did not produce an LTF at the location of ES2. Additionally, the modeled east basin CAP was weaker than the observed CAP. We expect that since LTFs on the east slope of GM are determined not just by the presence but also the positioning of the orographic wake, vertical-axis eddies, and the CAP, modeled LTFs are likely sensitive to model configuration. Accurate representation of the stratification of the CAP, stratification of residual layer, and of the boundary layer wind field are all critical to reproducing the orographic wake and the LTFs.

Much of the analysis in this study has focused on LTFs observed at the L2 level on the east slope. Orographic wakes are likely the primary causal mechanism of LTFs at L1, L3, and L4 as well. This is due to the fact that LTFs are observed on many of the same nights at each AWS and that the composite LTF structure at those stations is similar to that produced by LTFs at L2 (not shown). The clear differences in hourly LTF frequency at L1-L4 is likely attributable not to a different mechanisms, but to the deepening of the CAP through the night in the east basin. L2 observes more LTFs than the other AWSs likely because it is at an elevation corresponding to the mean depth of the CAP on the east slope. The height of L1 corresponds to the CAP top only in the evening hours, leading to the evening peak in LTFs there. The top of the CAP is almost always below the height of L4, and only very vigorous CAP displacements reach that level. If another mechanism was responsible for LTFs observed anywhere on the slope, it would likely be in the early evening at L1. From 1800-1900 MST, the stable boundary layer structure may not be sufficiently stable to produce an orographic wake, or the southwesterly flow has not yet developed. LTFs at this time at L1 are likely due to the displacement of a shallow CAP but due to mechanisms other than that of an orographic wake.

Other areas of DPG not discussed here see high frequencies of LTFs (see Fig. 3.1). One location is at the northern tip of the Dugway Range. Based on evidence from WRF simulations, this area is likely impacted by wakes forming in the lee of the Dugway Range in a similar fashion as those impacting the east slope of GM. A large

number of LTFs are also observed at one AWS in the southern end of the east basin at a similar elevation to L3. It is possible that an orographic wake affects this location due to southerly flow impacting the mountain to its south, disturbing the CAP. A third AWS, on the northern end of the east basin, also observes a large number of LTFs. The location of this AWS is very close to the elevation of L3, indicating that CAP displacement may be the cause of LTFs there. However, the mechanism for CAP displacement there remains unknown.

The improved understanding of flow interactions near GM presented here is expected to benefit operational forecasting at DPG. DPG is one of the primary test centers of the United States Army Test and Evaluation Command, and high-resolution weather forecasts are regularly required to support operations there. Several of the primary test locations are located in the east basin and on the slopes of GM. Many tests at DPG are highly sensitive to wind speed and direction and require detailed forecasts of winds at long lead times. The improved understanding of flows and their interactions will allow DPG forecasters to better interpret numerical model output and improve forecast skill. While the mesoscale model simulations that are used operationally by DPG forecasters may not be able to accurately predict orographic wakes near Granite Mountain accurately in space or time, awareness of the conditions conducive for orographic wake formation will allow forecasters to anticipate their occurence and incorporate this knowledge into their forecasts.

3.9   Conclusions

This study used an automated algorithm to identify large temperature fluctuations (LTFs), defined as a temperature drop of at least 3°C within 30 min followed by a partial temperature recovery, in a systematic fashion. Analysis of the spatial and temporal characteristics of LTFs showed that they are most common from 2200 MST to 0800 MST on the slopes of GM, with the frequency of LTFs on the east slope much higher than on the western slopes of GM.

LTFs occur most often under stably stratified westerly or southwesterly flow impinging on GM. This flow is blocked at low levels and an orographic wake with associated vertical axis eddies is formed in the lee of GM. This wake intensifies the preexisting horizontal temperature gradient due to the CAP along the east slope of GM. Changes in strength of the orographic wake and the vertical-axis eddy cause the location of this temperature gradient to fluctuate along the slope, leading to LTFs. This mechanism is likely to impact the entire east slope of GM.

The composite LTF compiled for the location with the highest frequency of LTF shows that the temperature drop is largest at the mid-levels of a 20-m tower. Winds are typically westerly before the LTF and show the signature of a katabatic flow, northerly during the temperature fall, and then return to westerly after the temperature recovers. LTFs display amplitudes of $3 - 13^\circ$C and occur on timescales of 30-90 min.

Numerical simulations of phenomena such as orographic wakes are frequently conducted using idealized or semi-idealized numerical simulations. This study offers unique observational evidence for the flows identified in numerical simulations. The uniquely dense observational network on the east slope of DPG made such a comparison possible, and further investigation of mountain wave- type flows could be pursued using the available dataset.

The presented results offer MATERHORN investigators a much-improved understanding of flow interactions with GM that may be useful for future model verification and development. A logical extension of this study would be to conduct a thorough model verification and sensitivity study using the MATERHORN observational dataset. Sensitivity to boundary layer scheme, advective scheme, or other model parameters could be tested. The ability of WRF to simulate LTFs under different large-scale conditions could be assessed, as well as an analysis of the variability of the orographic wake from night to night.

3.10   References

Blumen, W., R. L. Grossman, and M. Piper, 1999: Analysis of heat budget, dissipation and frontogenesis in a shallow density current. *Bound.-Layer Meteor.*, **91**, 281–306, doi:10.1023/A:1001813700928.

Brown, A. R., M. Athanassiadou, and N. Wood, 2003: Topographically induced waves within the stable boundary layer. *Quart. J. Roy. Meteor. Soc.*, **129**, 3357–3370, doi: 10.1256/qj.02.176.

Cheung, T. K., and C. G. Little, 1990: Meteorological tower, microbarograph array, and sodar observations of solitary-like waves in the nocturnal boundary layer. *J. Atmos. Sci.*, **47**, 2516–2536, doi:10.1175/1520-0469(1990)047<2516:MTMAAS>2.0.CO;2.

Clements, C. B., C. D. Whiteman, and J. D. Horel, 2003: Cold-air-pool structure and evolution in a mountain basin: Peter Sinks, Utah. *J. Appl. Meteor*, **42**, 752–768.

De Wekker, S. F. J., and C. D. Whiteman, 2006: On the time scale of nocturnal boundary layer cooling in valleys and basins and over plains. *J. Appl. Meteor. Climatol.*, **45**, 813–820, doi:10.1175/JAM2378.1.

Dimitrova, R., Z. Silver, T. Zsedrovits, C. Hocut, L. Leo, S. Di Sabatino, and H. S. Fernando, 2015: Assessment of planetary boundary-layer schemes in the weather research and forecasting mesoscale model using MATERHORN field data. *Bound.-Layer Meteor.*, 1–21, doi:10.1007/s10546-015-0095-8.

Doran, J. C., and T. W. Horst, 1981: Velocity and temperature oscillations in drainage winds. *J. Appl. Meteor*, **20**, 361–364, doi:10.1175/1520-0450(1981)020<0361:VATOID>2.0.CO;2.

Dudhia, J., 1989: Numerical study of convection observed during the winter monsoon experiment using a mesoscale two-dimensional model. *J. Atmos. Sci.*, **46**, 3077–3107, doi:10.1175/1520-0469(1989)046<3077:NSOCOD>2.0.CO;2.

Epifanio, C. C., 2003: *Lee Vortices*, 1150–1160. Academic Press, Oxford, doi: http://dx.doi.org/10.1016/B0-12-227090-8/00241-4.

Epifanio, C. C., and R. Rotunno, 2005: The dynamics of orographic wake formation in flows with upstream blocking. *J. Atmos. Sci.*, **62**, 3127–3150, doi: 10.1175/JAS3523.1.

Fernando, H. J. S., and Coauthors, 2015: The MATERHORN - unraveling the intricacies of mountain weather. *Bull. Amer. Meteor. Soc.*, doi:10.1175/BAMS-D-13-00131.1.

Grachev, A. A., L. S. Leo, S. D. Sabatino, H. J. S. Fernando, E. R. Pardyjak, and C. W. Fairall, 2015: Structure of turbulence in katabatic flows below and above the

wind-speed maximum. *Bound.-Layer Meteor.*, 1–26, doi:10.1007/s10546-015-0034-8.

Haiden, T., and C. D. Whiteman, 2005: Katabatic flow mechanisms on a low-angle slope. *J. Appl. Meteor*, **44**, 113–126, doi:10.1175/JAM-2182.1.

Holtslag, A. A. M., and Coauthors, 2013: Stable atmospheric boundary layers and diurnal cycles: Challenges for weather and climate models. *Bull. Amer. Meteor. Soc.*, **94**, 1691–1706, doi:10.1175/BAMS-D-11-00187.1.

Hong, S.-Y., Y. Noh, and J. Dudhia, 2006: A new vertical diffusion package with an explicit treatment of entrainment processes. *Mon. Wea. Rev.*, **134**, 2318–2341, doi:10.1175/MWR3199.1.

Jensen, D. D., D. F. Nadeau, S. W. Hoch, and E. R. Pardyjak, 2016: Observations of near-surface heat-flux and temperature profiles through the early evening transition over contrasting surfaces. *Bound.-Layer Meteor.*, 1–21, doi:10.1007/s10546-015-0067-z.

Johnson, R. H., R. S. Schumacher, J. H. R. Jr., D. T. Lindsey, J. E. Ruthford, and L. Kriederman, 2014: The role of convective outflow in the Waldo Canyon Fire. *Mon. Wea. Rev.*, **142**, 3061–3080, doi:10.1175/MWR-D-13-00361.1, `http://dx.doi.org/10.1175/MWR-D-13-00361.1`.

Lack, S. A., G. L. Limpert, and N. I. Fox, 2010: An object-oriented multiscale verification scheme. *Wea. Forecasting*, **25**, 79–92, doi:10.1175/2009WAF2222245.1.

Lareau, N. P., E. Crosman, C. D. Whiteman, J. D. Horel, S. W. Hoch, W. O. Brown, and T. W. Horst, 2013: The Persistent Cold-Air Pool Study. *Bull. Amer. Meteor. Soc.*, **94**, 51–63.

Lareau, N. P., and J. D. Horel, 2014: Dynamically induced displacements of a persistent cold-air pool. *Bound.-Layer Meteor.*, **154**, 291–316, doi:10.1007/s10546-014-9968-5.

Lee, T. J., R. A. Pielke, R. C. Kessler, and J. Weaver, 1989: Influence of cold pools downstream of mountain barriers on downslope winds and flushing. *Mon. Wea. Rev.*, **117**, 2041–2058, doi:10.1175/1520-0493(1989)117<2041:IOCPDO>2.0.CO;2.

Lehner, M., C. D. Whiteman, S. W. Hoch, D. Jensen, E. R. Pardyjak, L. S. Leo, S. Di Sabatino, and H. J. S. Fernando, 2015: A case study of the nocturnal boundary layer evolution on a slope at the foot of a desert mountain. *J. Appl. Meteor. Climatol.*, **54**, 732–751, doi:10.1175/JAMC-D-14-0223.1.

Lin, Y.-L., R. D. Farley, and H. D. Orville, 1983: Bulk parameterization of the snow field in a cloud model. *J. Clim. Appl. Meteor.*, **22**, 1065–1092, doi:10.1175/1520-0450(1983)022<1065:BPOTSF>2.0.CO;2.

Lin, Y.-L., T.-A. Wang, and R. P. Weglarz, 1993: Interactions between gravity waves and cold air outflows in a stably stratified uniform flow. *J. Atmos. Sci.*, **50**, 3790–3816, doi:10.1175/1520-0469(1993)050<3790:IBGWAC>2.0.CO;2.

Massey, J. D., W. J. Steenburgh, S. W. Hoch, and J. C. Knievel, 2014: Sensitivity of near-surface temperature forecasts to soil properties over a sparsely vegetated dryland region. *J. Appl. Meteor. Climatol.*, **53**, 1976–1995, doi:10.1175/JAMC-D-13-0362.1.

Mlawer, E. J., S. J. Taubman, P. D. Brown, M. J. Iacono, and S. A. Clough, 1997: Radiative transfer for inhomogeneous atmospheres: RRTM, a validated correlated-k model for the longwave. *J. Geo. Res. Atmos.*, **102**, 16 663–16 682, doi:10.1029/97JD00237.

Mueller, C. K., and R. E. Carbone, 1987: Dynamics of a thunderstorm outflow. *J. Atmos. Sci.*, **44**, 1879–1898, doi:10.1175/1520-0469(1987)044<1879:DOATO>2.0.CO;2.

Neemann, E. M., E. T. Crosman, J. D. Horel, and L. Avey, 2015: Simulations of a cold-air pool associated with elevated wintertime ozone in the Uintah Basin, Utah. *Atmos. Chem. Phys.*, **15**, 135–151, doi:10.5194/acp-15-135-2015.

Neff, W. D., and C. W. King, 1989: The accumulation and pooling of drainage flows in a large basin. *J. Appl. Meteor*, **28**, 518–529, doi:10.1175/1520-0450(1989)028<0518:TAAPOD>2.0.CO;2.

Reinecke, P. A., and D. Durran, 2009a: The overamplification of gravity waves in numerical solutions to flow over topography. *Mon. Wea. Rev.*, **137**, 1533–1549, doi:10.1175/2008MWR2630.1.

Reinecke, P. A., and D. R. Durran, 2008: Estimating topographic blocking using a Froude number when the static stability is nonuniform. *J. Atmos. Sci.*, **65**, 1035–1048, doi:10.1175/2007JAS2100.1.

Reinecke, P. A., and D. R. Durran, 2009b: Initial-condition sensitivities and the predictability of downslope winds. *J. Atmos. Sci.*, **66**, 3401–3418, doi: 10.1175/2009JAS3023.1.

Rife, D. L., T. T. Warner, F. Chen, and E. G. Astling, 2002: Mechanisms for diurnal boundary layer circulations in the Great Basin Desert. *Mon. Wea. Rev.*, **130**, 921–938, doi:10.1175/1520-0493(2002)130<0921:MFDBLC>2.0.CO;2.

Serafin, S., S. J. De Wekker, and J. Knievel, 2016: A mesoscale model-based climatography of nocturnal boundary-layer characteristics over the complex terrain of north-western Utah. *Bound.-Layer Meteor.*, 1–25, doi:10.1007/s10546-015-0044-6.

Shafer, J. C., and W. J. Steenburgh, 2008: Climatology of strong Intermountain cold

fronts. *Mon. Wea. Rev.*, **136**, 784–807, doi:10.1175/2007MWR2136.1.

Skamarock, W., and Coauthors, 2008: A description of the Advanced Research WRF Version 3. Tech. Rep. NCAR/TN-475+STR, NCAR Technical Note.

Steinacker, R., and Coauthors, 2007: A sinkhole field experiment in the Eastern Alps. *Bull. Amer. Meteor. Soc.*, **88**, 701–716.

Stull, R. B., 1976: Internal gravity waves generated by penetrative convection. *J. Atmos. Sci.*, **33**, 1279–1286, doi:10.1175/1520-0469(1976)033<1279:IGWGBP>2.0.CO;2.

Sukoriansky, S., B. Galperin, and I. Staroselsky, 2005: A quasinormal scale elimination model of turbulent flows with stable stratification. *Phys. Fluids*, **17**, 085107, doi:http://dx.doi.org/10.1063/1.2009010.

Whiteman, C. D., S. Zhong, W. J. Shaw, J. M. Hubbe, X. Bian, and J. Mittelstadt, 2001: Cold pools in the Columbia Basin. *Wea. Forecasting*, **16**, 432–447, doi:10.1175/1520-0434(2001)016<0432:CPITCB>2.0.CO;2.

Wolyn, P. G., and T. B. McKee, 1989: Deep stable layers in the intermountain western United States. *Mon. Wea. Rev.*, **117**, 461–472, doi:10.1175/1520-0493(1989)117<0461:DSLITI>2.0.CO;2.

CHAPTER 4

CONCLUSIONS

4.1 Summary of Findings

Near-surface winds in Northern Utah result from the complex interaction of flows forced on multiple scales ranging from synoptic scale troughs and ridges to individual slope flows. The resulting near-surface winds, and the forcing mechanisms associated with them, vary temporally based on the seasonal and diurnal evolution of the atmospheric boundary layer and large-scale weather patterns. Spatial variations in the near-surface winds and forcing mechanisms also arise due to changes in terrain and the land surface.

In this thesis, two approaches are taken to advance our knowledge of the multiscale flow interactions in the DPG area. In the first approach, an analysis of a long-term dataset highlights the importance synoptic scale and mesoscale processes that shape the observed wind field on diurnal and seasonal time scales. In the second approach, microscale signatures were analyzed (large temperature fluctuations (LTFs)). Analysis of the spatial and temporal distribution of LTFs and the mechanisms causing them revealed complex interactions of mesoscale and microscale flows with terrain.

In Chapter 2, seventeen years of surface wind data were used to characterize the surface wind climatology at Dugway Proving Ground (DPG). Surface winds were found to be bimodal, with the two modes referred to as the northerly regime and the southerly regime based on the predominate direction during each mode. Since the bimodality persists at hours when thermally driven flows would produce a single dominant direction, thermally driven flows are not the cause of the bimodality. The

bimodality is found to be caused by seasonally varying synoptic and mesoscale processes that combine to produce a tripolar seasonal distribution of regime frequency, with the southerly regime most common in August and January and the northerly regime most common in May. These processes include thermally induced low pressure in the Intermountain West, lee troughing east of the Sierra Nevada, the position of the GBCZ, and regional-scale thermally induced circulations. Additionally, the prototypical synoptic patterns associated with the northerly and southerly regimes correspond to those of the West Coast Thermal Trough and North American Monsoon, respectively. Local thermally driven circulations were a secondary contributor.

In Chapter 3 the structure of the planetary boundary layer in the vicinity of Granite Mountain (GM) was studied in order to identify the cause of the LTFs found there. GM was the focus for studying LTFs due to the large number of LTFs observed on its east slope and the large number of instruments in that area. The east slope of GM has the highest frequency of large temperature fluctuations at DPG, with an average of 3 per day. The west slope of GM displayed relatively few LTFs. LTF frequencies were uniformly low on the floor of the east basin and at mountaintop stations. The primary cause of LTFs was determined to be an orographic wake that forms in the lee of GM due to blocking of the low-level stratified southwesterly flow on the upstream side. As a result of this blocking, warm air from ridgetop level descends the lee side of GM, enhancing the strong thermal gradient already present due to a cold-air pool (CAP). Fluctuations in the incident flow or the development of vertical-axis eddies on the edge of the wake produce LTFs by perturbing this temperature gradient. This mechanism explains why the wind is northerly instead of easterly when the cold air arrives, why the east slope of GM has many more LTFs than the west slope, and why the maximum hourly LTF frequency on the east slope occurs later in the night as one moves up the slope.

As discussed in the Introduction, the Mountain Terrain Atmospheric Modeling and Observations (MATERHORN) program was designed with an overarching goal of

improving weather prediction in complex terrain through (1) increasing our knowledge of flow processes there and (2) improving numerical model performance. This work has made significant progress in pursuit of understanding flow processes in complex terrain at DPG, with applicability to other areas.

Two papers published through the MATERHORN program have speculated about the forcing mechanisms of the flows in the playa and east basin (Fernando et al. 2015; Lehner et al. 2015). In both studies thermally driven flows were expected to be dominant, possibly due in part to prior research in these areas by Rife et al. (2002). Here we have established that much of the playa and east basin are influenced by forcings on the mesoscale and synoptic scale. The finding that flows in the east basin and Playa are predominately forced by processes on these scales is important for a wide range of MATERHORN investigations, including the analysis of flux tower data at the Playa Site, Sagebrush Site, and lower sites on the east slope.

Previous studies focused on the east slope (Dimitrova et al. 2015; Fernando et al. 2015; Lehner et al. 2015; Serafin et al. 2016) have also had to speculate on the significant temperature disturbances that were explicitly or implicitly observed there. Fernando et al. (2015) proposed a mechanism for these disturbances, in which convergence of southwesterly flow through the Gap and southeasterly flow in the east basin resulted in the east basin CAP being displaced up the east slope. This work presents a more complete and comprehensive explanation for the LTFs: stratified flow produces an orographic wake that displaces the east slope CAP. Integration of this mechanism into our understanding of flow systems on the east slope is very important, as the east slope is the focus of considerable MATERHORN research. LTFs can affect all 5 flux towers that were deployed on the east slope and occur at a minimum of one location on the east slope during the majority of nights. Future work can be focused on LTF-producing phenomena or designed to avoid LTFs. For instance, studies of katabatic flows such as Grachev et al. (2015) on the east slope can largely avoid LTFs by focusing on the evening period before 2000 MST at the L3 level and

higher. Alternatively, numerous nights during the MATERHORN field experiments display multiple LTFs. The large dataset of LiDAR observations focused on flows on the east slope of GM could be analyzed on these nights to better understand the wake evolution.

The improved understanding of multiscale flow interactions presented here is expected to benefit operational forecasting at DPG. High-resolution weather forecasts are required to support many customers at DPG that are sensitive to small variations in wind speed and direction. The conceptual models presented here can enhance the ability of forecasters to interpret numerical model guidance and better anticipate favorable or unfavorable wind conditions.

A number of methods for assessing the degree of large-scale forcing on the surface wind were assessed through the course of this work and no distinctive separation could be made between days with strong synoptic forcing and weak synoptic forcing. This is primarily attributable to multiscale flow interactions. Forcing mechanisms at DPG appear to be continuous across the spectrum of spatial scales such that any division between strong versus weak forcing (or similarly, remote versus local forcings) is relatively artificial and may include scales of motion that are intended to be excluded.

As a result, this research suggests caution when using simple evaluations of synoptic forcing at DPG, due to the difficulty of making such determinations. Fernando et al. (2015) and Zhang et al. (2013) both utilized simple metrics to characterize conditions observed at DPG by the strength of synoptic forcing. However, many nights considered "quiescent" according to the Fernando et al. (2015) metric experience frequent LTFs on the east slope, significantly disturbing the katabatic flow that was expected there under "quiescent" conditions. The nocturnal flow that causes LTFs is neither synoptically driven nor thermally driven in the classical sense, as it likely arises from regional scale thermal contrasts. Similarly, southeasterly flow observed at the Sagebrush Site in the east basin on a "quiescent" night may be driven more by

mesoscale thermal contrasts than by a local playa breeze or downvalley flow.

The difficulty in assessing large scale forcing is likely to be observed in other areas of complex terrain. If classification of weak or strong synoptic forcing is necessary, then objective, clearly defined metrics should be used that are site-specific. Additionally, field experiments should be designed so as to measure as many scales of motion as possible, to allow for robust determinations to be made of the forcing mechanisms pertinent to a given flow.

Much of the published research on orographic wakes is limited to idealized or semi-idealized simulations, and this work offers an observational confirmation of an orographic wake closely resembling those in the numerical simulations of Epifanio and Rotunno (2005). The density of observational data on the east slope of GM offers a unique opportunity to observe the orographic wake and its surrounding environment, and demonstrates the value of deploying dense observational networks in field experiments in complex terrain. It is expected that the orographic wake and LTFs found here occur at many other locations in complex terrain where persistent stratified nocturnal flow interacts with terrain.

While this work has not assessed model performance, the findings presented here are applicable to such work. Model verification efforts such as those by Zhang et al. (2013) and Dimitrova et al. (2015) require a deep knowledge of the possible forcing mechanisms of the wind in order that the correct conclusions are reached regarding the shortcomings of a numerical model. This research encourages significant investigation in the form of case studies to ensure that the model adequately simulates the pertinent flow features, rather than simply maximizing statistical measures of model skill.

4.2   Future Work

Three specific recommendations will be made here for extending this work. First, an extensive WRF verification experiment could be performed to ascertain how well WRF can simulate the bimodal distribution of wind that constitutes the northerly and

southerly regimes. This could be done using long-term WRF runs used for climate research. The same WRF dataset could also be used to test the ability of WRF to reproduce the tripolar seasonal distribution of the regimes. The degree to which WRF can or cannot reproduce the climatological conditions in a given month would offer significant insight into which forcing mechanisms are not accurately simulated.

Second, WRF could also be used to test the sensitivity of flows at DPG (i.e. the southeasterly nocturnal flow in the east basin) to the presence of certain land-surfaces (i.e., the Playa or Great Salt Lake) or topographic features (i.e., the Cedar Mountains or the Dugway Range). Individual terrain features can be removed and changes to the flow can be quantified. Terrain features can be linked to certain forcing mechanisms, allowing mechanisms to be confirmed or ruled out. Since it would be unknown *a priori* whether a high-quality WRF simulation was due to coincidence or skill, such research would have to be carried out with this fact in mind. Analyzing multiple cases during different seasons would be very beneficial. When combined with the first task, this work would offer a much higher degree of certainty as to the contributions of different forcing mechanisms to the wind flows at DPG.

Third, WRF could also offer more insight to CAP displacements on the east slope of Granite Mountain. Additional real data or semi-idealized simulations run at large-eddy scales would allow a more in-depth analysis of the dynamically induced orographic wakes. Additionally, the location of the orographic wake was found in this work to be sensitive to a simple change of the boundary layer parameterization. Additional sensitivity tests involving the boundary layer parameterization, horizontal and vertical grid resolution, horizontal advection scheme, or land surface parameterization could be insightful.

Further work on LTFs could also involve identifying causal mechanisms for large temperature fluctuations at sites other than the east slope of GM using observations and numerical simulations. Preliminary evidence indicates that LTFs elsewhere are likely caused by CAP displacements. Establishing the cause of LTFs across DPG

would be useful to MATERHORN investigators.

4.3   References

Dimitrova, R., Z. Silver, T. Zsedrovits, C. Hocut, L. Leo, S. Di Sabatino, and H. S. Fernando, 2015: Assessment of planetary boundary-layer schemes in the weather research and forecasting mesoscale model using MATERHORN field data. *Bound.-Layer Meteor.*, 1–21, doi:10.1007/s10546-015-0095-8.

Epifanio, C. C., and R. Rotunno, 2005: The dynamics of orographic wake formation in flows with upstream blocking. *J. Atmos. Sci.*, **62**, 3127–3150, doi:10.1175/JAS3523.1.

Fernando, H. J. S., and Coauthors, 2015: The MATERHORN - unraveling the intricacies of mountain weather. *Bull. Amer. Meteor. Soc.*, doi:10.1175/BAMS-D-13-00131.1.

Grachev, A. A., L. S. Leo, S. D. Sabatino, H. J. S. Fernando, E. R. Pardyjak, and C. W. Fairall, 2015: Structure of turbulence in katabatic flows below and above the wind-speed maximum. *Bound.-Layer Meteor.*, 1–26, doi:10.1007/s10546-015-0034-8.

Lehner, M., C. D. Whiteman, S. W. Hoch, D. Jensen, E. R. Pardyjak, L. S. Leo, S. Di Sabatino, and H. J. S. Fernando, 2015: A case study of the nocturnal boundary layer evolution on a slope at the foot of a desert mountain. *J. Appl. Meteor. Climatol.*, **54**, 732–751, doi:10.1175/JAMC-D-14-0223.1.

Rife, D. L., T. T. Warner, F. Chen, and E. G. Astling, 2002: Mechanisms for diurnal boundary layer circulations in the Great Basin Desert. *Mon. Wea. Rev.*, **130**, 921–938, doi:10.1175/1520-0493(2002)130<0921:MFDBLC>2.0.CO;2.

Serafin, S., S. J. De Wekker, and J. Knievel, 2016: A mesoscale model-based climatography of nocturnal boundary-layer characteristics over the complex terrain of north-western Utah. *Bound.-Layer Meteor.*, 1–25, doi:10.1007/s10546-015-0044-6.

Zhang, H., Z. Pu, and X. Zhang, 2013: Examination of errors in near-surface temperature and wind from wrf numerical simulations in regions of complex terrain. *Wea. Forecasting*, **28**, 893–914, doi:10.1175/WAF-D-12-00109.1.

APPENDIX A

SUMMARY OF ADDITIONAL EXPERIENCE

During my tenure in the PhD program, I completed a one-year internship with the National Weather Service in Salt Lake City and I participated in 4 field experiments. I also gave 12 public outreach presentations on topics related to mountain weather, avalanches, and climate change. Most of these events were fundraisers for the Utah Avalanche Center. The internship and field experience will be detailed below.

A.1 National Weather Service Internship

In June 2015, I began a National Weather Service Pathways Internship based at the weather forecast office (WFO) in Salt Lake City. The internship included 640 hrs of work and lasted until June 2016. I spent an average of 15 hrs per week working on a variety of projects and helping create operational forecasts. My initial project involved identifying the conditions conducive for extreme snowfall in the Ogden Valley, 40 miles northeast of Salt Lake City. The Ogden Valley is prone to receiving exceptional snowfall totals, frequently exceeding 18 in in 24 hrs. Using observations and ERA-Interim reanalysis data I identified the synoptic patterns that produce large snowfalls. Despite the relatively small size of the valley, the north and south ends of it receive heavy snowfalls under significantly different large-scale flow regimes. This was a surprising result with implications for the issuance of Winter Storm Warnings. This information was presented at the WFO's Fall Seminar and was detailed in a short paper. In order to make the information easy for forecasters to access, I also developed a simple web page to display this information.

My second project involved developing a climatology of fog at the airports where terminal aerodrome forecasts (TAFs) are issued. The significant visibility reduction that occurs in fog is extremely important to airport operations, and therefore, is an important forecast challenge in the TAF. I analyzed hourly fog occurrence based on observations from the present weather sensor at 10 automated surface observation system (ASOS) stations. The fog climatology was placed on a web page for easy forecaster access.

My third project examined easterly high wind events along the Wasatch Front from 1978-2015 for the purpose of developing simple forecast metrics, resolvable by global models, that could improve forecast skill and lead time for such events. A mixture of surface observations and damage reports were used to construct a historical record of events that exceeded the High Wind Warning criteria of 26 ms^{-1} on the west slope of the Wasatch Range between Bountiful, UT and Ogden, UT. ERA-Interim data were then used to test the ability of various synoptic metrics to identify warning-level winds events as well as to differentiate gap wind events from downslope windstorms. It was found that a simple combination of zonal 700 mb wind speed and the sea level pressure gradient between Ogden, UT and Rock Springs, WY performed these tasks well. This knowledge was incorporated into a color-coded multi-model situational awareness table. With this table forecasters can assess how often the conditions forecast by a model at a given time have produced high winds in the past. The table can be accessed by forecasters via a web page.

Lastly, I spent significant time developing and issuing forecast products. I most commonly worked the "Aviation" forecast desk where I was responsible for issuing the 1800 UTC TAFs, for monitoring and amending those TAFs if necessary, for producing gridded forecast products from Day 4 through Day 7, and for writing forecast discussions for both the aviation products and for the long-term forecast. On several occasions I was also responsible for the short-term forecast products (present time through Day 3).

A.2 Field Experience

This section will detail my work on 4 field campaigns. The four field experiments were the MATERHORN Fall Experiment, MATERHORN Spring Experiment, the second Meteor Crater Experiment (METCRAX II), and the MATERHORN Fog Experiment.

The MATERHORN Fall Experiment ran from 25 September - 31 October 2012. I assisted in planning IOPs, conducting IOPs, and forecasting for MATERHORN Fall. I was involved in planning and initial field preparation from the time I entered the PhD program in September 2011 until the experiment began. A significant number of days were spent in the field installing instrumentation. During the experiment, I prepared a forecast for the approximately daily planning meetings that would occur. The primary forecast objective for MATERHORN was to accurately characterize the degree of forcing of the large-scale flow on the boundary layer for IOP planning purposes. Ten 24-hr IOPs were conducted during the experiment. During IOPs I was primarily responsible for the operation of a tethered balloon on the Playa. When travel and preparation time is included, each IOP required 28-30 hrs to complete.

The MATERHORN Spring Experiment ran from 1-31 May 2012. My involvement during MATERHORN Spring was very similar to that in MATERHORN Fall with the exception of a more prominent role in forecast decisions. MATERHORN Spring also included 10 24-hr IOPs.

METCRAX II ran from 30 September - 30 October 2013. Seven IOPs were conducted during this time. The primary objective of the METCRAX II program was to study downslope windstorm-type flows in the Meteor Crater in Arizona. I was heavily involved with the deployment of instrumentation into the crater, which included many ascents and descents of the crater on foot carrying equipment. The instrument deployment included an additional weekend trip to Flagstaff prior to the residence time there. Along with the rest of the METCRAX II team, I lived in Flagstaff, AZ for nearly 6 weeks beginning in mid-September 2013 to conduct the experiment.

I was the lead forecaster for the METCRAX II program. The primary forecast objective during METCRAX was to identify quiescent periods where the flows above and in the Meteor Crater would be thermally driven. This was a difficult task as significant shear was often observed in the lowest levels of the atmosphere that was inconsistent with both the synoptic flows and expected thermally driven flows. Weather forecast briefings were given on nearly a daily basis. During IOP's I was responsible for the coordinating the operation of tethered balloons in the crater. All IOPs were conducted at night and generally lasted from 1600-0930 MST. Including travel and set-up time, each IOP required nearly 24 hrs to complete.

The MATERHORN Fog Experiment ran from 1-31 January 2015. I was the primary forecaster for MATERHORN Fog and led daily forecast briefings throughout the experimental period. Forecasts were focused on accurately predicting nights when fog would be observed in the Heber Valley southeast of Salt Lake City, UT. Fog forecasting was a very difficult task due to the tenuous nature of fog in the Heber Valley and the generally unfavorable conditions experienced during January 2015. Forecasts and briefings were conducted in Salt Lake City and generally required 1-2 hrs to prepare and present. Unlike the previous 3 field experiments where I participated in the field during all IOPs, in MATERHORN Fog, I only assisted in operating instruments during one overnight IOP.

APPENDIX B

MEAN DIURNAL HODOGRAPHS FOR ALL MONTHS

In Chapter 2, monthly mean hodographs were shown in Figure 2.8 only for the months of January, May, and August. Figs. B.1 and B.2 are shown here to provide a reference for the diurnal evolution over all months.
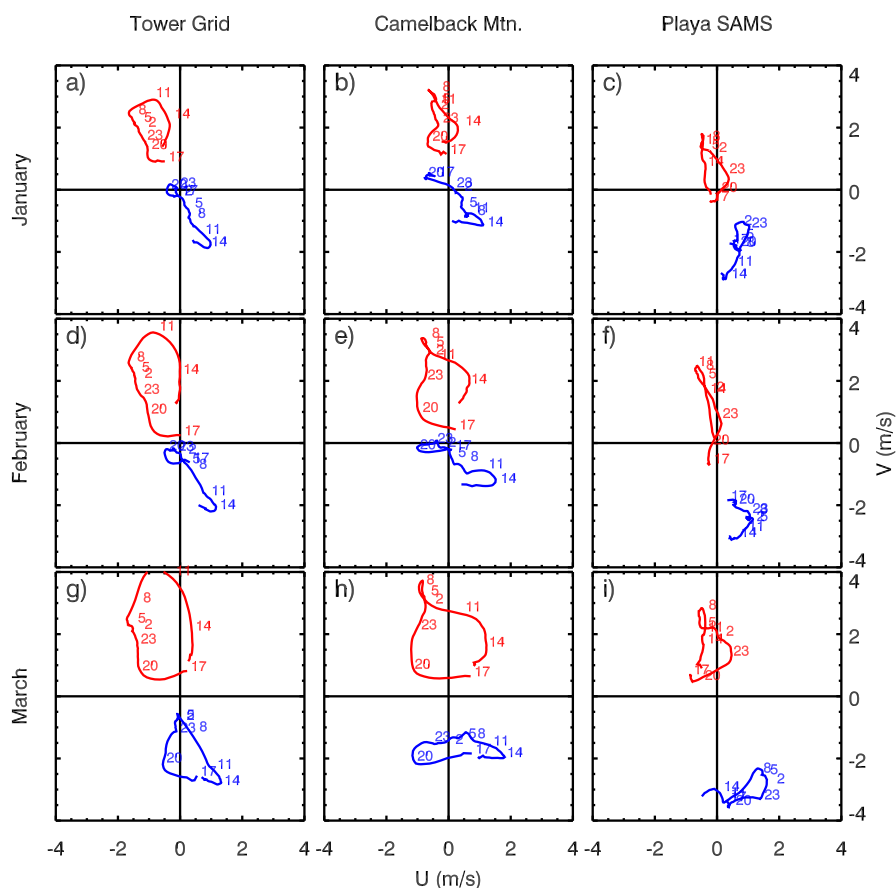
Fig. B.1. Temporal hodographs illustrating the diurnal wind evolution at three surface meteorological stations during January, February, and March. Each line traces the composite mean wind vector with a time resolution of 15 min. The lines are labeled every 3 hrs in MST. Red lines show composite means of southerly regime days at the given station in the given month. Blue lines show composite means of northerly regime days. Each diurnal cycle shown has a sample size of at least 200 days.
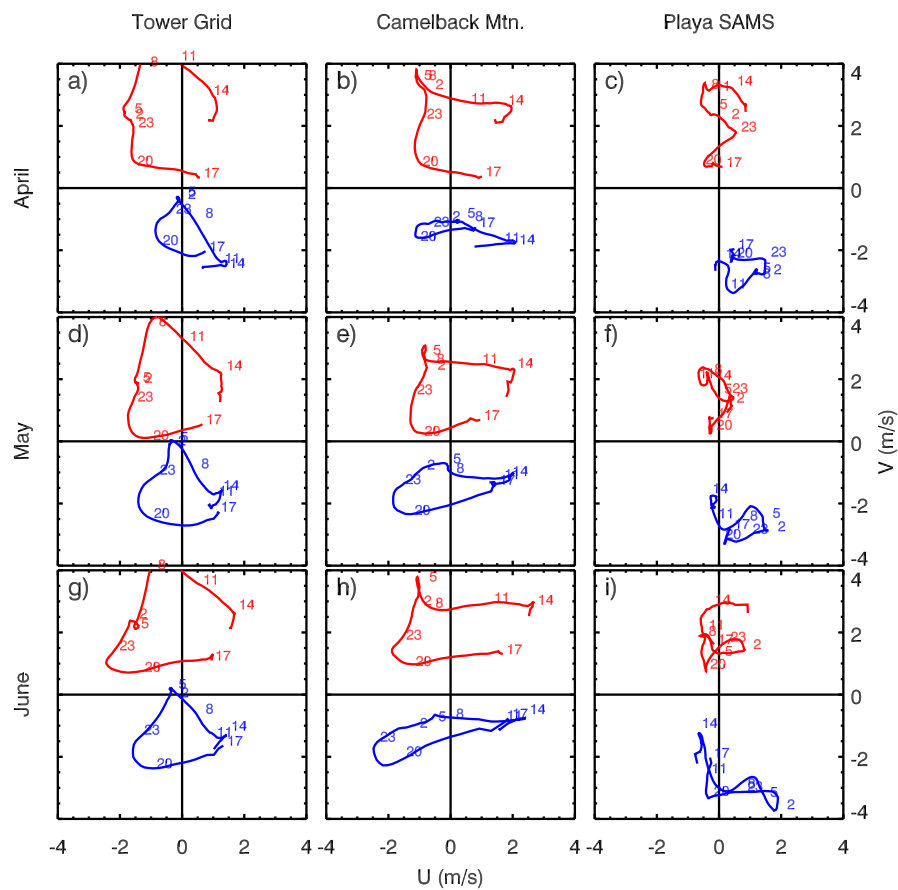
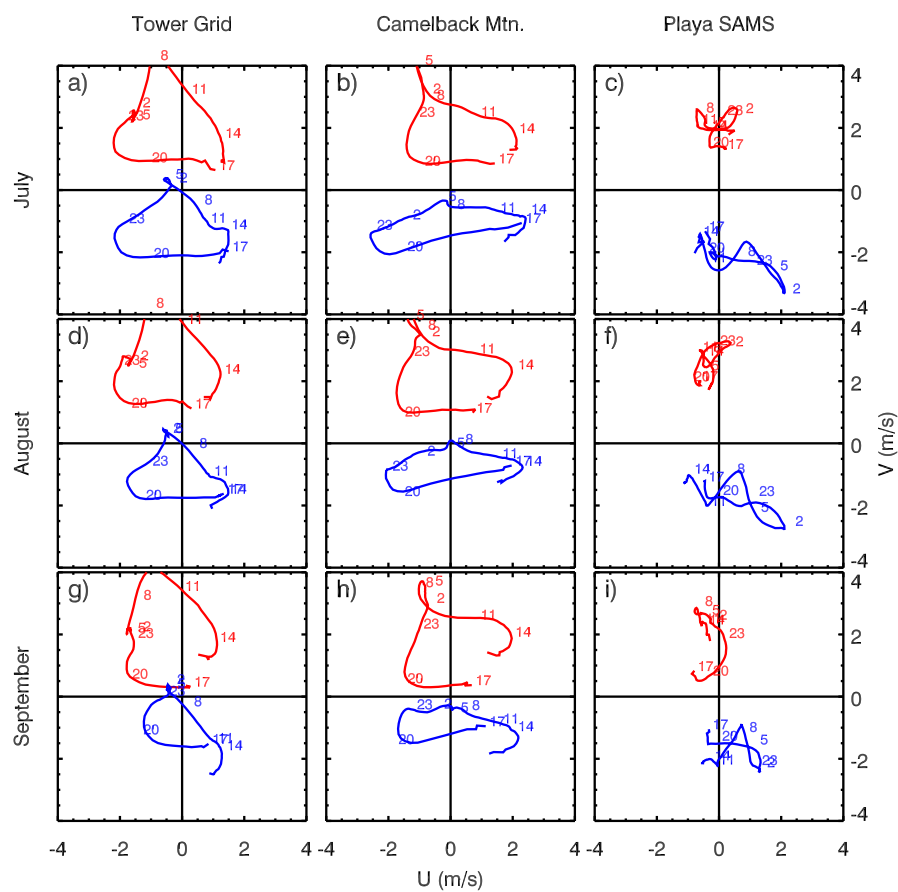Fig. B.2. Same as Figure B.1 except for April, May, and June.

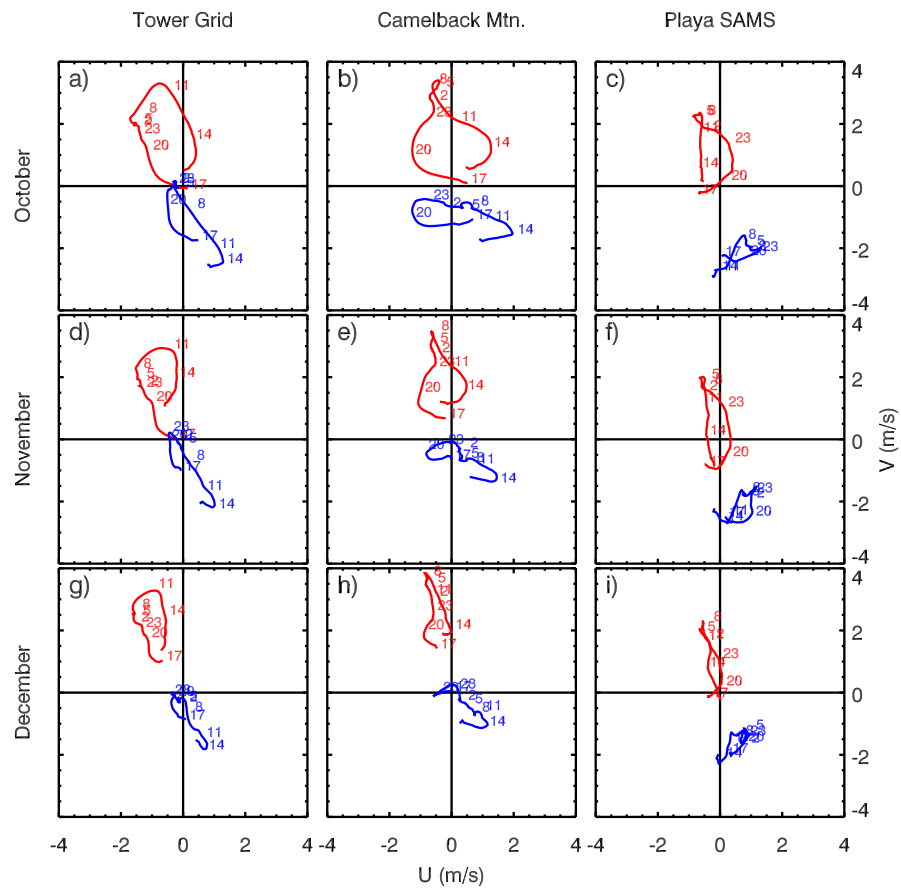Fig. B.3. Same as Figure B.1 except for July, August, and September.

Fig. B.4. Same as Figure B.1 except for October, November, and December.